The performance of the CMS muon detector in proton-proton collisions at $\sqrt{s}$ = 7 TeV at the LHC

The performance of the CMS muon detector in proton-proton collisions at $\sqrt{s} = 7$ TeV at the LHC

The CMS collaboration

E-mail: cms-publication-committee-chair@cern.ch

ABSTRACT: The performance of all subsystems of the CMS muon detector has been studied by using a sample of proton-proton collision data at $\sqrt{s} = 7$ TeV collected at the LHC in 2010 that corresponds to an integrated luminosity of approximately $40 \, \text{pb}^{-1}$. The measured distributions of the major operational parameters of the drift tube (DT), cathode strip chamber (CSC), and resistive plate chamber (RPC) systems met the design specifications. The spatial resolution per chamber was 80–120 μm in the DTs, 40–150 μm in the CSCs, and 0.8–1.2 cm in the RPCs. The time resolution achievable was 3 ns or better per chamber for all 3 systems. The efficiency for reconstructing hits and track segments originating from muons traversing the muon chambers was in the range 95–98%. The CSC and DT systems provided muon track segments for the CMS trigger with over 96% efficiency, and identified the correct triggering bunch crossing in over 99.5% of such events. The measured performance is well reproduced by Monte Carlo simulation of the muon system down to the level of individual channel response. The results confirm the high efficiency of the muon system, the robustness of the design against hardware failures, and its effectiveness in the discrimination of backgrounds.

2013 JINST 8 P11002

Contents

Table 1. Requirements for the CMS muon system as originally specified (adapted from ref. [3]). "BX identification" is explained in the text.

Muon trigger	BX identification	Trigger on single- and multi-muon events with well defined thresholds from a few to 100 GeV/c
Momentum resolution	Muon system	8–15% at 10 GeV/c, 20–40% at 1 TeV/c
	Tracker & muon system	1–1.5% at 10 GeV/c, 6–17% at 1 TeV/c Track matching between tracker and muon system at 1 TeV/c better than 1 mm in the bending plane, better than 10 mm in the non-bending plane
Charge misassignment		Less than 0.1% at muon p_T = 100 GeV/c

1 Introduction

Muon detection is a powerful tool for recognizing signatures of interesting physics processes over the high background rates at the Large Hadron Collider (LHC) [1]. The muon detector system in the Compact Muon Solenoid (CMS) experiment [2] has 3 primary functions: muon triggering, identification, and momentum measurement. Good muon momentum resolution is provided by the high spatial resolution of the detector and the high magnetic field of the superconducting solenoidal magnet and its flux-return yoke.

The CMS muon system (figures 1, 2, and 3) is designed to measure the momentum and charge of muons over a large kinematic range in LHC collisions. Table 1 lists selected design requirements as specified in the Muon Technical Design Report (TDR) [3] in 1997. These requirements were determined by assuming a 4-T magnetic field. Later it was decided to operate the magnet at 3.8 T, leading to a ≈5% degradation in the achievable momentum resolution.

The CMS detector uses 3 types of gas-ionization particle detectors for muon identification. To be compatible with the geometry of the central solenoidal magnet, it is natural to have a cylindrical barrel region and planar endcaps. Because of the large area to be covered the muon detectors must be relatively inexpensive, and because the CMS detector is inaccessible when the LHC is running, it is important that the muon system be robust. This technology also allows fast access to hit information from the entire muon detector for use in a hardware muon trigger that is relatively immune to the high particle densities originating from proton-proton collisions at the center of the detector.

Previous publications [4–14] have described the performance of the muon system during the long cosmic-ray-muon runs of 2008 and 2009. Here we describe the performance of the CMS muon detectors using a data sample accumulated at $\sqrt{s} = 7$ TeV during the 2010 LHC proton-proton physics run corresponding to an integrated luminosity of approximately 40 pb^{-1}. The same data have already been used to study the performance of CMS muon reconstruction [15], whereas the results presented in this paper focus on the performance at the individual detector level. Following a general description of the muon system and its operation, section 3 describes the calibration of the individual muon subsystems. This is followed by sections on CSC and DT local triggering, and the measurement of the position and time resolution of all of the muon subsystems. Local

reconstruction efficiency is discussed in section 7, and the radiation background and alignment issues are explained in sections 8 and 9, respectively. The important role of data quality monitoring (DQM) is considered in section 10. A summary of the failure rates of muon system electronic components is presented in appendix A. Finally, the offline simulation of the muon detector is described in appendix B.

2 Overview of the muon system

The basic detector process utilized in the CMS muon system is gas ionization. For all the different technologies — drift tubes, cathode strip proportional planes, and resistive plates — the basic physical modules are called "chambers". The chambers are independently-operating units, which are assembled into the overall muon detector system of CMS. The chambers form part of a spectrometer in which the analyzing magnet is the central solenoid together with the flux-return yoke of CMS. To match the cylindrical geometry of the solenoid, the barrel region is instrumented with drift tube chambers, and the 2 endcap regions with cathode strip chambers. Resistive plate chambers are interspersed in both the barrel and endcap regions. The muon chambers must detect the traversing track at several points along the track path to utilize the magnet to measure the deflection of muons as they pass through its field. In the barrel region, this requires chambers to be positioned at several different values of the radial distance R from the beam line, and in the endcap region at several different values of distance along the beam direction z. A "station" is an assembly of chambers around a fixed value of R (in the barrel) or z (in the endcap). There are 4 stations in the barrel and in each endcap (figure 1), labeled MB1–MB4 and ME1–ME4, respectively. Along z, the drift tubes and resistive plate chambers in the barrel are divided into 5 "wheels", with Wheel 0 centered at $z = 0$ and wheels W+1 and W+2 in the +z direction and W−1 and W−2 in the −z direction. Similarly in the R direction in the endcaps, there are "rings" of endcap resistive plate chambers and cathode strip chambers. The latter are labeled ME1/n–ME4/n, where integer n increases with the radial distance from the beam line.

2.1 Drift tube and cathode strip chamber subsystems

In the barrel region, the muon rate is low, the neutron background is relatively small (except in the outermost station MB4), and the magnetic field is mostly uniform with strength below 0.4 T in between the yoke segments (figure 4). Here, drift chambers with standard rectangular cells and sophisticated electrical field shaping are employed. The barrel drift tube (DT) chambers cover the pseudorapidity region $|\eta| < 1.2$, where $\eta = -\ln[\tan(\theta/2)]$ and θ is the polar angle with respect to the counterclockwise beam direction. They are divided into 12 ϕ-segments per wheel, where ϕ is the azimuthal angle, forming 4 stations at different radii interspersed between plates of the magnet flux-return yoke. Each station consists of 8 layers of tubes measuring the position in the bending plane and 4 layers in the longitudinal plane (except for MB4).

The basic element of the DT system is the drift cell (figure 5, right). The cell has a transverse size of $42 \times 13 \text{ mm}^2$ with a 50-μm-diameter gold-plated stainless-steel anode wire at the center. A high voltage of $+3600$ V is applied to the wire. The gas mixture (85%/15% of Ar/CO_2) provides good quenching properties and a saturated drift velocity of about 55 μm/ns. The maximum drift time is almost 400 ns. The cell design makes use of 4 electrodes (including 2 cathode strips) to
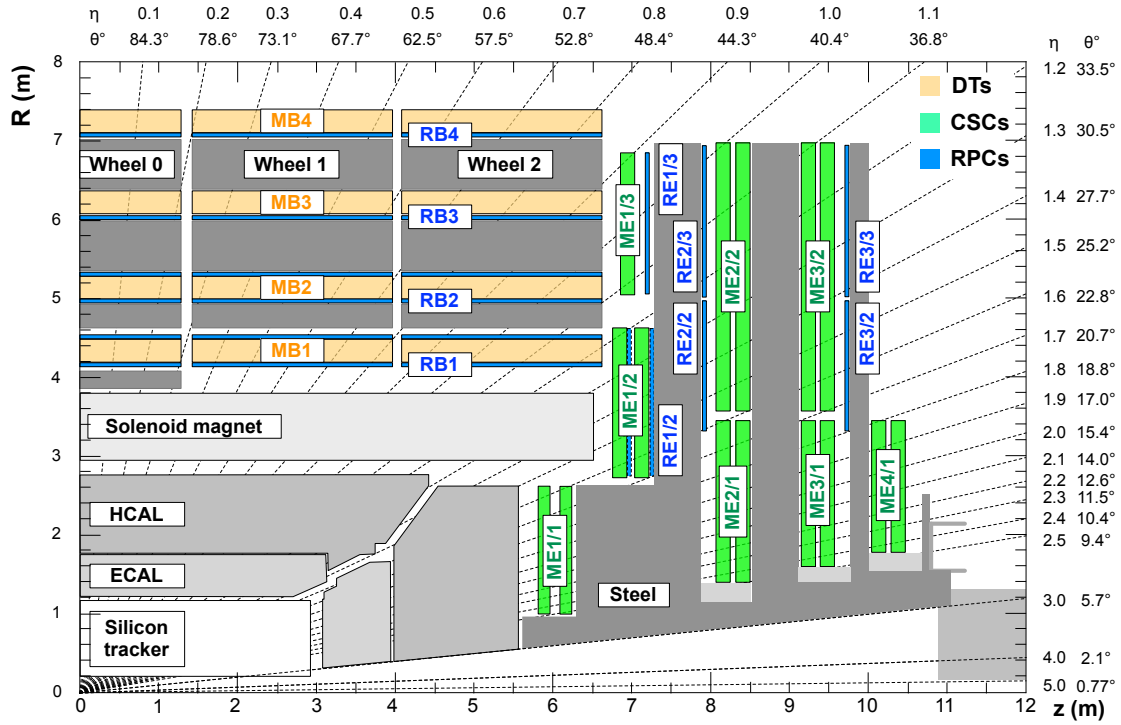
Figure 1. An *R–z* cross section of a quadrant of the CMS detector with the axis parallel to the beam (*z*) running horizontally and radius (*R*) increasing upward. The interaction point is at the lower left corner. Shown are the locations of the various muon stations and the steel disks (dark grey areas). The 4 drift tube (DT, in light orange) stations are labeled MB ("muon barrel") and the cathode strip chambers (CSC, in green) are labeled ME ("muon endcap"). Resistive plate chambers (RPC, in blue) are in both the barrel and the endcaps of CMS, where they are labeled RB and RE, respectively.

shape the effective drift field: 2 on the side walls of the tube, and 2 above and below the wires on the ground planes between the layers. They operate at −1200 and +1800 V, respectively. Four staggered layers of parallel cells form a superlayer (SL). A chamber consists of 2 SLs that measure the *r-φ* coordinates with wires parallel to the beam line, and an orthogonal SL that measures the *r-z* coordinate, except for MB4, which has only an *r-φ* SL (figure 5, left). Here *r* is the nominal distance from the beam collision point. The chambers are limited in size in the longitudinal dimension by the segmentation of the barrel yoke, and are about 2.5 m long. In the transverse dimension, their length varies with the station, ranging from 1.9 m for MB1 to 4.1 m for MB4.

In the endcap regions of CMS the muon rates and background levels are higher, and the magnetic field is strong and non-uniform (figure 4). Here, cathode strip chambers (CSC) are installed since they have fast response time (resulting from a short drift path), they can be finely segmented, and they can tolerate the non-uniformity of the magnetic field. The CSCs cover the |*η*| region from 0.9 to 2.4. Each endcap has 4 stations of chambers mounted on the faces of the endcap steel disks, perpendicular to the beam. A CSC consists of 6 layers, each of which measures the muon position in 2 coordinates. The cathode strips run radially outward and provide a precision measurement in the *r-φ* bending plane (figure 6, left). The wires, ganged into groups to reduce the number of readout channels, provide a coarse measurement in the radial direction.
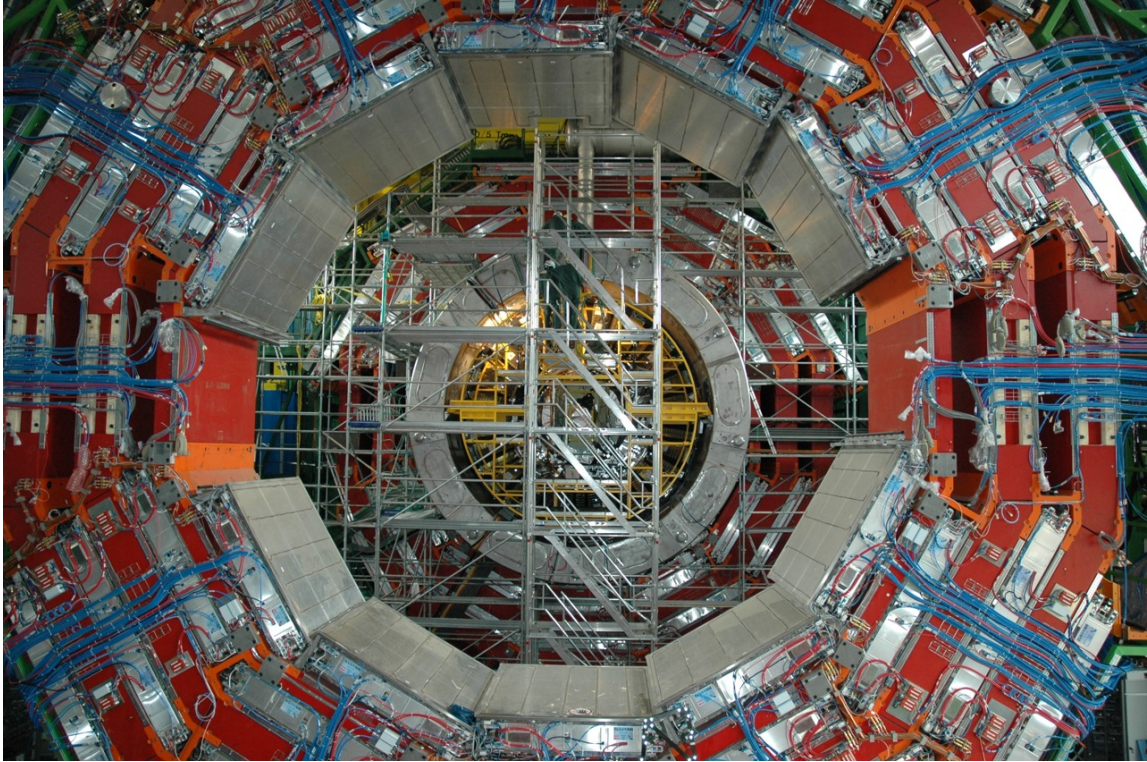
Figure 2. Photograph of a barrel wheel during the construction of CMS in June 2006. The 4 stations of DT chambers are separated by layers of the yoke steel (painted red). Several chambers had not yet been installed.

The CSCs operate as standard multi-wire proportional counters (MWPC), but with a cathode strip readout that precisely measures the azimuthal position at which a muon or other charged particle crosses the gas volume (figure 6, right) [16]. CSCs of various physical dimensions are used in the system, ranging in length from about 1.7 to 3.4 m in the radial dimension. In the inner rings of stations 2, 3, and 4, each CSC subtends a ϕ angle of about 20°; all other CSCs subtend an angle of about 10°. Each layer of a CSC contains 80 cathode strips, each of which subtends a constant ϕ angle between 2.2 and 4.7 mrad and projects to the beamline. The anode wires have a diameter of 50 µm and are spaced by 3.16 or 3.12 mm in all chambers except ME1/1 where they have 30 µm diameter and are 2.5 mm apart. They are ganged in groups of 5 to 16 wires, with widths from 16 to 51 mm, which limits the position resolution in the wire coordinate direction. All chambers use a gas mixture of 50% CO_2, 40% Ar, and 10% CF_4. The ME1/1 chambers are operated at an anode voltage of 2.9 kV and all others at 3.6 kV. Alternate layers of all CSCs except those in ME1/1 are shifted by half a strip width, and neighboring CSCs within all rings except ME1/3 overlap each other by 5 strip widths to avoid gaps between chambers.

The CSCs in the innermost ring of station 1, ME1/1, have a structure different from those of the other rings. The strip region of each ME1/1 chamber is divided into two at $|\eta| = 2.1$, so that each region can trigger and be read out independently of the other. Narrower strips than in the other chambers are used in both regions. The innermost region is labelled "ME1/1a" and the outer "ME1/1b". The 48 strips in each ME1/1a region of an ME1/1 chamber are ganged in groups
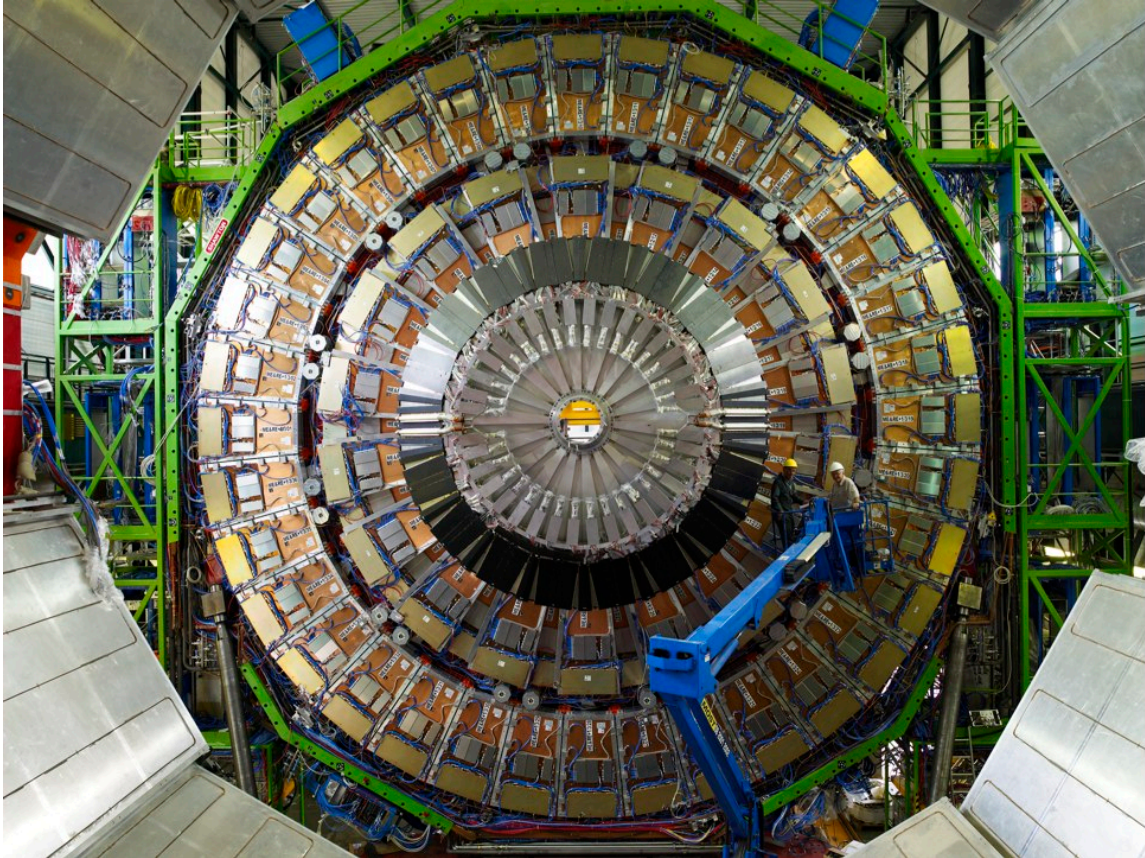
Figure 3. Photograph of the ME1 muon station of the "plus" ($z > 0$) endcap during the construction of CMS. Visible in concentric rings are the CSC types ME1/2 and ME1/3. The ME1/1 chambers are hidden behind the endcap calorimeters closest to the center. The endcap RPCs are in the layer behind the CSCs.

of 3, in steps of 16, to give 16 readout channels, to satisfy space and cost constraints for the on-chamber electronics. This ganging leads to ambiguities in reconstruction and triggering, and will be removed in a future upgrade of the detector.

The B field in the CSC chamber volumes does not exceed 0.5 T except in ME1. In ME1/1 the field is almost purely axial; in ME1/2 there is both an axial component of about 1 T decreasing to 0.5 T with increasing distance from the magnet axis and a radial component decreasing from about 1 T close to the magnet axis to zero far from it. In ME1/1 the anode wires are tilted by 29° to compensate for the Lorentz drift of electrons from the gas ionization process that otherwise causes a smearing of the induced charge distribution on the cathode strips and hence a deterioration in position resolution. In ME1/2 the radial component of the field induces a smearing equivalent to that from muons incident at non-zero ϕ, but there is no simple way to compensate for this in chamber construction. However, the degraded resolution is still within the specified requirements.

The DT and CSC muon detector elements together cover the full CMS pseudorapidity interval $|\eta| < 2.4$ with no acceptance gaps, ensuring good muon identification over a range corresponding to $10° < \theta < 170°$. Offline reconstruction efficiency for the muons is typically 96–99% except in the gaps between the 5 wheels of the yoke (at $|\eta| = 0.25$ and 0.8) and the transition region between
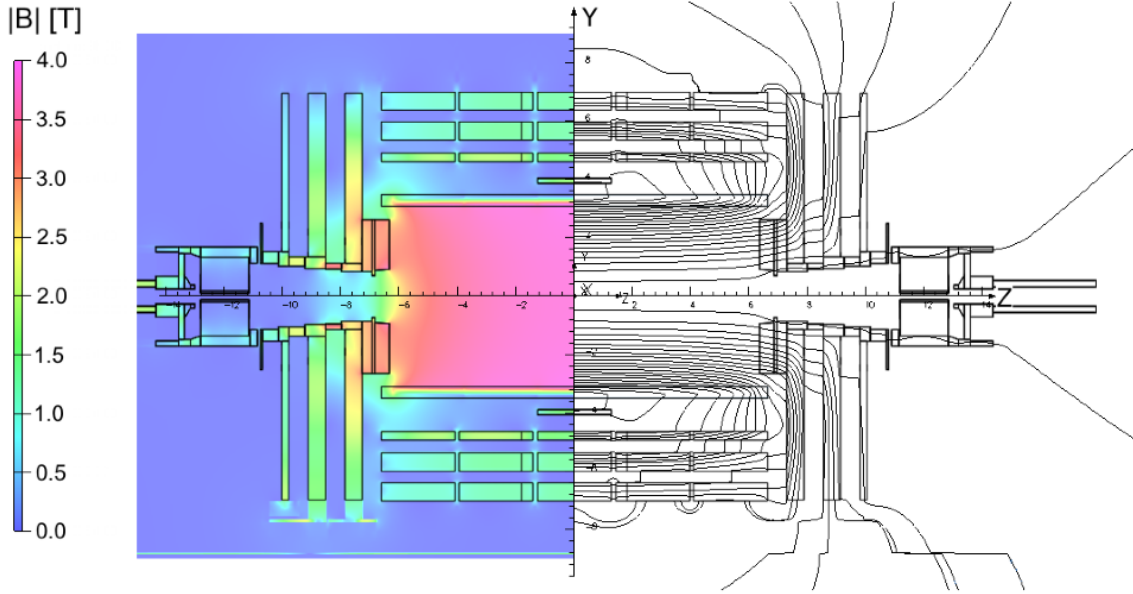
Figure 4. Map of the $|B|$ field (left) and field lines (right) predicted for a longitudinal section of the CMS detector by a magnetic field model at a central magnetic flux density of 3.8 T. Each field line represents a magnetic flux increment of 6 Wb.
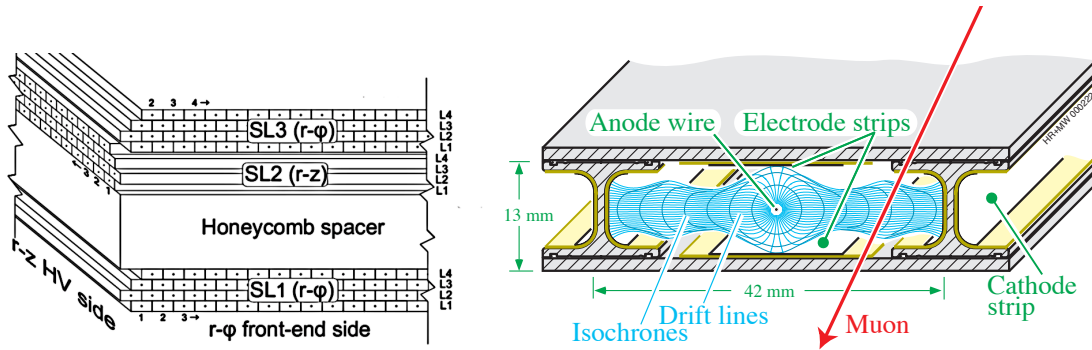
Figure 5. Left: schematic view of a DT chamber. Right: section of a drift tube cell showing the drift lines and isochrones.

the barrel outer wheels and the endcap disks [15]. The amount of absorbing material before the first muon station reduces the contribution of punch-through particles to about 5% of all muons reaching the first station and to about 0.2% of all muons reaching further muon stations. Crucial properties of the DT and CSC systems are that they can each identify the collision bunch crossing that generated the muon and trigger on the p_{T} of muons with good efficiency, and that they have the ability to reject background by means of timing discrimination.

The LHC is a bunched machine, in which the accelerated protons are distributed in bunches separated by one (or more) time steps of 25 ns. This is therefore also the minimum separation between bunch crossings, in which proton-proton collisions occur. Thus, a convenient time quantity for both the accelerator and the detectors is the bunch crossing (BX) "unit" of 25 ns, and, because the fundamental readout frequency is 40 MHz, clock times are often quoted in BX units. The
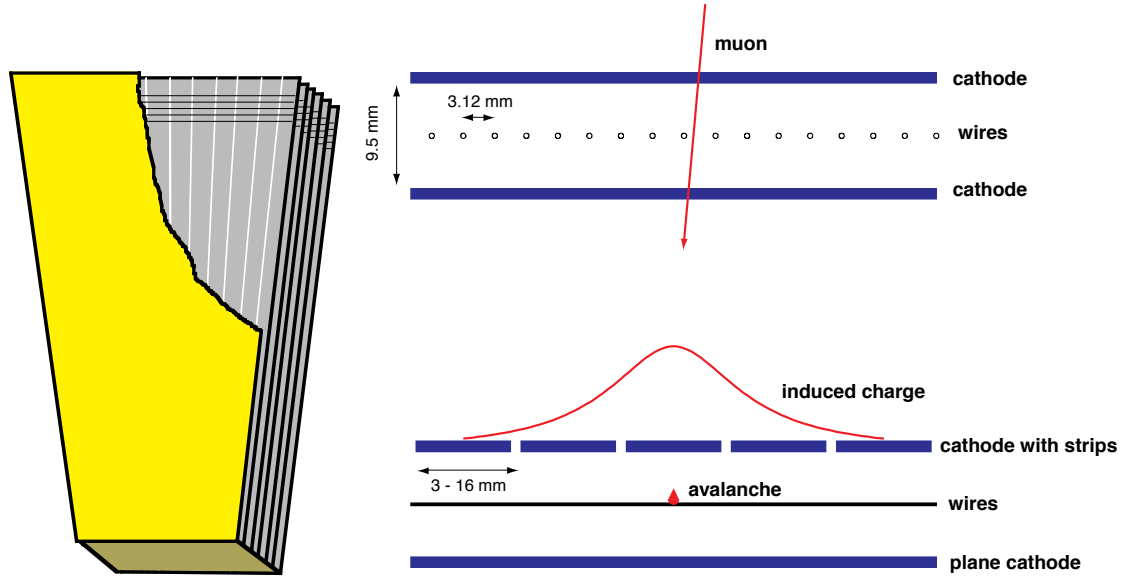
Figure 6. Left: cut-away diagram of a CSC showing the 6 layers and the orientations of the wires and strips (not all shown). Right: cross-sectional views of the gas gap in a CSC showing the anode wires and cathode planes, and a schematic illustration of the gas ionization avalanche and induced charge distribution on the cathode strips.

ability of the muon chambers to provide a fast, well-defined signal is crucial for triggering on muon tracks. To ensure unambiguous identification (ID) of the correct bunch crossing and the time coincidence of track segments among the many muon stations, the local signals must have a time dispersion of a few nanoseconds, much less than the minimum 25 ns separation of bunch crossings. A design in which intrinsically slow tracking chambers nevertheless provide good timing and spatial performance at the trigger level is an important feature of the CMS muon system.

2.2 Resistive plate chamber system

In addition to these tracking detectors, the CMS muon system includes a complementary, dedicated triggering detector system with excellent time resolution to reinforce the measurement of the correct beam crossing time at the highest LHC luminosities. The resistive plate chambers (RPC) are located in both the barrel and endcap regions, and they can provide a fast, independent trigger with a lower p_T threshold over a large portion of the pseudorapidity range ($|\eta| < 1.6$). The RPCs are double-gap chambers, operated in avalanche mode to ensure reliable operation at high rates.

Figure 7 shows the layout of a double-gap RPC. Each gap consists of two 2-mm-thick resistive Bakelite plates separated by a 2-mm-thick gas gap. The outer surface of the bakelite plates is coated with a thin conductive graphite layer, and a voltage of about 9.6 kV is applied. The RPCs are operated with a 3-component, non-flammable gas mixture that consists of 95.2% Freon ($C_2H_2F_4$, known as R134a), 4.5% isobutane (i-C_4H_{10}), and 0.3% sulphur hexafluoride (SF_6). After mixing, water vapor is added to obtain a mixture with a relative humidity of 40%–50%. Readout strips are aligned in η in between the 2 gas gaps. A charged particle crossing an RPC will ionize the gas in both gas volumes and the avalanches generated by the high electric field will induce an image
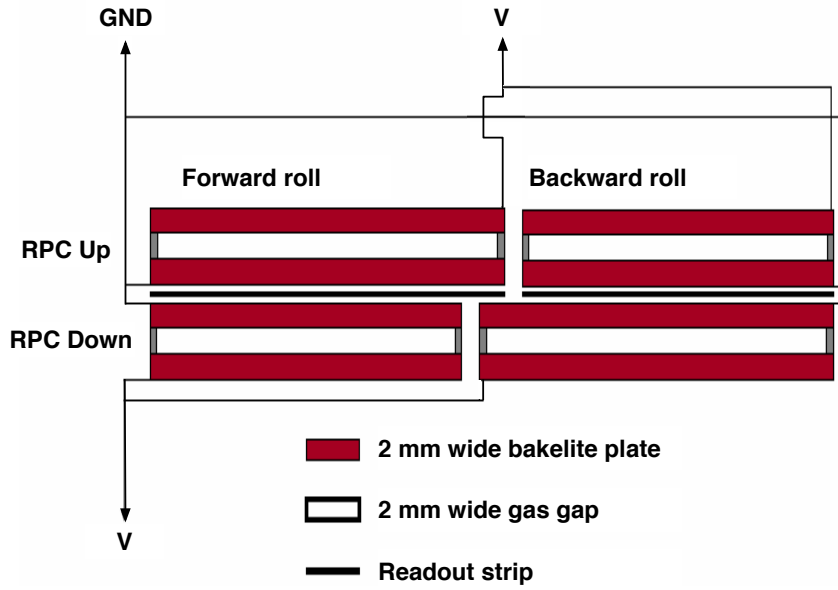
Figure 7. Schematic view of a generic barrel RPC with 2 "roll" partitions.

charge, which is sampled by the readout strips. This signal is discriminated and shaped by the front-end electronics.

The RPCs are arranged in stations following a sequence similar to the DTs and CSCs. In the RPC barrel (RB) there are 4 stations, namely RB1, RB2, RB3, and RB4, while in the RPC endcap (RE) the 3 stations are RE1, RE2, and RE3. The innermost barrel stations RB1 and RB2 are instrumented with 2 layers of RPCs facing the innermost (RB1in and RB2in) and outermost (RB1out and RB2out) sides of the DT chambers. Every chamber is then divided from the readout point of view into 2 or 3 η partitions called "rolls" (figure 7). In the endcaps, each station is divided into 3 rings (identified as rings 1, 2, and 3) at increasing radial distance from the beam line. Ring 1 was not instrumented in 2010; the RPC system therefore covered only the region up to $|\eta| = 1.6$. Each endcap ring is composed of 36 chambers covering the full azimuthal range. From the readout point of view, each endcap chamber is divided into 3 η partitions (rolls) identified by the letters A, B, and C. Thus the endcap RPCs are identified in the following way: REn/r/x where n is the station ($\pm 1, \pm 2, \pm 3$), r is the ring (2 or 3), and x is the roll (A, B, or C).

2.3 Muon triggering, tracking, and reconstruction

The triggering scheme of the CMS muon system relies on 2 independent and complementary triggering technologies: one based on the precise tracking detectors in the barrel and endcaps, and the other based on the RPCs. The tracking detectors provide excellent position and time resolution, while the RPC system provides excellent timing with somewhat poorer spatial resolution.

For values of p_T up to $200\,\mathrm{GeV}/c$, the momentum resolution is dominated by the large multiple scattering in the steel, combined in the endcaps with the effect of the complicated magnetic field that is associated with the bending of the field lines returning through the barrel yoke. The detectors

designed to meet the required measurement specifications and to operate in this environment are robust, multilayered chambers from which the fine spatial resolution required for good momentum resolution at high muon momenta can be obtained with a modest resolution per layer.

The large number of layers in each tracking chamber is exploited by a trigger hardware processor that constructs track segments within the chambers with a precision sufficient to set sharp transverse momentum (p_T) thresholds up to 100 GeV/c for a level-1 (L1) trigger, and to identify the parent bunch crossing with very good time resolution. This component of the L1 trigger is called the "local" trigger since it operates purely with information local to a chamber. The local trigger information is combined to form a "regional" trigger, one for each of the muon subsystems. These regional triggers are finally combined to form the "global" muon trigger that serves as one of the primary L1 triggers for CMS. A suitably steep transverse momentum threshold is obtained because the local spatial resolution of the segments is on the order of a couple of millimeters. This resolution is necessary to guarantee a high trigger efficiency and defines a lower limit on the accuracy that must be reached by the alignment of the CSC and DT chamber positions.

The geometry of CMS strongly influences the performance of the muon system. The change in the direction of the magnetic field in the return yoke causes the curvature of the muon trajectory to reverse. Therefore, the first muon detector stations (ME1, MB1) in both the barrel and endcap regions are critical, since they provide the largest sagitta and, hence, the most important contribution to the measurement of the momentum of high momenta (more than a few hundred GeV/c) muons, for which multiple scattering effects become less significant.

Reconstruction proceeds by first identifying hits in the detection layers of a muon chamber due to the passage of a muon (or other charged particle), and in the DT and CSC systems by then building straight-line track segments from these hits. This is referred to as "local" reconstruction. The reconstruction of muon tracks from these hits and segments is called "global" reconstruction. Muon tracks can be reconstructed by using hits in the muon detectors alone; the resulting muon candidates are called "standalone muons". Alternatively, the reconstruction can combine hits in the muon detectors with those in the central tracker; the resulting candidates are called "global muons". The muon system can also be used simply to tag tracks extrapolated from the central tracker; such tracks are called "tracker muons". For muons with momenta below $\approx$300 GeV/c, tracker muons have better resolution than global muons. As the p_T value increases, the additional hits in the muon system gradually improve the overall resolution. Global muons exploit the full bending of the CMS solenoid and return yoke to achieve the ultimate performance in the TeV/c region.

Table 2 lists the functions and parameters of the muon systems as installed in CMS during the 2010 running period. The design specifications for spatial and time resolution are also listed [3]. One of the goals of the present publication is to compare the requirements as outlined in the Muon TDR with the performance achieved in 2010.

3   Calibration

This section describes the procedures used in the extraction of calibration parameters that affect the performance of the CMS muon system, such as the drift velocity for the DTs and the electronic channel gains for the CSCs.

Table 2. Properties and parameters of the muon systems during the 2010 data-taking period. The design values of the position and time resolutions are from the CMS Muon TDR (1997) (ref. [3]). As discussed in later sections, in general, these specifications were met and in some cases exceeded.

Muon subsystem	Drift Tubes (DT)	Cathode Strip Chambers (CSC)	Resistive Plate Chambers (RPC)
Function	Tracking, p_T trigger, BX ID	Tracking, p_T trigger, BX ID	p_T trigger, BX ID
$|\eta|$ range	0.0–1.2	0.9–2.4	0.0–1.6
No. of stations	4	4 (no ME4/2 ring)	Barrel 4; Endcap 3
No. of layers	r-ϕ: 8, z: 4	6	2 in RB1 and RB2; 1 elsewhere
No. of chambers	250	468	Barrel 480; Endcap 432
No. of channels	172 000	Strips 220 000; Wire groups 183 000	Barrel 68 000; Endcap 41 000
Design position resolution (σ) for perpendicular tracks	per wire 250 μm; r-ϕ (6/8 pts) 100 μm; z (3/4 pts) 150 μm	per chamber r-ϕ (6 pts) ME1/1, ME1/2 75 μm other CSCs 150 μm; r (6 pts) 1.9–6.0 mm	Strip size (on the order of a centimeter)
Design time resolution	5 ns	6 ns	3 ns

Calibration constants and monitoring parameters are stored as *conditions data*. They are produced both online, directly from the front-end electronics, and by dedicated calibration algorithms run offline. The CMS conditions database [7] uses 3 databases (DB) for storing non-event data: the online master database system (OMDS) is in the online network at the detector site and stores the data needed for the configuration and appropriate detector settings together with the conditions data produced directly from the front-end electronics; the offline reconstruction condition DB online subset (ORCON), also located at the detector site, stores all conditions data that are needed for the high-level trigger (HLT) as well as for detector performance studies; and the offline reconstruction condition DB offline subset (ORCOFF), located at the CERN computing center (tier 0), contains a copy of the information in ORCON. It is the database used for all offline processing and physics analyses.

To provide a rapid response to changing detector operating conditions, special offline calibration workflows use dedicated calibration data streams, distinct from the main collisions data output stream, as input to the offline calibration procedures. These can then provide updated calibration information rapidly enough to be used in the full offline reconstruction of the collision data [7]. They are available with very low latency and are analyzed at the CERN analysis facility for a prompt determination of new constants.

The specific calibration procedures for the DTs and CSCs are described in the next sections, followed by a brief description of the procedure followed for setting the operating voltages and electronics thresholds of the RPCs.

3.1 DT system calibration

Charged particles crossing a drift cell in the DTs ionize the gas within the cell. The drift time of the ionization electrons is obtained by using a high-performance time-to-digital converter (TDC) [17], after subtraction of a time pedestal. The time pedestal contains contributions from the latency of the trigger and from the propagation time of the signal within the detector and the data acquisition chain. The hit position, i.e., the distance of the muon track with respect to the anode wire, is reconstructed as

$$x_{hit} = t_{drift} \cdot v_{drift} \equiv \left(t_{TDC} - t_{ped} \right) \cdot v_{drift}, \tag{3.1}$$

where t_{TDC} is the measured time, t_{ped} the time pedestal, and v_{drift} the effective drift velocity, which is assumed to be approximately constant in the cell volume.

The operating conditions of the chambers are monitored continuously [3]. The high voltage supplies have a built-in monitor for each channel. The temperature of the gas, nominally at room temperature, is measured on each preamplifier board inside the chamber. The gas pressure is regulated and measured at the gas distribution rack on each wheel, and is monitored by 4 additional sensors, 2 at the inlets and 2 at the outlets of each chamber. The flow from a single gas distribution rack, shared by 50 chambers, is monitored at the inlet and outlet lines of each individual chamber. Any leakage in the gas line can be detected via the flow and pressure measurements.

Small gas chambers called drift velocity chambers [18, 19] are located in the gas room adjacent to the CMS cavern, outside the magnetic field, and accessible during LHC operation. They are used to measure the drift velocity in a gas volume with a very homogeneous electric field. A drift velocity chamber can selectively measure the gas distributed to, and returned from, each DT chamber in a wheel, thus providing rapid feedback on any changes due to the gas mixture or contamination of the gas.

3.1.1 Time pedestal offline calibration

The drift time t_{drift} is obtained from the TDC measurement after the subtraction of a time pedestal. In an ideal cell, the time distribution from the TDC, t_{TDC}, would have a box shape starting at close to 0 ns for muon tracks passing near the anode and extending up to 380 ns for those passing close to the cathode. In practice, different time delays related to the trigger latency and the length of the cables to the readout electronics contribute to the time measured by the TDC as follows:

$$t_{TDC} = t_{drift} + t_0^{wire} + \underbrace{t_{L1} + t_{TOF} + t_{prop}}_{t_{trig}}, \tag{3.2}$$

where the different contributions to the time pedestal are classified as

- t_0^{wire}, the channel-by-channel signal propagation time to the readout electronics, relative to the average value in a chamber; it is used to equalize the response of all channels within a chamber, and hence controls inter-channel synchronization;

- t_{L1}, the latency of the L1 trigger;

- t_{TOF}, the time-of-flight (TOF) of the muon produced in a collision event, from the interaction point to the cell;

- t_{prop}, the propagation time of the signal along the anode wire.

The inter-channel synchronization t_0^{wire} is determined by test pulse calibration runs. It is a fixed offset, since it depends only on the cable or fiber lengths. A test pulse is simultaneously injected in 4 channels of a front-end board, each from a different layer in an SL, simulating a muon crossing the detector. The same test pulse signal is also distributed to other 4-channel groups, 16 channels apart, such that the entire DT system is scanned in 16 cycles.

The remaining contribution to the time pedestal is extracted from the data for each SL. It is computed as the turn-on point of the TDC time distribution [4, 20], after correction for the inter-channel synchronization. Channels identified as noisy are not considered. This contribution is called t_{trig}, since it is dominated by the L1 trigger latency and includes the contributions from the average time-of-flight, roughly corresponding to the time taken by muons to reach the center of the SL, as well as the average signal propagation time along the anode wire, taken from the center of the wire to the front-end board.

The correction for the propagation time along the wire and the muon time-of-flight to the cell is performed at the reconstruction level, after the 3D position of the track segment is determined [21]. The segment is built in a multi-step procedure, as described in more detail in section 7. First, the reconstruction is performed in the r-ϕ and r-z projections independently. Once the 2 projections are paired, the segment position inside the chamber can be estimated and the drift time is further corrected for the propagation time along the anode wire and for the time-of-flight from the center of the SL. The 3D segment is then updated.

To define the turn-on point of the TDC time distributions more precisely, a correction to the t_{trig} pedestal is calculated by using the hit position residuals. The residuals are computed as the distance between the hit position and the intersection of the 3D segment with the layer plane, reconstructed as described above. The offset in the mean of the residual distribution for each SL (divided by the drift velocity) is used as an estimate of the correction that is added to the time pedestal (subtracted from the drift time reconstruction). This procedure is repeated iteratively. The t_{trig} values derived from a representative subset of the 2010 collision data are shown in figure 8 (top) for the first r-ϕ superlayer (SL1) in each chamber of the DT system. Similar values are obtained for all SLs.

3.1.2 Drift velocity calibration

The drift velocity depends on the gas mixture, purity, and the electrostatic configuration of the cell. The effective drift velocity, used in the hit reconstruction (see eq. (3.1)), is further affected by the presence of the residual magnetic field and the track incidence angle [4, 20]. The drift velocity is computed as an average for each SL in the system.

Two methods have been used to determine the drift velocity: the first is based on the "mean-time" technique, and the second is based on the local muon reconstruction in which a track is fitted to measurements from one chamber at a time.

The mean-time method [20] exploits the staggering of the chamber layers (see also section 4.1.2). Because of the staggering, ionization electrons drift in opposite directions in even and odd layers. Therefore the maximum drift time t_{max} in a semi-cell can be calculated from the drift times of hits from the track crossing nearby cells in consecutive layers, by using relations derived from detailed Garfield simulation of an individual drift cell [22]. In general, these relations depend on the track inclination and on the pattern of cells crossed by the track. The appropriate mean-time relation is chosen for each track by using the 3D position and direction of the track segment in
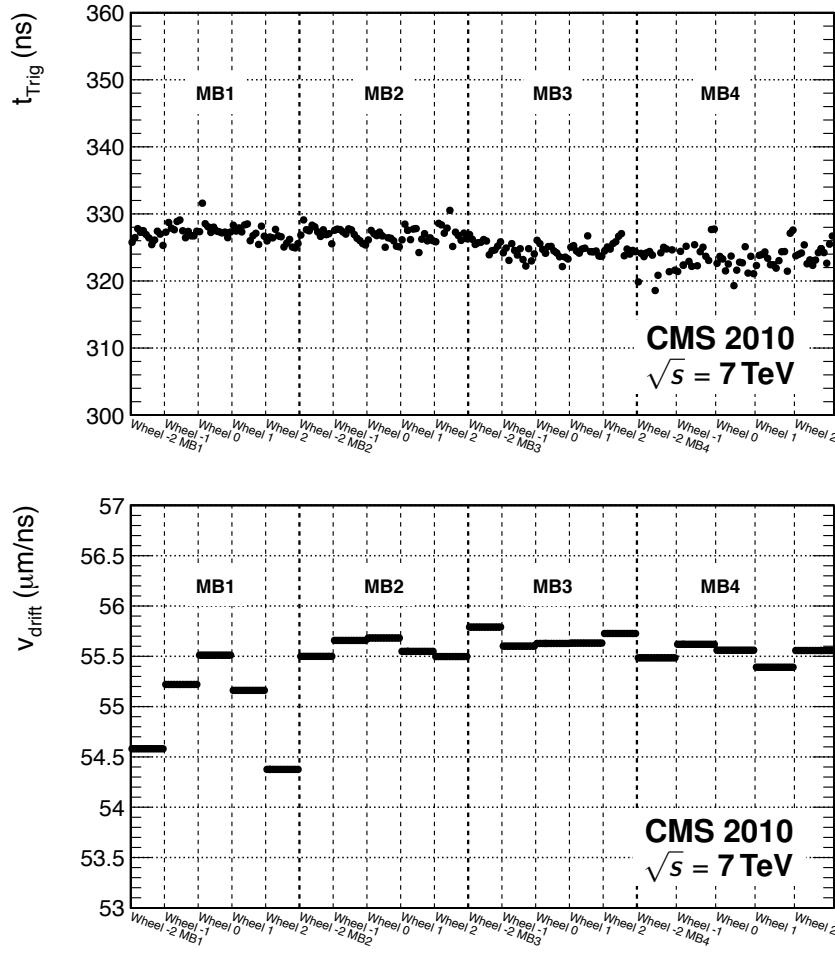
Figure 8. Top: time pedestals t_{trig} computed for all chambers in the DT system. Only values corresponding to the first r-ϕ superlayer (SL1) in each chamber are shown. Bottom: drift velocities of all the chambers in the DT system. Chambers belonging to the same wheel were merged by station in the computation of the drift velocity.

the SL. A linear approximation is used to determine the drift velocity, $v_{\text{drift}}^{\text{eff}} = L_{\text{semi-cell}}/< t_{\text{max}} >$, where $L_{\text{semi-cell}} = 20.3$ mm is approximately half the width of a drift cell.

The drift velocity obtained from the mean-time method depends directly on the measured drift time and hence on the time pedestal. Conversely, the time pedestal (see section 3.1.1), corrected by using the mean of the distributions of the hit residuals, is itself dependent on the drift velocity value used in the hit position computation (eq. (3.1)). The 2 parameters cannot be fully disentangled.

An alternative method for computing the drift velocity relies on the full reconstruction of the trajectory within the muon system [4]. A track is reconstructed by assuming the nominal drift velocity v_{drift} and, in a second step, is refitted with the drift velocity and the time of passage of the muon through the chamber as free parameters. The method is applied to the r-ϕ view of the track segment in a chamber, where up to 8 hits can be assigned to the track. This method cannot, however, be applied to the r-z SLs where only 4 points are available because an insufficient number of degrees

of freedom is available in the fit to disentangle the drift velocity and synchronization contributions. Figure 8 (bottom) shows the drift velocity values obtained for each chamber in the DT system (corresponding to r-ϕ SLs) from a subset of the 2010 collision data. Since the drift velocity is not expected to vary substantially among different sectors, the distributions corresponding to all chambers in each wheel were merged by station, thus yielding a constant value for each wheel within a station. A notable reduction ($\approx$2%) in the value of the drift velocity is observed in the innermost chambers of the outer wheels because of the Lorentz angle induced by the stronger magnetic field.

3.2 CSC system calibration

A set of calibrations and related tests of the CSCs and the front-end electronics is performed periodically. The tests are intended both to monitor the stability of the system and to determine parameters required for configuration of the electronics modules. Counting rates, chamber noise levels, and channel connectivity are monitored. The configuration constants include anode front-end board (AFEB) discriminator thresholds and delays, cathode front-end board (CFEB) trigger primitive thresholds, and numerous timing constants required for the peripheral crate electronics. These values are then uploaded to the electronics modules. Calibration of electronics channels is required to normalize the measured signals for use in reconstruction offline and in the HLT. The calibration constants, required for optimal hit reconstruction and for simulation of the CSC detectors, specify strip-to-strip crosstalk, strip channel noise, strip pedestals, and strip channel electronic gains.

3.2.1 CSC CFEB operation

The cathode strips are connected to 16-channel amplifier-shaper ASIC (application-specific integrated circuit) chips. The outputs from these ASIC chip channels are sampled every 50 ns. The sampled voltage levels are stored in switched capacitor array (SCA) [23] ASICs during the Level-1 trigger latency of 120 BXs. There are 96 channels per CFEB distributed across six 16-channel SCAs, with each channel containing 96 capacitors (equivalent to 192 BXs). These samples are digitized and read out when a local charged track (LCT) trigger associated with the CFEB is correlated in time with a L1 trigger accept (L1A) signal. (The L1 trigger is discussed in section 4.)

3.2.2 CSC CFEB calibration

For calibration purposes, L1As are generated by the local trigger control and are received synchronously by the CSC electronics. Two internal capacitors are incorporated on the amplifier-shaper ASIC chip for each cathode amplifier channel, and one precision external capacitor is mounted on the CFEB board to service each amplifier-shaper. Each capacitor can be used to generate a test pulse. These pulses are activated in parallel so that pulses for calibration runs can be completed during beam injection. For more details, see ref. [24].

The linearity, offset, and saturation of the amplifier are determined by incrementally varying the test pulse amplitude applied to every channel and measuring the output. This also yields the electronic gain for each strip channel. The raw pulse height measurements from each strip channel are normalized by these gains before use in the reconstruction of muon hit positions.

To determine crosstalk between neighboring strips, a fixed-sized pulse of very short duration (an approximate delta-function pulse) is injected into each amplifier channel. The output on neighboring channels is then measured. To obtain the crosstalk fraction (the ratio of the charge induced on a neighboring strip to the charge deposited on a strip) appropriate for an operating CSC, these amplifier responses to a delta-function charge deposition must be convoluted with the expected ion drift time distribution and the arrival time distribution of electrons (approximately uniform in time). Then, for a given time bin, the ratio of one side pulse to the central pulse plus both side pulses yields the crosstalk fraction. This is found to be linear in time for an interval of about 160 ns around the peak time of the central charge distribution. This linearity is confirmed by test beam measurements. The typical magnitude of the crosstalk fractions ranges from about 5% to 10%. Thus the crosstalk fractions for a given strip are determined by 4 crosstalk constants associated with a strip: a slope and intercept to describe the straight line representing the crosstalk coupling to each of its 2 neighbors, as a function of the SCA time bin. This information is stored as a 3×3 matrix for each strip and SCA time bin, with elements that relate the measured charge on the strip and its 2 neighbors to the input charge on the strip. These matrices are used directly to model crosstalk in simulation, and the inverse matrices can be used to unfold crosstalk from the real data. This is performed even though the reconstructed position of a muon is largely insensitive to crosstalk because the reconstruction algorithm is robust against symmetric channel-to-channel coupling.

To determine the pedestals on each chamber strip, the amplifier output is sampled continuously at 20 MHz with no input signal. Then the charge measured in each SCA time bin is taken as the pedestal. The pedestal noise (pedestal RMS) is correlated between the SCA time bins. Therefore, for each strip, a symmetric "noise matrix" is defined to describe the covariance between the pedestals in each time bin, with elements $C_{ij} = \langle Q_i \cdot Q_j \rangle - \langle Q_i \rangle \langle Q_j \rangle$, where Q_i is the charge in the time bin i, and the averages are over a large number of calibration events. This matrix is used to introduce appropriate pedestal correlations in the simulation. These "static" pedestals are not used in the reconstruction. Instead, the reconstruction uses a "dynamic" pedestal, which is based on the average of the first 2 SCA time bins before the peak of the signal arrives. This compensates for any baseline shift arising from high-rate operation. The static pedestals, however, are used in simulation to provide an appropriate baseline to the simulated signals.

Figure 9 displays the relative differences for gains and pedestals strip-by-strip between constants calculated before and after the $\sqrt{s} = 7$ TeV operation in 2010. There are about 220 000 strip channels, and the correlation between values associated with the same front-end boards is visible. Gross changes occurred when electronic boards were replaced during the year.

3.3 Validation and monitoring of calibration constants

A detailed validation is performed to assess the quality and monitor the stability of the calibration constants. For each new calibration set, a comparison to previous constants is carried out and the impact on the reconstruction performance is analyzed. The CMS data quality monitoring (DQM; see section 10) framework [25] is used throughout the validation procedure.

The local hit reconstruction in the DT system is directly dependent on variations in the time pedestal, as well as the drift velocity calibration. Small changes in the system are accounted for with new calibration constants, thus optimizing the chamber performance. The calibration procedures discussed in section 3.1.1 guarantee that the hit position residuals are well centered around 0.
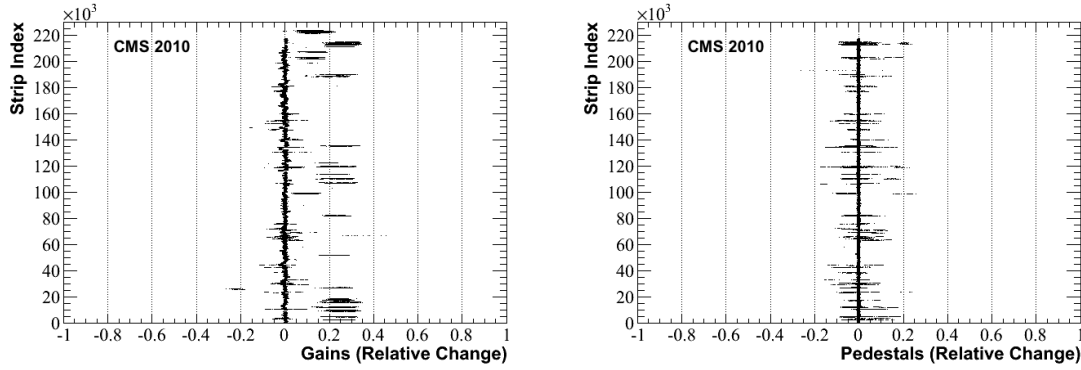
Figure 9. The change in CSC calibration constants calculated from calibration runs taken before and after CMS 2010 $\sqrt{s} = 7\,\mathrm{TeV}$ operation. Left: relative difference in gains. Right: relative difference in pedestals. The vertical axis "strip index" just indexes each strip in the system counting from 1.

The measured resolutions (figure 16) are within $300\,\mu\mathrm{m}$ for r-ϕ SLs and are slightly worse for the outermost station (MB4) because there is no theta information. They are larger for r-z SLs, when moving towards the external wheels (see section 5).

The impact of the calibration on the local muon reconstruction is studied by analyzing the hit position residuals. Resolution measurements are discussed in detail in section 5. The effect of changing calibration constants calculated before and after extended run periods on the hit position distributions in each CSC station has been shown to be very small. Testing and validation of new constants are performed regularly and possible changes due to the effect of calibration are closely monitored.

3.4 Setting RPC system operating voltages and thresholds

Once the gas composition is fixed, the main calibration parameters for the RPCs are the time synchronization (see section 4.1.4), the operating high-voltage points, and the electronics thresholds. The optimal operating voltages have been determined by means of dedicated runs only in 2011, while work on the electronics thresholds continued. During 2010, just 2 different values were chosen: 9550 and 9350 V for the endcap and barrel chambers, respectively. These values were derived from measurements made during the construction and commissioning phases, which were averaged over the 2 sets of chambers and extrapolated to the different conditions typical of CMS at the LHC (including the rate, which could not be accounted for previously).

4 Level-1 trigger

The purpose of the trigger system is to identify interesting event candidates fulfilling a predefined set of criteria, and to identify the appropriate originating bunch crossing for each candidate. Because at the LHC many interesting physics events contain muons, the muon detectors are an important component of the CMS L1 trigger system.

The CSC and DT systems provide candidate muon track segments through dedicated "local trigger" hardware. In the barrel, this task is performed by the DT local trigger (DTLT), and in

the endcaps by the CSC local trigger (CSCLT). The RPC trigger does not use local trigger hardware: muon candidates are directly constructed from the spatial and temporal coincidence of hits in multiple RPCs. The DT and CSC local trigger segments from each muon station are collected by trigger track finder (TF) hardware, which combine them to form a muon track and assign a transverse momentum value. At least 2 segments in 2 different stations are needed by the TFs to construct a muon candidate.

The DTLT system is described in detail in refs. [6, 26–28]. Only the main functions and characteristics are summarized here. The trigger segments are found separately in the transverse plane *x*-*y* (called the ϕ view) and in the plane that contains the *z* direction (called the θ view). The maximum drift time in the DT system is almost 400 ns, which is much longer than the minimum interval of 25 ns that separates 2 consecutive colliding bunches, but the DTLT system can associate each trigger segment with the bunch crossing in which the muon candidate was produced. For each BX the system provides up to 2 trigger segments per chamber in the ϕ view and 1 in the θ view. In the ϕ view, each trigger segment is associated with

- the BX at which the corresponding muon candidate was produced;

- the position and direction of the trigger segment;

- a quality word describing how many aligned DT hits were found;

- a bit that flags the segment for that BX as the best or second-best candidate, according to their assigned quality.

A set of these quantities is called a "DT trigger primitive".

Trigger primitives are provided separately for each station. During the 2010 data taking, the DTLT electronics was configured in the following way. A trigger segment was accepted if the minimum number of aligned hits in a trigger segment was 4 if the segment contained hits only from a single SL, or at least 3 in each SL if hits from both ϕ SLs were used. A DT muon trigger candidate was then identified by the DT track finder (DTTF) if an acceptable spatial and angular matching was found between at least 2 trigger primitives in 2 different stations [26].

A single muon is expected to produce one and only one DTLT segment in each station crossed by the particle. Additional spurious trigger candidates ("ghosts") can occasionally be produced. These can arise from the presence of additional displaced hits around the true muon track, or because adjacent electronics modules that reconstruct the trigger segments share a group of DT cells, thus leading to identical trigger candidates. A dedicated ghost-suppression algorithm is used by the DTLT electronics to discard such duplicate candidates (see section 4.3).

To measure the DTLT performance during the 2010 LHC run, approximately 10^6 events from 2 data samples containing reconstructed muons were studied: a minimum bias sample and a sample of W/Z events decaying to muons. Muon candidates in minimum bias events are characterized by low transverse momenta, $p_T > 3$ GeV/*c*, whereas W/Z decays produce muon tracks with $p_T > 20$ GeV/*c*. A sample of approximately 7×10^5 simulated minimum bias events containing at least 1 reconstructed muon track was also used for comparison.

The CSCLT system is described in detail in ref. [26]. Signals are recorded by the front-end cathode and anode electronic boards connected to the chambers. Muon track segments are found

separately in the nearly orthogonal cathode and anode planes, where the 6-layer redundancy of the system is used to measure the muon-segment BX, its pseudorapidity η, and the azimuthal angle ϕ. Up to 2 cathode and 2 anode local track projections can be found in each chamber at any BX. These are then combined into 3D tracks by requiring a timing coincidence in the trigger electronics module. The CSCs are read out in zero-suppressed mode, requiring a pretrigger that depends on specific patterns of cathode and anode local tracks. Hence, the CSC readout is highly correlated with the presence of CSCLT segments. This feature is taken into account when measuring the local trigger efficiency.

The CSCLT efficiency measurements are performed by using a minimum bias event sample and a sample of events containing J/ψ and Z decays to dimuons. A sample of 2.5 million simulated minimum bias events containing at least 1 muon at the generator level is also used for comparison, as well as samples of simulated events containing a J/ψ or a Z decaying to a pair of muons. Muon candidates from J/ψ decays are characterized by $p_T < 20\,\text{GeV}/c$, whereas muon tracks from Z decays have $p_T > 20\,\text{GeV}/c$.

When a muon passes through an RPC, it creates a pattern of hits that contains information about the bending of the track and thus about the p_T of the muon. Hardware processors compare the observed pattern within a segment with predefined patterns corresponding to certain p_T values. The pattern comparator trigger (PACT) allows for coincidences of 4 hits out of 4 stations (4/4) and 3 hits out of 4 stations (3/4). The latter are assigned a lower quality than the former. In the barrel, higher quality triggers are also possible with 5/6 and 6/6 coincidences. If the observed hits match multiple patterns, the muon candidate with the highest quality and highest p_T is selected. All candidates are first sorted by quality, then by p_T and the L1 RPC regional trigger delivers the 4 best muons in the barrel and the 4 best muons in the endcap to the global muon trigger (GMT).

4.1 Timing and synchronization

The L1A signal, which is broadcast to all subdetectors, initiates the readout of the event. Trigger synchronization is of great importance because as simultaneous hits in multiple chambers are required for an L1 trigger, out-of-time chambers can reduce the overall trigger efficiency. Moreover, if the L1 muon trigger is generated early or late relative to the collision time, it forces readout of the entire detector at the wrong BX. For these reasons, online synchronization of the muon chambers was a priority during the early running period.

Trigger synchronization of each subsystem must be achieved at 3 levels: intrachamber synchronization, chamber-to-chamber relative synchronization, and subsystem-to-subsystem synchronization. Although each muon subsystem faced unique challenges due to differences in chamber design, trigger electronics design, and physical position on the CMS detector, the general synchronization procedures were similar. The general procedure is discussed in section 4.1.1. The details and results of the separate DT, CSC, and RPC trigger synchronization methods are found in sections 4.1.2, 4.1.3, and 4.1.4, respectively. The overall L1 GMT synchronization results are discussed in section 4.1.5.

For physics analyses, the time assigned to the muon hits once the event has been collected and fully reconstructed is also important. This is called the "offline time". For a muon produced in a proton-proton collision and with the correct BX assignment, the offline time of any muon chambers hit should be reported as t=0. Any deviations from 0 may be caused by backgrounds

such as cosmic-ray muons, beam backgrounds, chamber noise, or out-of-time pileup, or it may be an indication of new physics such as a slow moving, heavy charged particle. In section 6.2, the offline time alignment procedure and results are shown.

4.1.1 Common synchronization procedure

Track segments are promptly obtained by the local front-end trigger electronics from hits in the 4 layers of a DT chamber superlayer or the 6 layers of strips and wires in a CSC. Trigger primitives are delivered to the L1 trigger at a fixed delay with respect to the chamber local clock, which is a copy of the master LHC clock. The time of a hit caused by the passage of a particle through the muon chamber with respect to the locally distributed clock signal depends on the following:

- the muon time-of-flight from the interaction point to the chamber;

- individual chamber properties and geometrical position;

- the latency of the trigger electronics;

- the length of the cables and fibers connecting the chamber electronics to the peripheral crates.

The last 3 items are specific to each chamber and were already studied during cosmic-ray data taking, before proton-proton collisions were recorded at CMS. The synchronization with respect to the master LHC clock (and hence with the rest of CMS) is achieved by moving the phase of the locally distributed BX signal with respect to the master LHC clock.

The tool used by CMS subdetectors for the synchronization of trigger and data acquisition chains is the trigger and timing control system device (TTC) [29]. The purpose of the TTC is to distribute the machine clock signal to the various parts of the detector and broadcast the L1A "strobe" trigger signal.

Prior to the start of collisions in the LHC, each muon subsystem used cosmic-ray data or early single-beam data to adjust its TTC delays for a rough chamber-to-chamber synchronization. Additional adjustments were introduced based on calculated time-of-flight paths to each chamber. Once collision data were available, each subsystem used high-p_T muon data to refine internal delay settings so that the on-chamber clocks would be in the correct phase with respect to the LHC machine clock. This procedure was iterative. The L1 trigger is different for each muon subsystem, so the subsystem-specific figures of merit for synchronization are presented in the next sections.

4.1.2 DT trigger synchronization

To optimize the readout time of collision data, 2 independent synchronization steps ("coarse" and "fine") are carried out. The first refers to the chamber-to-chamber adjustment of the overall DTLT latency in terms of BX spacing units and is performed to provide equalized input to the DT regional trigger. The second refers to the tuning of the sampling phase of the DTLT to a precision of 1–2 ns to optimize the system response to muons arriving at a fixed time after the beam crossings.

Every DT is equipped with a trigger and timing control receiver (TTCrx) device that provides a parameter to adjust the clock phase between on-board electronics and the CMS master clock (TTCrx delay parameter). The latter is used to perform the fine synchronization of the DTLT and is configurable in steps of 0.1 ns.

Since it is possible to tune the TTCrx delay parameters only chamber by chamber, delays due to signal propagation between the boards equipping a single DT chamber need to be taken into account. To compensate for this effect, the DTLT internal timing was equalized using cables of appropriate lengths. The maximum skew of the clock distribution after equalization has been measured to be around 1 ns, ensuring that each chamber was intrinsically synchronous within this level of precision. Such a level of accuracy compares well with the design performance; hence the online DT software allows timing adjustments to a precision of 1 ns.

The tuning of the TTCrx delay parameter affects both readout and DTLT boards. Therefore every adjustment related to trigger timing optimization needed to be followed by an update of the DT calibration pedestals used for local hit reconstruction.

The procedure used to synchronize the DTLT with collision data is extensively described in ref. [12]. A precise measurement of the particle arrival time in a muon station with respect to the calibration pedestal (see section 3.1) can be performed for each local segment. The method exploits the staggering of the wires in the SLs. The ionization electrons in the 2 odd layers drift in a direction opposite to that in the 2 even layers. In the case of a 4-hit track, 2 segments can be reconstructed, one from the even hits and the other from the odd hits. If the reference time does not have the correct phase with respect to the time of passage of the particle, the 2 segments do not coincide but are separated by a time that depends on the reference pedestal time. This time difference can be measured precisely via an optimization procedure that uses this difference as a free parameter in the reconstruction.

During commissioning of the detector with cosmic-ray muons, the DTLT response was studied to characterize the DTLT performance with respect to the relative phase between the particle's crossing time and the rising edge of the bunch crossing TTC signal. This allowed identification of the timing phases within a bunch crossing, where the system has optimal performance. These were collected for each chamber and used as a startup reference to time in the detector during bunched beams operation.

The timing distribution of reconstructed segments matched to global muons originating at the interaction vertex was computed as soon as sufficient bunched beam data were available. The timing distribution was then compared to the set of optimal timing phases previously measured from cosmic data. This was used to estimate additional corrections that optimize the DTLT performance to maximize the BX identification efficiency of global muons. The procedure was iterated 4 times to reach the final configuration.

Figure 10 (upper left) shows the time distribution of the highest quality local DT trigger primitives. These trigger primitives were constructed with at least 7 out of 8 layers in a chamber and were found in the DTLT readout window of triggering stations crossed by offline reconstructed muons from LHC collisions. In this figure, data from all DT chambers were summed together.

Out-of-time primitives symmetrically populate the bins to the right and to the left of the correct BX. The pre- and post-triggering rates of the highest quality DTLT primitive are both on the order of 2%. These are mainly due to the presence of DTLT out-of-time "ghosts" that can occasionally be generated together with in-time trigger primitives. As outlined in section 4.3, this effect has been carefully investigated. Under 2010 timing conditions and LHC luminosities, the efficiency to deliver a trigger primitive at the correct BX and the low rate of out-of-time triggers are in good agreement with Muon TDR expectations and simulation studies (see appendix B).
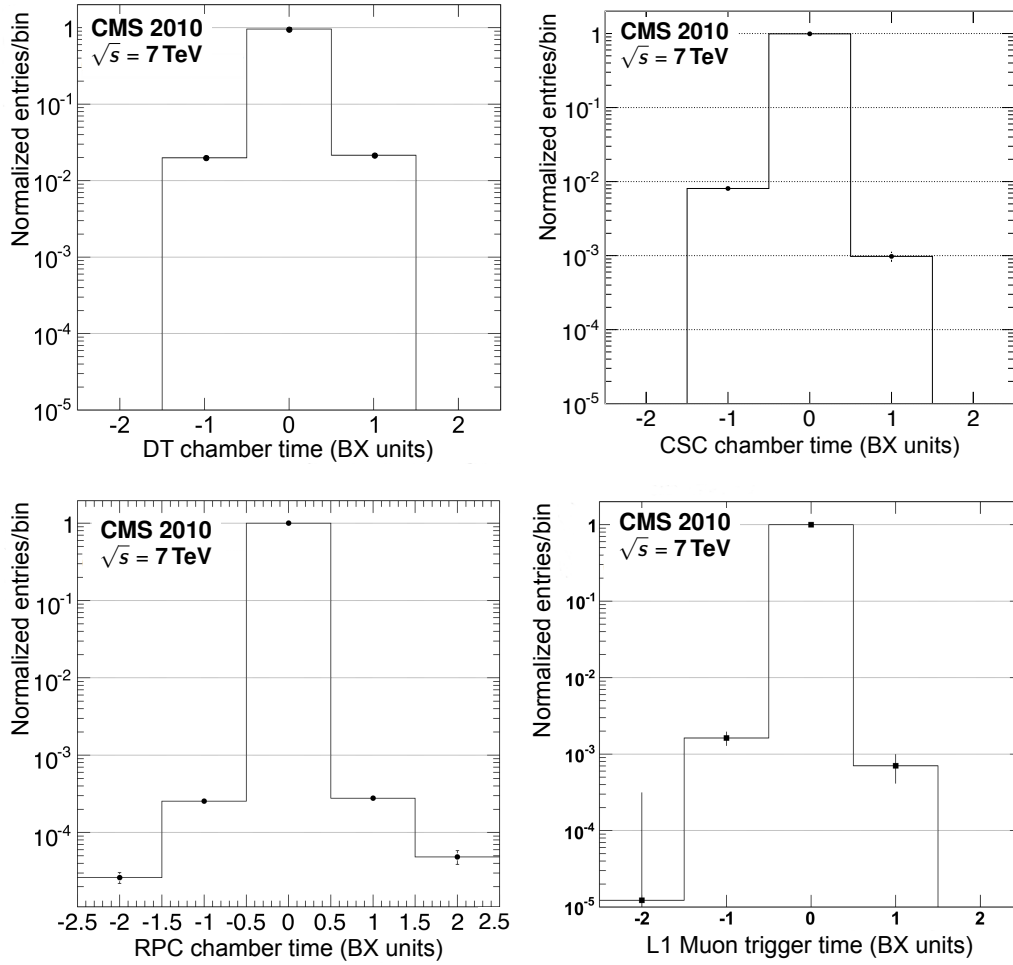
Figure 10. Time distributions for the chamber-level trigger primitives for (upper left) DT and (upper right) CSC hits, and for (lower left) RPC hits, relative to the true event BX (1 BX unit = 25 ns). In each distribution, data from all chambers were summed together to show the overall subsystem synchronization. (lower right) Distribution of the combined L1 single-muon trigger.

The final set of DTLT timing corrections was applied by the end of August 2010. Data collected during the remaining 2010 LHC operation period were analyzed to compute a further set of adjustment parameters, which were tested at the beginning of the 2011 LHC run.

4.1.3   CSC trigger synchronization

Data from the anode wires and cathode strips of the CSCs are split into 2 paths, one feeding the readout for data acquisition and the other the trigger. Within a chamber, the CSC trigger object is called a local charged track (LCT) (see section 4.1.3). An LCT is defined by a pattern of hits on at least 4 layers that is compatible with the straight line segment produced by a muon from a proton-proton collision [30]. The LCTs from different chambers are fed into the CSC track finder trigger hardware, which combines them to identify candidate muon tracks. These candidate tracks are then passed to the main CMS L1 trigger system. As the CMS trigger is a synchronous system,

the time associated with these LCTs is crucial for proper operation of the trigger and subsequent synchronization of the front-end readout. The LCT time is a measure of the BX in which the collision occurred, and the process of identifying this time in BX units is the "BX assignment".

The LCT is formed from a coarse time coincidence (within ± 3 BX) of

- a cathode LCT (CLCT), formed from the strip hits, and

- an anode LCT (ALCT), formed from the wire hits.

Since the anode signal timing is more precise than the cathode signal timing, the BX assignment of the LCT is determined by the ALCT time. The ALCT signal development is briefly outlined as follows. When a collision muon passes through a CSC, charge collected on the anode wire is input to a constant fraction discriminator in the anode front-end board. If the charge is above the detection threshold, a 35-ns pulse is output to the chamber's ALCT board. Because the pulse is digitized every 25 ns, the start time of the pulse will determine if the anode hit spans a time period equivalent to 1 or 2 BXs.

In forming an ALCT, the digitized hit pulses are stretched in time to the duration of 6 BXs based only on the leading edge of the pulse. The ALCT BX assignment is defined as the first BX in which 3 or more layers within the anode pattern contain a hit (to be confirmed by a coincidence of 4 or more layers). The resulting BX identification efficiency is better than 99%.

The "anode hit time" is defined as either the time of the single BX or the average time of the 2 BXs to which the hit corresponds. Averaging the chamber anode hit times over several events yields a characteristic "chamber anode time", which is sensitive to changes in the clock delays sent to the ALCT electronics boards. These delays can be adjusted in steps of 2 ns.

The average chamber anode time in a sample of reconstructed muons was correlated with the fraction of apparently early (-1 BX), in-time (BX=0), and late ($+1$ BX) ALCTs. The ALCT times were then adjusted so that they optimized the fraction of in-time ALCTs by appropriate adjustment of the clock delays for each ALCT board. After adjustment, the distribution of the difference between the ALCT time and the true event time is shown in figure 10 (upper right). This distribution is intentionally asymmetric: when 2 ALCTs measure different times, the CSC Track Finder logic chooses the later value, so the optimal performance point is set slightly earlier than the zero of the distribution.

4.1.4 RPC trigger synchronization

The RPCs possess good intrinsic timing resolution (typically below 2 ns) [31], and therefore are well suited for the task of muon triggering and BX assignment. Unlike the CSCs and DTs, the RPC system does not form trigger primitives, but the chamber hits are used directly for muon trigger candidate recognition.

The signal path can be summarized as follows:

- amplification and discrimination at the front-end boards located on the chambers;

- transmission through cables to the link boards situated on the balconies in the CMS experimental cavern;

- zero-suppression and transmission through optical fibers to the trigger electronics outside of the cavern;

- arrival at the electronics room and distribution of signals to the individual processing elements of the pattern comparator (PAC) trigger system.

Because hit signals are discriminated at the chamber level, there are different offsets for individual chambers. Signals coming from a single chamber may be shifted in time in steps on the order of 0.1 ns to achieve synchronization. By using cable length values and muon time-of-flight, it was possible to produce a first approximation of the synchronization constants. These were further refined during studies of beam halo and beam splash events. Beam splash events are recorded during intentional beam dumps about 100 m upstream from the CMS detector that result in large fluxes through the chambers of about 5 synchronous muons cm^{-2} that are parallel to the beam line.

After the start of LHC collisions, the recorded data were used to further improve the synchronization. The experimental procedure consisted of selecting global muons with tracks that would cross the RPC system. Furthermore, only the first hit from any chamber was selected, since a particle crossing an RPC may sometimes provide afterpulses. The distribution of the hit time, in units of BX, relative to the true collision time was studied for all chambers. In cases where the distribution was asymmetric or shifted, the synchronization parameters were adjusted to obtain a symmetric distribution centered at 0. This procedure was repeated 3 times and the final results are presented in figure 10 (lower left). The data used here correspond to roughly 1 million muon tracks. Hits outside the central bin contribute significantly less than 0.1%. The fraction of out-of-time hits decreased by roughly 50% after the third iteration.

4.1.5 L1 muon trigger synchronization

L1 muon triggers are formed from trigger primitives (DT, CSC) or hits (RPC) forwarded from multiple chambers. The L1 trigger assigns the triggering BX according to the assignments of the regional (e.g., muon) L1 triggers. It is determined according to a logic that depends on the muon subsystems involved and combines primitive or hit information, reducing the contribution of early/late signals from individual chambers.

The HLT filtering biases the use of normally-triggered data for studies of L1 trigger timing because out-of-time events may be rejected. Therefore, to study out-of-time L1 triggers a dedicated DAQ stream was developed to collect just the L1 trigger information from the complete CMS raw data stream, before HLT processing.

The combined L1 muon trigger time, with no minimum p_T requirement, is shown in figure 10 (lower right). This dedicated data stream did not contain the information required for reconstruction of muons and hence explicit rejection of cosmic-ray and beam halo backgrounds was not possible. In LHC running during 2010, protons were not filled into every possible 25-ns slot and so there was no proton bunch in some time slots. Therefore the L1 trigger rate attributable to cosmic rays was measured at times during the LHC orbit at which protons were not colliding within CMS. Likewise, the beam background was estimated from the L1 muon trigger rate when a single bunch was present in CMS. After contamination from cosmic-ray muons and beam halo was subtracted, the fraction of pre- and post-triggered events was below 0.2% and 0.1%, respectively. These results exceeded the Physics TDR expectations of 99% in-time triggering [32].

Table 3. Average DTLT efficiencies for the different station types for 2010 collision data and simulation. Results that include the correct BX identification (BXID) are also shown. The uncertainties include both the statistical and systematic components summed in quadrature.
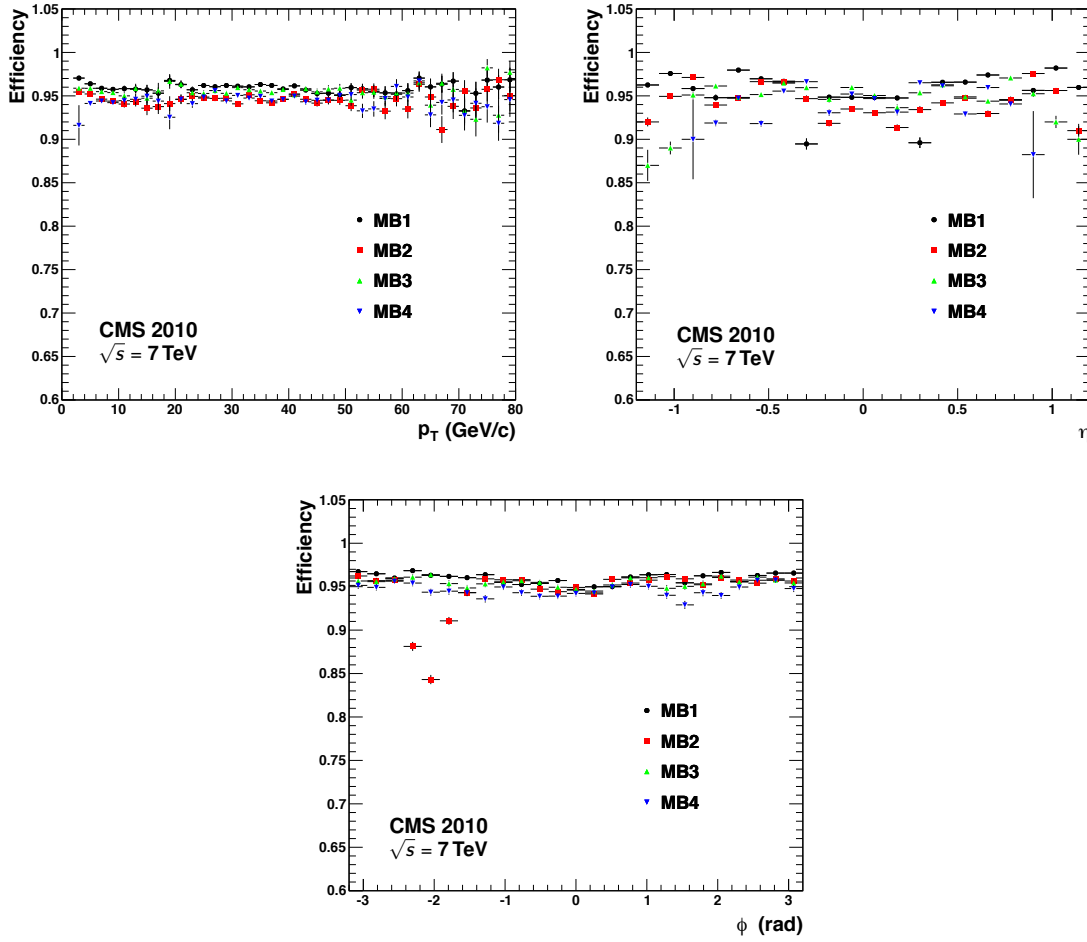
Station	DTLT Efficiency (%)		BXID Efficiency (%)	
	Data	Simulation	Data	Simulation
MB1	96.2 ± 0.1	97.9 ± 0.9	94.5 ± 0.9	96.4 ± 0.9
MB2	95.7 ± 0.8	98.0 ± 0.8	94.0 ± 0.8	96.7 ± 0.7
MB3	95.8 ± 0.9	98.3 ± 0.8	93.8 ± 0.9	96.9 ± 0.8
MB4	95.0 ± 0.1	97.1 ± 0.9	93.0 ± 0.9	95.6 ± 0.9

4.2 Measurement of the DT and CSC local trigger efficiencies

To measure the DTLT efficiency, selected events are required to be triggered by the RPC system, without any requirement on the presence of the DT trigger, which could otherwise bias the measurement. The presence of a reconstructed muon track in the event is required. To remove contamination from cosmic rays, muon candidates must have an impact parameter in the transverse and longitudinal planes within $|d_{xy}| < 0.2$ cm and $|d_z| < 24$ cm, respectively. Their pseudorapidity must be in the range $|\eta| < 1.2$ to be within the acceptance of the inner stations of the muon barrel. The number of DT hits associated with the track N_{DT} must be greater than 3. Such hits can be located anywhere along the track, and not necessarily in a single muon station. This requirement does not introduce any bias on the efficiency measurement, because at least 4 aligned hits in 1 SL are necessary to deliver a trigger primitive. Poorly reconstructed muon tracks are removed by requiring the normalized χ^2 of the track fit to be less than 10. The track transverse momentum is required to be $p_T > 7$ GeV/c to ensure that the muon reaches the outer station of the muon barrel.

To measure the DTLT efficiency in a chamber, the presence of a track segment associated with the selected muon track is required. The segment must be reconstructed with at least 4 out of 8 hits in the ϕ view. In addition, it is required that $|\psi| < 40°$, where ψ is the local track segment angle with respect to the direction to the interaction point in the CMS bending plane. This ensures that the segment is fully contained in the angular acceptance of the DTLT modules. If more than a single track segment is found in the chamber, the event is not used for the efficiency calculation. The efficiency of the DTLT in a given chamber is defined as the fraction of selected track segments with an associated trigger primitive. This definition allows the effective trigger efficiency to be measured, after elimination of inefficiencies related to geometrical acceptance that can amount to a few percent.

During the 2010 data-taking period, about 3% of the DT chambers suffered from hardware failures that affected the DTLT efficiency. Ignoring these chambers, the average DTLT efficiency in a station is 95.7%, to be compared with 97.8% obtained with simulated events. The average DTLT efficiency is shown in table 3, for data and simulation, for the 4 barrel stations. The uncertainties are dominated by systematic effects. Differences in the DTLT efficiency from station to station are caused by small shifts in the time synchronization of the local trigger electronics and differences in the average angular incidence of the muon tracks. The overall systematic uncertainty is estimated from the observed spread of the measured DTLT efficiencies over the various stations,

Figure 11. The measured DTLT efficiency as a function of the muon transverse momentum p_T, the pseudo-rapidity η, and the azimuthal angle ϕ. Results for the 4 stations are superimposed.

after ignoring stations with known hardware problems. The lower efficiency measured in the data compared with the simulation is partially due to small differences in the timing of the muon stations with respect to ideal conditions, and was a subject of further investigation during the 2011 data-taking. The DTLT efficiency as a function of the muon transverse momentum p_T, the pseudo-rapidity η, and the azimuthal angle ϕ is shown in figure 11, for the 4 stations. All the DT chambers are used for this measurement, and the inefficiency observed in the region $-2.5 < \phi < -1.5$ radians is due to a known hardware failure in a single MB2 station.

If the trigger primitive is also required to correctly identify the BX at which the muon candidate is produced, the average DTLT efficiency decreases to 93.8%. This is still over 1% better than the design performance (L1 Trigger TDR [26]). Results for the DTLT efficiency after requiring correct BX assignment are shown in table 3.

The important component of the CSCLT efficiency is the efficiency for creating CLCT candidates, since the CLCTs provide the CSC L1 trigger track finder with the critical information about the bending of a muon in the magnetic field. Two methods are used to measure the CLCT efficiency:

a "single-track matching" method and the standard CMS "tag-and-probe" method [33]. Both methods are based on tracks reconstructed using silicon tracker detector information alone (so-called "tracker tracks") to allow efficiency measurements free of any bias from the use of muon detector information in track reconstruction. Contrary to the DTLT efficiency measurement, the presence of an RPC trigger is not required in the event selection, since the RPCs only cover $|\eta| < 1.6$. As shown in section 4.1, the BX identification efficiency of the CSCs could be adjusted to exceed 99% (even better than the TDR design of 99% [26]), so out-of-time BX assignment is an insignificant contribution to CSCLT inefficiency.

In the single-track matching method, a high-quality tracker track that projects to match a track segment in a CSC station is selected. The CLCT efficiency is measured in any upstream station through which the track must have passed. If a track is matched to a segment in station ME2, then station ME1 is examined for the presence of a CLCT. If the track is matched to a segment in ME3, then ME2 is examined. Downstream of ME3, only ME4/1 exists, so only part of ME3 can be probed. In general the method is effective only for chambers in stations ME1 and ME2. Only tracker tracks that have η within the CSC geometrical coverage, $0.9 < |\eta| < 2.4$, are used. A high-quality track is identified by requiring that the transverse impact parameter $|d_{xy}|$ be less than 0.2 cm and the longitudinal impact parameter $|d_z|$ be less than 24 cm, that there be at least 11 associated hits in the silicon tracker, that the normalized χ^2 of the track fit be less than 4, that the η and ϕ uncertainties be less than 0.003, that the momentum be above 15 GeV/c, and that the relative p_T uncertainty be $\Delta p_T / p_T < 0.05$. The track must cross the chamber in which it matches a segment at least 5 cm away from the chamber's edge to ensure it is well within the geometrical coverage of the system, and it must be the only track to cross that chamber. The track is required to project to within 10 cm of a CSC track segment, $D_{\text{trk-seg}} < 10$ cm, where $D_{\text{trk-seg}}^2 = (X_{\text{trk-proj}} - X_{\text{seg}})^2 + (Y_{\text{trk-proj}} - Y_{\text{seg}})^2$, to confirm that the track indeed reached that station. In the upstream station in which CLCT efficiency is measured, a track is considered to be associated with a CLCT if it projects to within 40 cm of a CLCT: $D_{\text{trk-LT}} < 40$ cm, where $D_{\text{trk-LT}}^2 = (X_{\text{trk-proj}} - X_{\text{LT}})^2 + (Y_{\text{trk-proj}} - Y_{\text{LT}})^2$.

A track that projects into a chamber known to be inoperative because of hardware or electronic board failures is not used in the computation of the efficiency. (In 2010, typically about 8 of the 468 chambers in the system were inoperative at any given time.)

In the tag-and-probe method, dimuons from J/ψ and Z decays are used. They are, however, collected with an inclusive single-muon trigger, so that one of the muons (the probe) is unbiased by the performance of the muon system. The triggering muon (the tag) is identified as a muon by the standard muon selection criteria, involving selection of a track in the silicon tracker matched to information in the muon detectors. The probe track is not identified as a muon other than by forming an invariant mass with the tag muon near the resonance mass. The Z sample was selected from events collected using a single-muon trigger, and the J/ψ sample from events collected using a dedicated J/ψ trigger in which 2 tracks reconstructed in the silicon tracker formed an invariant mass in the J/ψ mass region, and 1 of the 2 also triggered the muon system. The tag track must fulfill the following silicon tracker track selection criteria: $|d_{xy}| < 0.2$ cm and $|d_z| < 24$ cm, $p_T > 5$ GeV/c, at least 11 hits in the tracker, and the normalized track $\chi^2 < 4$. The tag track can be in the barrel or endcap, and is required to match the HLT object that triggered the event within an angular distance $\Delta R < 0.4$, where $\Delta R^2 = (\eta_{\text{trk}} - \eta_{\text{HLT}})^2 + (\phi_{\text{trk}} - \phi_{\text{HLT}})^2$, and η_{trk}, ϕ_{trk}, η_{HLT}, and ϕ_{HLT} are the η and ϕ (in radians) values of the track and the HLT candidate, respectively. The tag track is also required

Table 4. Average CLCT efficiencies per station; the statistical uncertainties are shown.

| Station | Cathode Trigger Primitive Efficiency (%) | | | |
| | Single-Track Matching Method | | Tag-and-Probe Method | |
	Data	Simulation	Data	Simulation
ME1	97.9 ± 0.1	99.0 ± 0.1	98.7 ± 0.9	97.2 ± 0.1
ME2	97.0 ± 0.1	96.7 ± 0.1	95.6 ± 0.9	94.2 ± 0.2
ME3	–	–	96.0 ± 0.9	92.5 ± 0.2
ME4	–	–	94.5 ± 1.6	89.8 ± 0.3

to be associated with at least 2 track segments in 2 different muon stations. The probe is a tracker track fulfilling the same selection criteria as for the probe in the single-track matching method described earlier. The tag and probe tracks are also required to share the same primary vertex.

The invariant mass of the tag and probe tracks is fitted to extract the J/ψ and Z signal event yields for both the denominator and the numerator of the efficiency ratio, with the requirement that all probes in the numerator match a CLCT candidate. Several different fitting functions for peak and background are used, and the spread in the results arising from the different choices is assigned as a systematic uncertainty.

The CLCT efficiency is measured for both data and simulated events. The single-track matching method is applied to minimum-bias data, whereas the tag-and-probe method is applied to the J/ψ and Z samples. The average efficiencies from both methods are shown in table 4 for each station (although single-track matching only provides measurements in stations ME1 and ME2). For the tag-and-probe method the data are from the combined J/ψ and Z samples.

Both methods are susceptible to possible systematic effects arising from the choice of selection criteria for the tracks, CLCTs, and reconstructed segments. The tag-and-probe method involves subtraction of background events not originating from J/ψ and Z decays, and this too can introduce systematic differences. The robustness of the values for the extracted efficiencies has been examined by varying the selection criteria over a range of reasonable values. The results are stable to within 1–2% and we therefore estimate the systematic uncertainty on each value to be at this level. For the single track matching, this dominates the statistical uncertainty. For the tag-and-probe method the systematic and statistical uncertainties are of similar magnitude.

For the single-track matching method, the simulated and measured efficiencies agree, while for the tag-and-probe method the simulation slightly underestimates the trigger efficiencies. The efficiencies measured by the tag-and-probe technique tend to decrease with distance from the IP, in both data and simulation. This is consistent with a few probe muons not actually reaching the probed station because of losses in the intervening magnet yoke steel, since there is no guarantee that a probe muon actually reaches the probed station. In the single-track matching case, the track always reaches a chamber downstream of the station in which the efficiency is measured.

The CLCT efficiency measured using the tag-and-probe method is compared to simulation in figure 12 for the ME1 and ME2 stations as functions of η, ϕ, and p_T. Similar results are obtained from the single-track matching method.
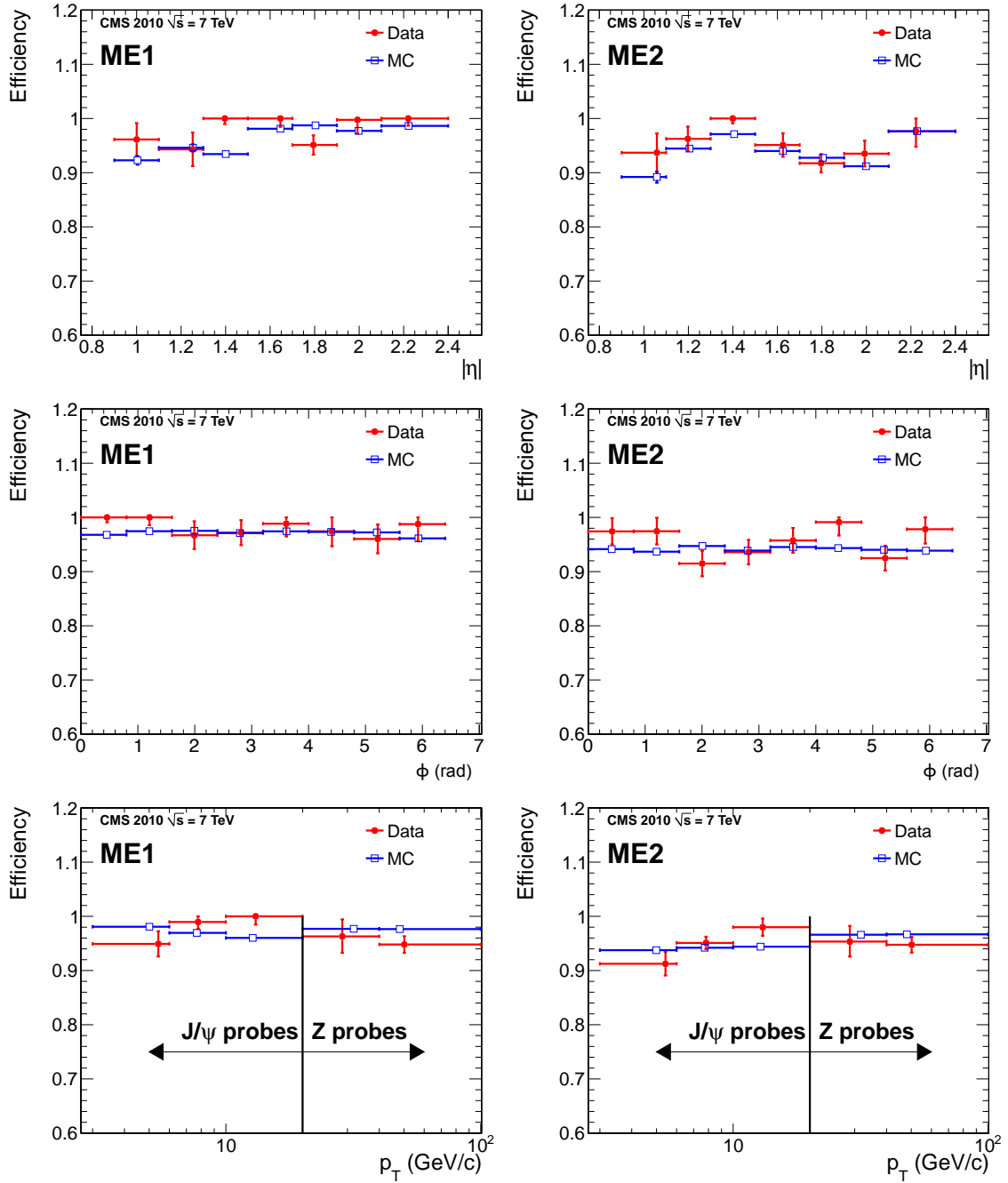
Figure 12. Comparison between CSCLT efficiencies measured using the "tag-and-probe" method (red; filled circles) and simulation (blue; open squares) as functions of muon pseudorapidity η (top), azimuthal angle ϕ (middle), and transverse momentum p_T (bottom) for the ME1 (left) and ME2 (right) stations. The vertical line on the p_T distributions separates the ranges covered by probes originating from J/ψ (left side) and Z (right side) decays. The statistical uncertainties are shown as vertical error bars. The horizontal error bars show the range of each bin, and within each bin the data point is positioned at the weighted average of all values within that bin.
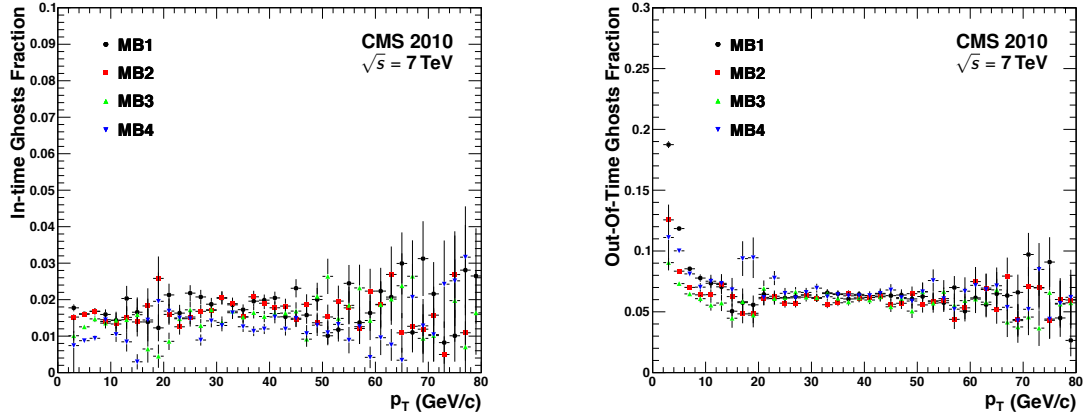
Figure 13. Left: fraction of the DTLT in-time ghosts as a function of the muon transverse momentum. Right: fraction of the DTLT out-of-time ghosts as a function of the muon transverse momentum. Results for the 4 DT stations are superimposed.

4.3 False local triggers

In the DT system, "ghost" trigger candidates can arise from additional displaced hits around the track, or if adjacent hardware trigger units share a common DT cell. The few ghosts that pass the ghost-suppression algorithm and occur at the correct BX are called "in-time ghosts". They can produce spurious dimuon trigger signals if at least 2 of them are matched together by the DTTF. The probability for the DTLT algorithm to generate such false trigger signals in a given station is defined as the number of events with 2 trigger primitives in that station, both associated with the correct BX, divided by the number of events in which at least 1 trigger primitive is delivered. The in-time ghost probability determined from the analysis of the data collected in year 2010 is shown in figure 13 (left) as a function of the muon transverse momentum, for the 4 DT stations. The result is in excellent agreement with the Trigger TDR predictions [26], which range from 2% to 4% as a function of the muon p_T.

Ghost trigger candidates assigned to the wrong BX, in addition to the candidate that identifies the correct BX, are called "out-of-time ghosts". If at least 2 such spurious local triggers are matched by the DTTF, a muon trigger candidate would be associated with the wrong BX. The probability of out-of-time ghosts in a DT station is defined as the number of events with 2 trigger primitives, one assigned to the correct and the other to the wrong BX in that station, divided by the number of events in which at least 1 trigger primitive at the correct BX is present. The out-of-time ghost probability is shown in figure 13 (right) as a function of the muon transverse momentum, for the 4 DT stations. In this plot, all out-of-time segments are included, regardless of quality. This explains why their fraction is almost a factor of 2 larger than in figure 10 (upper left) where only out-of-time segments with a quality higher than that of the segment at the correct BX are considered. The results are at least a factor 3 better than the Trigger TDR predictions. However, a direct comparison is not possible in this case because the study in the TDR was performed by using a looser definition of out-of-time ghosts [26].
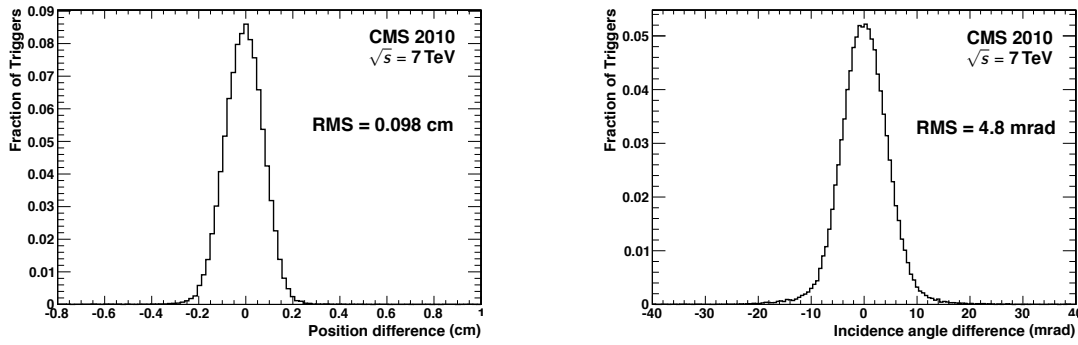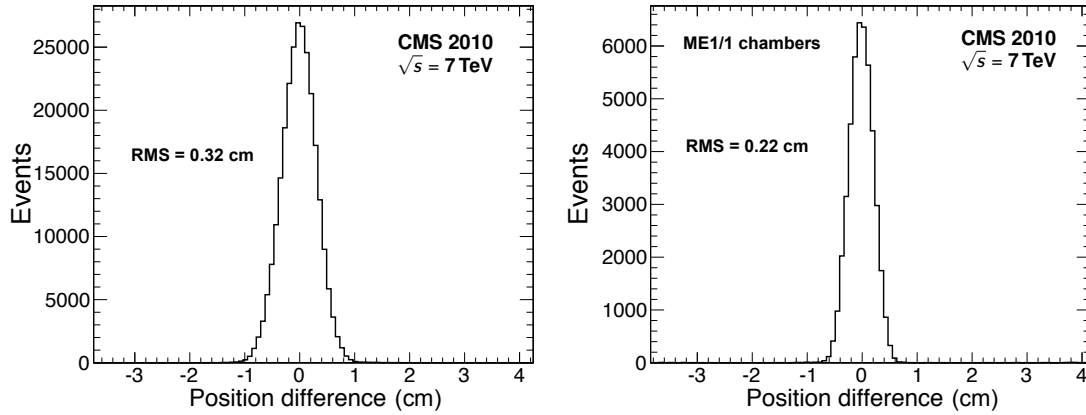
Figure 14. Left: distribution of the difference between the position of the local track segment and the DTLT segment. Right: distribution of the difference between the angle of the local track segment and the DTLT segment. Results are shown for the MB1 station.

For the CSCs, the probability of an out-of-time trigger primitive is well below 1%, as discussed in section 4.1, and so out-of-time segments are not a concern. Further aspects related to the timing and synchronization of the DT and CSC systems, which can produce out-of-time triggering, are also discussed in section 4.1.

4.4 Trigger primitive position and angular resolution

The track segments obtained by fitting the TDC information in each DT chamber are used for offline muon reconstruction, and provide an accurate determination of the position and incidence angle of the muon in the DT chamber that is independent of the DTLT output. The position and angle of the reconstructed track segments are compared with the values assigned by the DTLT to the trigger segments to determine the position and angular resolution of the DTLT primitives. As an example, figure 14 (left) shows the distribution of the difference between the position of the track segment reconstructed offline and the position of the DTLT segment for the MB1 station. The root-mean-square (RMS) of the distribution is approximately 1 mm, and is the same for every station type. This result is in agreement with previous measurements [6, 27]. Figure 14 (right) shows the distribution of the difference between the incidence angle of the reconstructed track and the DTLT segment in the MB1 DT station. The RMS of the distribution is 4.8 mrad. The result is again in agreement with previous measurements [6, 27], showing that the expected performance of the L1 trigger is achieved in terms of position and transverse momentum resolution [26].

The position resolution of the CSCLT primitive is measured by comparing the position of the CSC trigger primitive in the station to the position of the best-matched CSC track segment determined offline. Figure 15 shows the distribution of the position difference between the CSC trigger primitive and the closest matching track segment in the azimuthal direction corresponding to the strip measurement, for all CSC stations and for the ME1/1-type stations separately. The measured resolution is 3.2 mm. A smaller value of 2.2 mm is found for ME1/1, which has narrower cathode strips. The CSC TF does not depend on CSC trigger primitives for directional information, which is obtained by the position of the primitives relative to the interaction point.

Figure 15. Left: distribution of the position differences measured between trigger primitives and track segments along the strips for all CSC station types. Right: the distribution of the same quantity measured for the ME1/1 station type, in which narrower cathode strips are used.

5 Position resolution

This section presents measurements of the spatial resolutions of the DT, CSC, and RPC systems based on data recorded during the first year of LHC collisions in 2010.

The spatial resolution is determined from the distribution of hit residuals with respect to the muon trajectory. This is possible in the DTs and CSCs with no need of an external reference by using the track stubs ("segments") reconstructed with a straight-line fit of the hits in the different measurement layers. Therefore, the relative alignment of chambers does not affect the result.

The residual of hits with respect to the reconstructed segment is a biased estimator of the resolution because the hit under study contributes to the segment fit if all available hits are included in the segment, or because of the uncertainty in segment extrapolation or interpolation if the segment fit is performed after removing the hit under study. In either case, the bias can be removed by using the statistical relationship between the width of the residual distribution for layer i (σ_{R_i}) and the actual resolution (σ_i). This can be obtained from Gaussian error propagation of the explicit expression of the residual with respect to the straight line obtained from a least-squares linear fit [34, 35]:

$$\sigma_i = c_i \ \sigma_{R_i}, \tag{5.1}$$

where c_i is a factor that depends on the distance of the layer from the middle of the measurement planes, and is less than 1 in the case where the hit under study is removed from the segment, and larger than 1 otherwise. Monte Carlo (MC) studies confirm that such biases can be removed by using these corrections.

Residuals in RPC chambers, which provide a single measurement of the trajectory, are defined by extrapolating the segment of the closest CSC or DT chamber.

The following sections describe the details and results for each subdetector. The measurements are made with a pure sample of high-momentum muons from W and Z decays [33]. The muons

Table 5. Correction factors c_i of eq. (5.1) derived for the DT geometry and for the case of a segment fit including all available hits, separately in the 8 layers of the 2 r-ϕ SLs and in the 4 layers of the r-z SL. The factors depend only on the distance of the layer from the middle of the measurement planes, that is, respectively, the middle plane of the 2 r-ϕ SLs and the middle plane of the r-z SL.

Layer	1	2	3	4
SL1 (r-ϕ)	1.17	1.16	1.15	1.14
SL3 (r-ϕ)	1.14	1.15	1.16	1.17
SL2 (r-z)	1.83	1.20	1.20	1.83

Table 6. Single-hit DT resolution for r-ϕ and r-z layers expressed in μm, averaged over all sectors in each barrel wheel and station.

SL Type	Station	W−2	W−1	W0	W+1	W+2
	MB1	220±7	249±16	266±8	243±9	217±7
r-ϕ	MB2	229±12	255±10	276±9	252±6	223±15
	MB3	229±11	256±11	275±10	255±10	231±8
	MB4	287±21	325±26	349±23	315±21	284±19
	MB1	772±32	432±25	266±16	419±18	785±33
r-z	MB2	627±26	425±19	280±10	419±16	651±43
	MB3	538±30	372±13	278±14	368±18	538±27

are required to lie within the geometrical acceptance of the corresponding subdetector, and to have $p_T > 20\,\text{GeV}/c$.

5.1 DT spatial resolution

In the DT chambers, segments are reconstructed independently in the 8 layers of the 2 r-ϕ SLs and, where present, in the 4 layers of the r-z SL [21]. All available hits are included in the fit, using eq. (5.1) to obtain the resolution from residuals with the coefficients shown in table 5.

For each layer, σ_{R_i} is obtained with a Gaussian fit of the core of the segment residual distribution. The result is averaged separately for all r-ϕ and r-z layers of a chamber.

Only segments with at least 7 hits in the r-ϕ SLs and, in the innermost 3 stations, with 4 hits in r-z SL are used. In addition, segments are required to point towards the beam line, with a selection on the incidence angle at the chamber in the transverse plane of $|\psi| < 25°$.

The single-hit resolutions obtained with this method are shown in figure 16 and are summarized in table 6 separately for r-ϕ and r-z layers, averaged over all sectors in each wheel and station. The spatial resolution of the segment fitted in the whole chamber, obtained as $\sigma/\sqrt{N}$, where σ is the single-hit resolution and N the number of layers included in the fit, is given in table 7.

Several features can be noted:

- For both r-ϕ and r-z layers, the resolution of Wheel W+1 (W+2) is approximately the same as that of W−1 (W−2), as expected from the geometric symmetry of the system.

- In Wheel 0, the resolution is the same for the r-ϕ and r-z layers.
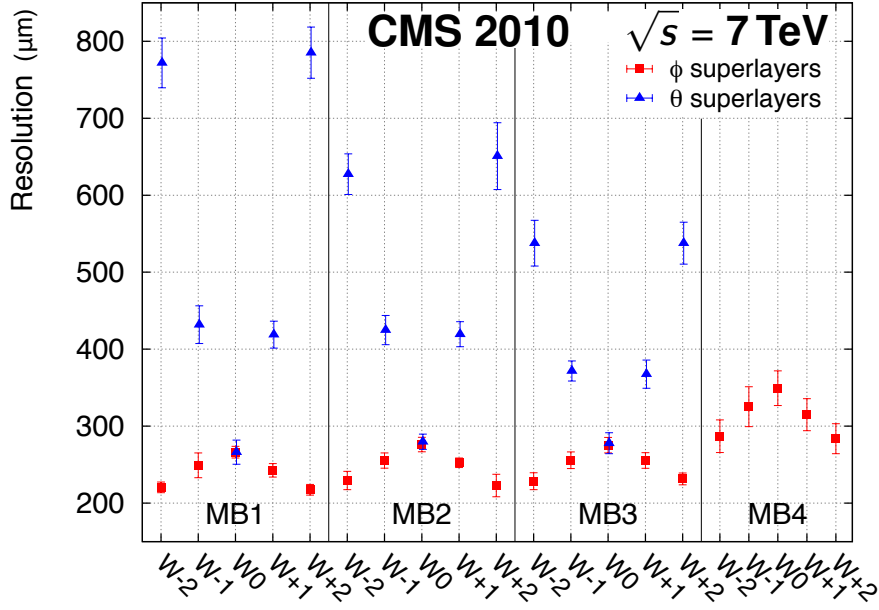
Figure 16. Single-hit DT resolution for r-ϕ and r-z layers, averaged over all sectors in each barrel wheel and station.

Table 7. The DT chamber resolution in the r-ϕ and r-z projections, expressed in μm, averaged over all sectors in each barrel wheel and station.

SL Type	Station	W−2	W−1	W0	W+1	W+2
r-ϕ	MB1	78±2	88±6	94±3	86±3	77±2
	MB2	81±4	90±3	98±3	89±2	79±5
	MB3	81±4	90±4	97±4	90±4	82±3
	MB4	101±7	115±9	123±8	111±7	100±7
r-z	MB1	386±16	216±12	133±8	209±9	393±17
	MB2	314±13	212±9	140±5	210±8	325±22
	MB3	269±15	186±7	139±7	184±9	269±14

- The resolution changes from inner to outer wheels because of the effect of the increased angle of incidence (θ) of muons. For r-z SLs, θ is the angle in the measurement plane; therefore the resolution is significantly degraded in external wheels because of the increasing deviation from linearity of the space-time relationship (eq. (3.1)) with larger angles of incidence of the particles. For r-ϕ layers, θ is the angle in the plane orthogonal to the measurement plane; the larger angle in external wheels results in longer paths inside the cells that increase the number of primary ionizations, causing a slight improvement in the r-ϕ resolution.

- The poorer resolution of the r-ϕ layers in MB4 compared to MB1–MB3 is because in this station, where a measurement of the longitudinal coordinate is missing, it is not possible to correct for the actual muon time-of-flight and signal propagation time along the wire. In particular, the signal propagation time along the wires is up to about 9.8 ns, which corresponds

to differences in reconstructed position of up to about 540 μm. This correction can be applied at a later stage, during the fit of a muon track using all stations.

For comparison, the single-hit resolution obtained in a test beam is about 190 μm for normal incidence on the chamber, with a deterioration to about 450 μm for an incident angle of 30° in the cell measurement plane and improving to about 150 μm for an incident angle of 30° in the orthogonal (non-measurement) plane [27]. The observed resolution is that expected from simulation, given the distribution of the incident angle for muons in CMS, and is in agreement with Muon TDR expectations.

5.2   CSC spatial resolution

The spatial resolution of the CSCs is determined by the properties (geometrical and operational) of the chambers, but can vary with the kinematic properties of the detected muons, and can depend on the details of the reconstruction of the hit positions. The chamber gas gain (how large a signal results from the passage of an ionizing particle through the gas) is affected by changes in atmospheric pressure, and such changes are also reflected in variation of spatial resolution. In the following characterization of the spatial resolution, the measurements are averaged over time periods of months so pressure variations tend to average out.

The precisely measured coordinate in the CSCs is that measured by the strips, since it is in this direction that muons are deflected by the CMS magnetic field, and thus is crucial for input to the L1 trigger for estimation of the p_{T} of a muon trigger candidate. In global coordinates this is approximately the azimuthal direction, but the results presented here are expressed in coordinates local to an individual chamber. To match the endcap CMS geometry, the CSCs have trapezoidal shape so that they can be assembled in concentric rings, and the strips in a CSC are radial, approximately projecting to the beamline (z axis), with each strip subtending a fixed azimuthal angle. This means that the strip width progressively increases as the radial distance from the beamline increases, as shown in table 8, and so the resolution within a given CSC depends on the radial position. It is thus natural to measure the resolution in units of strip width, and the results are quoted in terms of the fractional position s within a strip, where $-0.5 < s < 0.5$. To convert a resolution from strip width units to standard units the value is multiplied by the mean strip width $\langle w \rangle$ within the CSC; these values are also shown in table 8.

The spatial resolution in a CSC layer depends on the relative position at which a muon crosses a strip: it is significantly worse for a track crossing the center of a strip than for one crossing near an edge where the induced charge is shared between the strip and its neighbor. To compensate, alternate layers in a CSC are staggered by half a strip width, except in the ME1/1 chambers where the strips are very narrow and the effect is small [2, 36, 37]. As a measure of the resolution, the Gaussian σ resulting from a Gaussian fit to the core region of the distributions of the residuals is used. For the CSCs with staggered layers, separate distributions of the residuals are formed for hits in the central half of any strip and for hits lying outside this central region, and the distributions are fit separately giving a "central" σ_{c} and an "edge" σ_{e}. Both of these measurements are combined according to

$$\sigma_{\text{chamber}} = \left(\frac{3}{\sigma_{\text{e}}^2} + \frac{3}{\sigma_{\text{c}}^2} \right)^{-1/2}. \tag{5.2}$$

Table 8. Selected physical specifications of the CSCs, including the range of strip widths, the average widths, and the strip angular widths. For more information, see ref. [2].

Ring	Strip width w (mm)	$\langle w \rangle$ (mm)	Strip angular width (mrad)
ME1/1	4.4–7.6	6.0	2.96
ME1/2	6.6–10.4	8.5	2.33
ME1/3	11.1–14.9	13.0	2.16
ME2/1	6.8–15.6	11.2	4.65
ME2/2	8.5–16.0	12.2	2.33
ME3/1	7.8–15.6	11.7	4.65
ME3/2	8.5–16.0	12.2	2.33
ME4/1	8.6–15.6	12.1	4.65

Table 9. Correction factors c_i for 5-hit fits in the CSCs.

Layer	1	2	3	4	5	6
ME1/1 chambers	0.69	0.84	0.905	0.905	0.84	0.69
ME1/2 edge	0.59	0.73	0.87	0.87	0.73	0.59
ME1/2 center	0.80	0.91	0.94	0.94	0.91	0.80
All others edge	0.56	0.70	0.86	0.86	0.70	0.56
All others center	0.83	0.93	0.95	0.95	0.93	0.83

For the non-staggered ME1/1, the following expression is used:

$$\sigma_{\text{chamber}} = \left(\frac{6}{\sigma_{\text{layer}}^2} \right)^{-1/2} = \frac{\sigma_{\text{layer}}}{\sqrt{6}}. \tag{5.3}$$

In eqs. (5.2) and (5.3), σ_c, σ_e, and σ_{layer} are the layer resolutions calculated by eq. (5.1). The 5-hit fit is used to estimate the width of the distributions of the residuals. The correction factors c_i for different CSC types are listed in table 9.

To reduce backgrounds, the following selection criteria were applied to the hits and segments that were used to measure the resolution:

- 6 hits on a segment;

- $\chi_{\text{seg}}^2/\text{dof} < 200/8$ and $\chi_{\text{seg strip-fit only}}^2/\text{dof} < 50/4$, where dof is the number of degrees of freedom;

- exclude segments with largely displaced hits (leading to residuals of >0.2 strip widths);

- segment points roughly towards the interaction point ($|dx/dz| <0.15$ and $|dy/dz| <1.5$ in local coordinates, where y is measured along and x is perpendicular to the strips);

- reconstructed cluster charge Q_{3x3}, which is defined as the sum of the elements of a 3x3 matrix (3 strips x 3 time slices), is in a reasonable range ($150 < Q_{3x3} < 2000$ ADC counts (figure 17); hits with high charge are often distorted by δ electrons;
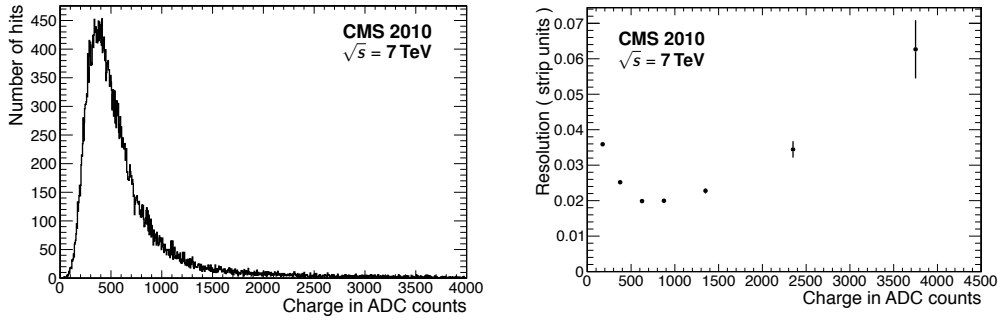
Figure 17. Left: charge distribution Q_{3x3}. Right: variation of the CSC layer resolution as a function of Q_{3x3}.

Table 10. Average CSC position resolutions (μm) for each chamber type comparing cosmic and collision data with Monte Carlo (MC) simulation. The uncertainty on the values is discussed in the text.
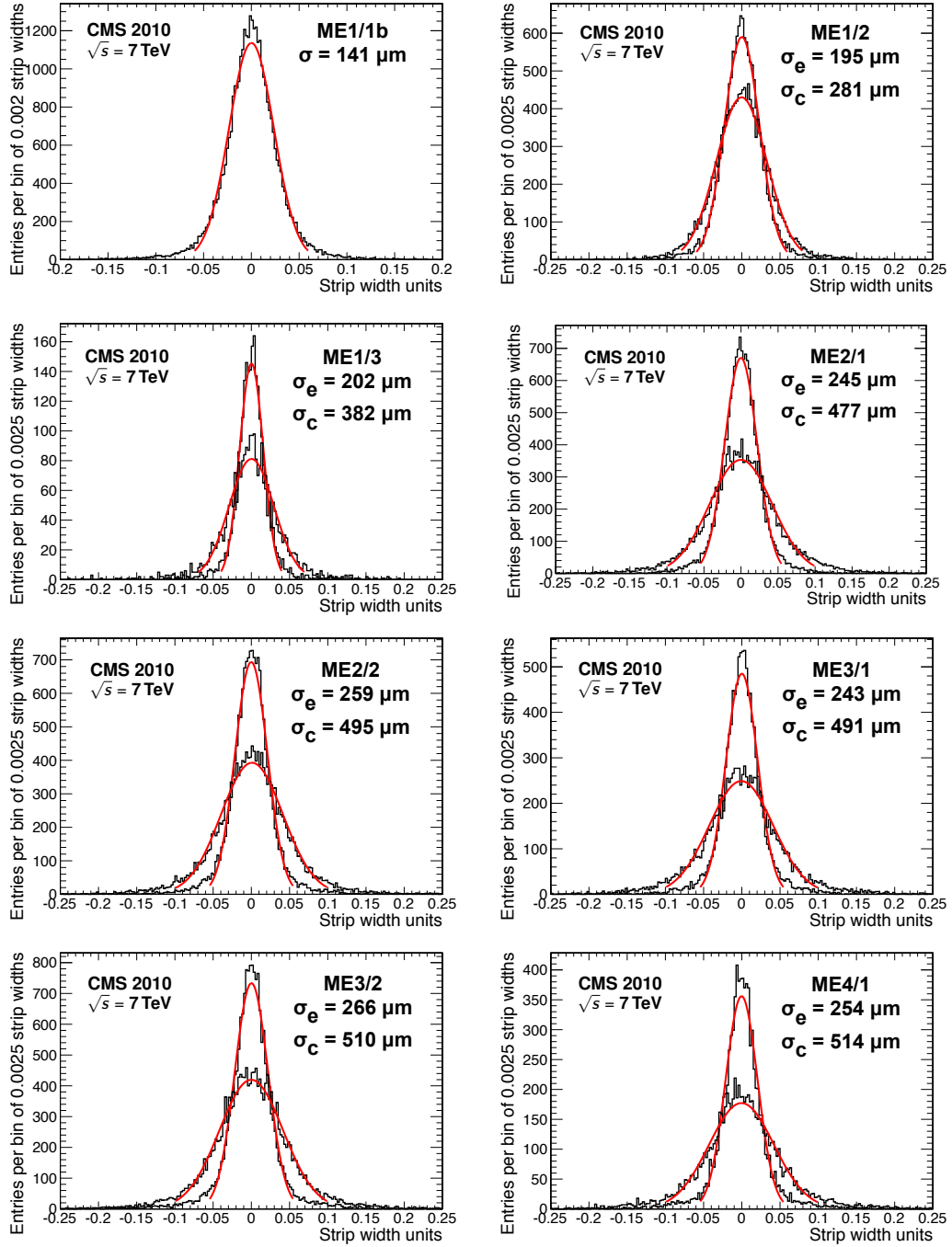
	Chamber type							
Run type/year	ME1/1	ME1/2	ME1/3	ME2/1	ME2/2	ME3/1	ME3/2	ME4/1
Cosmics 2009	73	109	135	147	162	143	200	218
Cosmics 2010	70	110	136	147	164	144	196	205
Collisions 2010	58	92	103	126	132	126	136	131
pp MC 2010	37	82	110	121	152	119	155	119

- for proton-proton collision data, require a well reconstructed muon with transverse momentum $p_T > 20\,\text{GeV}/c$ (reconstructed using muon chamber and central tracker information) within $\Delta\eta < 0.07$ of the segment.

These requirements are similar to those used in previous studies [10].

The distributions of the residuals for each chamber type are shown in figure 18. The distributions agree reasonably well with a single Gaussian distribution in the central region. The fits shown are used to extract the value of the resolution, which is then scaled by the average strip width per chamber. The measured chamber resolutions obtained by using eqs. (5.2) and (5.3) are summarized in table 10. The uncertainties on the widths from the Gaussian fits vary from 2% to 3%, corresponding to statistical uncertainties of 2–4 μm on the values in the table.

Once the chamber gas mixture and operating high voltages are fixed, the specific values for position resolution still depend on the range over which the Gaussian fits are performed, on the momentum spectra of the muons examined, and on the atmospheric pressure. The datasets used in table 10 average over periods of several weeks so that atmospheric pressure effects are also averaged, and the muon momentum spectra are similar. The similarity of the values from the cosmic datasets in 2009 and 2010 show that this procedure provides a consistent and robust measure of the CSC spatial resolution. The resolutions obtained from cosmic-ray muons are somewhat worse than those from muons with $p_T > 20\,\text{GeV}/c$ produced in proton-proton collisions. The cosmic-ray muons are of lower average momentum, arrive uniformly distributed in time, and have larger variation in angles of incidence, all of which tend to lead to poorer spatial resolution. The agreement between the resolutions determined from simulated collision data and those obtained from real data

Figure 18. Distributions of spatial residuals for the different CSC chamber types, corrected per layer according to eq. (5.1). The residuals are measured in units of strip width, and for chambers with staggered layers, the distributions for both the center (σ_c) and edge (σ_e) of the strip are shown. The curves are the results of simple Gaussian fits to the central region (within $\pm 2.5\sigma$) of each distribution.

2013 JINST 8 P11002

Table 11. Strip widths for the RPCs. The numbers in parentheses correspond to the disks/stations that have the same strip width, i.e., RE(2,3) means RE±2 and RE±3.

Barrel		Endcaps			
Layer	Width (cm)	Ring	Average width (cm)	Ring	Average width (cm)
RB1in	2.28	RE1/2/A	2.38	RE(2,3)/2/A	2.55
RB1out	2.45	RE1/2/B	2.09	RE(2,3)/2/B	2.23
RB2in	2.75	RE1/2/C	1.74	RE(2,3)/2/C	1.95
RB2out	2.95			RE(1,2,3)/3/A	3.63
RB3	3.52			RE(1,2,3)/3/B	3.30
RB4	4.10			RE(1,2,3)/3/C	2.93

is reasonable, considering that the dependence of the chamber gas gain on atmospheric pressure is not simulated. The MC value for ME1/1 is notably lower than the real value because the MC used the design HV, which was lowered by 4% during the 2010 running to increase the lifetime of the chambers while still providing the required design resolution.

All measured resolutions are close to and most even exceed the requirements noted in the CMS Muon TDR [3], which called for $75 \, \mu\text{m}$ for the ME1/1 and ME1/2 chambers and $150 \, \mu\text{m}$ for the remaining chambers.

5.3 RPC resolution

In the CMS muon system, RPCs are used as trigger detectors; in addition, hits are provided for reconstruction and muon identification. To measure the resolution of the RPC system, DT and CSC track segments were extrapolated with the technique explained in section 7. The coordinates of the extrapolated point were then compared with those of the reconstructed RPC hit, i.e., the average coordinates of the strips fired by the muon.

The RPC hit resolution depends on the strip width (table 11), the cluster size (table 12), and the alignment of the RPC chambers. Since no alignment constants are applied during muon reconstruction because of the coarse resolution of the RPCs, the RMS values are shown with and without alignment in table 13. The measured spatial resolutions are shown by chamber type in table 14 and are between around 0.8 and 1.3 cm. The cluster size measured in strip units (table 12) decreases for increasing radial distance r from the beam line, following the increasing strip size (table 11). An example of a residuals distribution fitted with a Gaussian is shown in figure 19. The Gaussian fit results for all the different distributions of the residuals (table 14) constitute the definitive resolution measurements for the RPC system. As expected, a clear correlation can be seen between RPC resolution and strip width by comparing tables 11 and 14.

6 Time resolution

In addition to a measurement of the track position and direction, the DTs and CSCs provide a measurement of the arrival time of a muon in a chamber. The RPCs also provide a very good time measurement. The resolution of these measurements is discussed in the following sections.

Table 12. Measured average cluster sizes in strip units for different RPC strip widths.

Barrel		Endcaps			
Layer	Cluster size (strip units)	Ring	Cluster size (strip units)	Ring	Cluster size (strip units)
RB1in	2.20	RE1/2/A	2.08	RE(2,3)/2/A	1.88
RB1out	2.12	RE1/2/B	2.29	RE(2,3)/2/B	2.01
RB2in	1.96	RE1/2/C	2.27	RE(2,3)/2/C	2.46
RB2out	1.93			RE(1,2,3)/3/A	1.64
RB3	1.80			RE(1,2,3)/3/B	1.57
RB4	1.63			RE(1,2,3)/3/C	1.80

Table 13. Residuals distribution RMS, with and without alignment (Align) for different RPC strip widths.

RMS Barrel			RMS Endcaps					
Layer	Align (cm)	no-Align (cm)	Ring	Align (cm)	no-Align (cm)	Ring	Align (cm)	no-Align (cm)
RB1in	1.23	1.24	RE1/2/A	1.07	1.08	RE(2,3)/2/A	1.37	1.42
RB1out	1.32	1.36	RE1/2/B	0.99	1.00	RE(2,3)/2/B	1.27	1.32
RB2in	1.56	1.72	RE1/2/C	1.09	1.10	RE(2,3)/2/C	1.10	1.14
RB2out	1.54	1.55				RE(1,2,3)/3/A	1.70	1.77
RB3	1.60	1.61				RE(1,2,3)/3/B	1.68	1.73
RB4	1.93	1.95				RE(1,2,3)/3/C	1.42	1.48

Table 14. Position resolution (σ) per chamber type for the RPCs with alignment. The uncertainty on each resolution value is smaller than 0.01 cm.

Barrel		Endcaps			
Layer	σ (cm)	Ring	σ (cm)	Ring	σ (cm)
RB1in	0.81	RE1/2/A	0.94	RE(2,3)/2/A	1.07
RB1out	0.90	RE1/2/B	0.88	RE(2,3)/2/B	0.96
RB2in	1.03	RE1/2/C	1.05	RE(2,3)/2/C	0.86
RB2out	0.99			RE(1,2,3)/3/A	1.11
RB3	1.06			RE(1,2,3)/3/B	1.28
RB4	1.32			RE(1,2,3)/3/C	1.10

6.1 Time measurement in the DTs

The arrival time of a muon track in each DT chamber is reconstructed as follows. The distance of all hits from the anode wire includes an offset common to all hits, which is taken as a free parameter in the segment fit [38]. Assuming a constant drift velocity, this common displacement corresponds to a shift in the time of the track, henceforth called local time, with respect to the mean value of the times of the sample of prompt high-p_T muon tracks used during the calibration
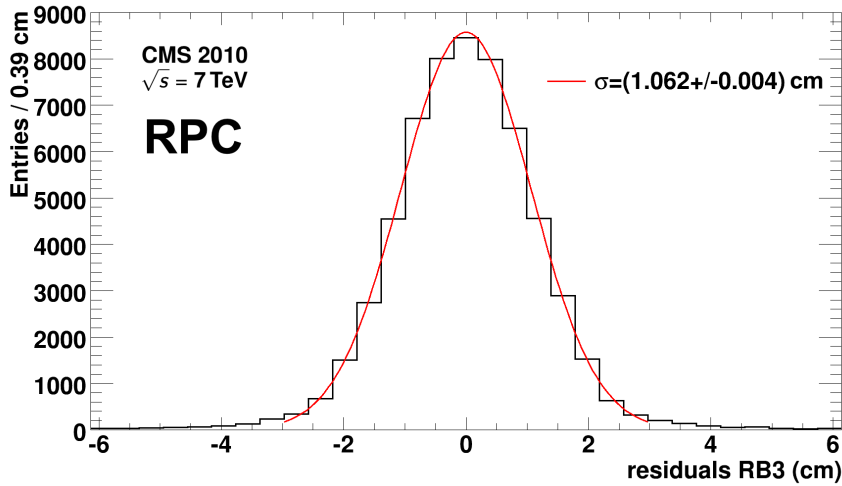
Figure 19. Residuals distribution with a Gaussian fit for RB3 of the barrel RPC system in local *x* coordinates.

process (cf. section 3.1). This common shift takes into account variations in the arrival time of the muon caused by different bending angles of tracks for different p_T values, and to uncertainties in the calculation of the propagation time of the signal along the wire. The distribution of these local times, as measured in the r-ϕ projection in a sample of high-p_T prompt muon tracks (p_T > 10 GeV/c), is shown in figure 20; the overall RMS resolution is better than 2.6 ns. For a given track, the spread in the time measurement in different chambers is typically less than 0.2 ns. The tail at low values is due to the inclusion of δ-ray hits in the fit, which may mask the genuine track hit in the same cell. Hits originating from δ-rays can be removed with a quality cut.

6.2 Offline CSC timing alignment

The CSC hit time is based on the cathode signal, which is amplified, shaped, and then sampled every 50 ns. Eight 50-ns samples are saved with the first 2 bins serving as dynamic pedestals [24]. The peak time of the pulse is found from a simple comparison of the shape with the known analytical form of the pulse shape delivered by the cathode electronics. The measured single hit resolution is 5 ns [10]. Using calibrations and muons from collisions, offsets were derived to shift the average hit time for each chamber to 0. These offsets are applied during reconstruction. To define a CSC segment time, the cathode hit times are combined with the anode hit times as defined in section 4.1.3. A Gaussian fit to the resulting segment time distribution (figure 21) yields a resolution measurement of about 3 ns.

6.3 RPC time measurement capability

Double-gap RPCs operated in avalanche mode have demonstrated the ability to reach an intrinsic time resolution of around 2 ns [39]. This has to be folded in with the additional time uncertainty coming from the time propagation along the strip, which contributes about 2 ns, plus the additional jitter that comes from small channel-by-channel differences in the electronics and cable lengths, again on the order of 1–2 ns. These contributions, when added quadratically, give an overall time
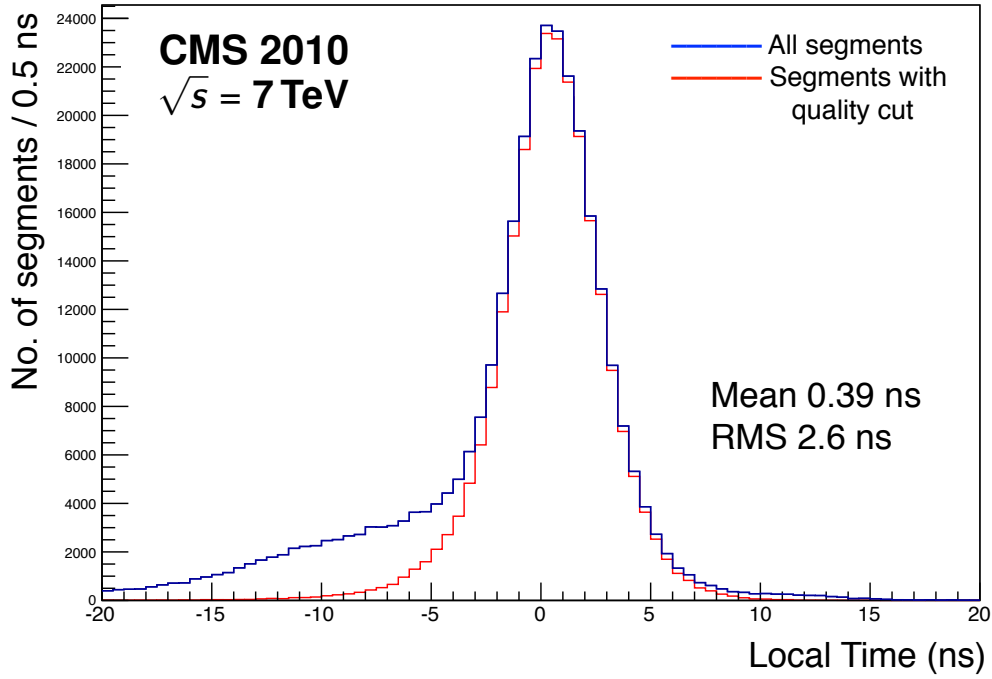
Figure 20. Distribution of the local times, as measured in the r-ϕ projection of DT chambers in a sample of a high-p_T prompt muon tracks. The distribution of all segments (blue line) shows a clear tail from δ-rays; also shown is the distribution of segments after a χ^2 quality cut (red line).
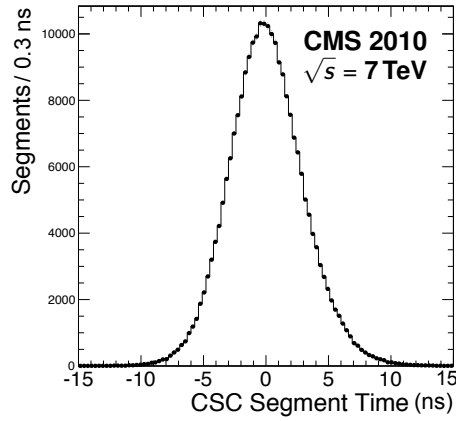
Figure 21. The CSC segment time distribution for muons with $p_T \geq 20\,\mathrm{GeV}/c$.

resolution of better than 3 ns. This is much smaller than the 25 ns timing window of the RPC data acquisition system (DAQ) in CMS, which therefore represents the achievable time precision.

7 Local reconstruction efficiency

The global reconstruction of muons relies on the local reconstruction of objects inside the individual muon chambers. The 3 muon detector systems (DT, CSC, and RPC) use different techniques to register and reconstruct signals originating from charged particles traversing them. Still, in all cases the basic objects are "reconstructed hits" or "rechits" (i.e., 2D or 3D spatial points with assigned uncertainties) and segments, obtained by fitting straight lines to the reconstructed hits.

In this paper we do not present reconstructed muon efficiencies [15] or muon trigger efficiencies since they convolute detector performance with other aspects of the CMS detector, trigger, and software. Instead we restrict our measurements to the level of local reconstruction and local trigger. This means restriction to the reconstruction of hits and track segments for muons in the muon chambers, and to the formation of local trigger objects based on chamber information that are passed on to the central CMS muon trigger system. Inefficient regions and non-functional electronic channels in the muon system were in general not excluded from the efficiency calculations, but if an entire CSC failed to provide any rechits at all, it was excluded. At any time in 2010 about 8 of the total 468 CSCs (1.7%) in the system were non-operational due to electronic failures like this. The fraction of non-operating electronic channels in the CSC system was otherwise small. In the DT system, the fraction of non-operational channels was very small (less than 1%; see appendix A).

The track segment reconstruction in the barrel DT chambers proceeds as follows: first, a hit reconstruction consisting of deriving spatial points from the TDC time measurements; second, a linear fit of these points in the 2 projections of a chamber (8 ϕ-layers and 4 θ-layers), to perform a local pattern recognition and obtain reconstructed segments. The first step starts with the calibration of the TDC output to get the real drift times (see section 3.1) of the ionized charge within the tube. Since a DT cell is 42 mm wide and has a central wire, the maximum drift distance is 21 mm. Then, multiplying the drift times by a known drift velocity, 2 space points (rechits) are obtained, left and right, at equal distance from the wire. These are the inputs to the linear fit that attempts to associate the majority of rechits to a segment. Hits that are inconsistent with the fit, yielding high segment χ^2 values, are discarded. At least 3 rechits from different layers are required to build a segment.

In the endcap CSCs, the rechit reconstruction is based on information from the strips (local x or ϕ coordinates) and wires (local y coordinate). A rechit is built only if signals from both strips and wires are present in a given layer. The strip width varies between 0.35 and 1.6 cm for different chamber sizes and locations, and a typical muon signal is contained within 3 to 6 strips. The charge distribution of the strip signals is well described by a Gatti function [40–42], which is the basis of the local x coordinate reconstruction. The center of gravity of the shower shape induced on a group of contiguous strips is obtained by using a parameterization of the expected Gatti shower shape distribution depending on the measured signals, and on the local strip width and other characteristics of the specific CSC type. This is considerably faster than an explicit fit to the expected Gatti shower shape to extract the position, and just as precise. The uncertainty in the estimated position is also extracted from a parameterization of the associated measurement uncertainties obtained from studies of the CSC response in test beam and collision data. Crosstalk between neighboring strips is unfolded by using the known crosstalk matrix from the CSC calibration measurements. The CSC wire signals are read out in groups with widths between 2 and 5 cm; typically only 1 or 2 wire groups have signals due to a traversing muon. A rechit is built at each overlap of a

strip cluster with a hit wire group (or pair of hit wire groups). Each rechit has a position in terms of local ϕ (equivalent to local x) and local y. The known geometrical positions of the chambers allow the transformation of these non-orthogonal local coordinates (strips and wires are not, in general, aligned with orthogonal global coordinates (x, y, z) where z is the global z coordinate of a given CSC). The appropriate covariance matrix is also transformed from local to global coordinates, which in general introduces correlations between the global x and y positions. This matrix is used both when building track segments from rechits and in full muon track reconstruction. Segments are built from the available rechits in the 6 layers of each CSC. The straightest pattern of hits through the chamber is found by a spanning tree algorithm, using only 1 rechit per layer, and at least 3 layers. A segment is then formed by performing a least-squares fit of the selected rechits to a straight line. Rechits that are rejected are typically those that have positions distorted by the presence of δ electrons, or are very close to the edge of a chamber's sensitive region.

The inputs to the RPC local reconstruction are the strips that have signals in a given event. The strips that are next to each other are grouped into a "strip cluster", and the average position of the strips that form the cluster constitutes the reconstructed hit of a given RPC detector. The uncertainty on the measurement is set to the standard deviation of a uniform distribution (i.e., the size of the cluster along each direction divided by $\sqrt{12}$).

The tag-and-probe technique (see section 4.2), using muons from the decay of J/ψ, Υ, and Z resonances, can be used to measure muon efficiencies since such muons can be reliably identified without the use of information from the muon system. Trigger and selection requirements limit the size of the samples of such events. An alternative method based on inclusive muons can provide larger samples, especially in the forward region, and at low p_T.

Both methods require the projecting of tracks from the inner tracker region to the muon system through the detector material and magnet steel, and multiple scattering introduces dispersion between the tracks and the associated hits and segments in the muon chambers. A third method avoids this problem by using the reconstructed segments as probes to measure the efficiency for hit reconstruction in each layer of a muon chamber.

Similarly, for the specific case of the RPC system, where the chambers are firmly attached to the DTs and CSCs, segments reconstructed in the DTs or CSCs are directly used as RPC probes. They are extrapolated to the RPC layers to measure the hit reconstruction efficiency.

7.1 Segment reconstruction efficiency in the DTs and CSCs based on the tag-and-probe method

The segment reconstruction efficiency was measured by using the tag-and-probe method applied to well-identified muons from J/ψ and Z decays selected from the 2010 collision data. The same technique was applied to appropriate samples of simulated events.

As discussed in section 4.2, a single well-identified muon (the tag) of the pair from a resonance decay is required to satisfy the trigger requirements, and the other muon (the probe) is identified as such just by virtue of forming the resonance invariant mass with the tag. Since the probe does not make use of any muon system information, it can then be used to probe the efficiency of the muon detection and reconstruction. The selected probe tracks were propagated to the muon stations, starting from their point of closest approach to the interaction point. The propagation procedure allows the position of the track to be determined at any surface that it crosses. Uncertainties on the

extrapolated position due to multiple scattering agree with the MC expectations [15]. To reduce the apparent loss of efficiency that might arise from propagation uncertainties, the point of intersection of a probe track and a chamber was required to be within the sensitive volume of a chamber, away from the chamber edges by a distance of at least the uncertainty on the position of this intersection.

The presence of reconstructed segments was checked for each individual chamber crossed by the probe tracks. A "passing probe" is defined as a probe that matched a reconstructed segment using an appropriate distance criterion. The segment reconstruction efficiency for each chamber is defined as

$$\varepsilon = \frac{N_{pp}}{N_p},\tag{7.1}$$

where N_p and N_{pp} are the number of probes and passing probes, respectively, obtained after fitting the tag and probe pair to the J/ψ and Z invariant mass spectra.

The uncertainties on the efficiency are given by a Clopper-Pearson interval [43], but in cases where the efficiencies are not close to 0 or 1 we apply the binomial error formula

$$\Delta\varepsilon = \sqrt{\frac{\varepsilon\,(1-\varepsilon)}{N_p}}.\tag{7.2}$$

The efficiency was evaluated as a function of the intersection position in the chamber and of the p_T, η, and ϕ of the traversing probe track. Compared to the J/ψ, the Z dimuon sample allows higher p_T ranges to be explored. Overall, the efficiencies determined from the J/ψ and Z samples are consistent.

Because of energy losses in the traversed material, there is a minimum momentum (or p_T at a given η) threshold for muons to reach the muon detector. The p_T threshold is $\approx 1\,\mathrm{GeV}/c$ for the forward region, and increases to $\geq 3\,\mathrm{GeV}/c$ in the central region. To reduce the effect of multiple scattering on the efficiency measurement and to ensure that the muon has the energy to further penetrate all the muon stations, a requirement on the minimal p_T or p of the track probes is imposed. In the following, selections of $p_T > 10\,\mathrm{GeV}/c$ in the barrel and $p > 15\,\mathrm{GeV}/c$ in the endcap are applied (except for the p_T dependent measurement).

The overall performance of the barrel DT system is summarized in figure 22, which shows the typical segment efficiencies for each sector to be better than 95%.

Figure 23 shows the segment efficiency computed for all barrel sectors and wheels of the MB2 DT stations as a function of the local x and z coordinates, respectively (where x is along the layer, normal to the beams, and z is along the beams). The observed efficiency matches the Monte Carlo expectations all the way to the edges of the chamber. Similar distributions have been obtained for all other barrel DT stations. Figure 24 shows the segment efficiency as functions of the p_T and η of the probe track for the 4 barrel DT stations. Figure 25 shows the segment efficiency as functions of η, ϕ, and p_T of the probe track for both endcap CSC stations and comparisons with simulation.

The overall segment reconstruction efficiencies measured in the barrel (DT) and endcap (CSC) muon systems are summarized in table 15. The segment reconstruction efficiencies are susceptible to systematic uncertainties arising from the choice of selection criteria, particularly since multiple scattering can cause deviations between a projected track and the actual position of a segment in a muon chamber. In the CSC case, the position matching criteria have been varied over a range that encompasses the average expected deviation of muons attributable to multiple scattering effects
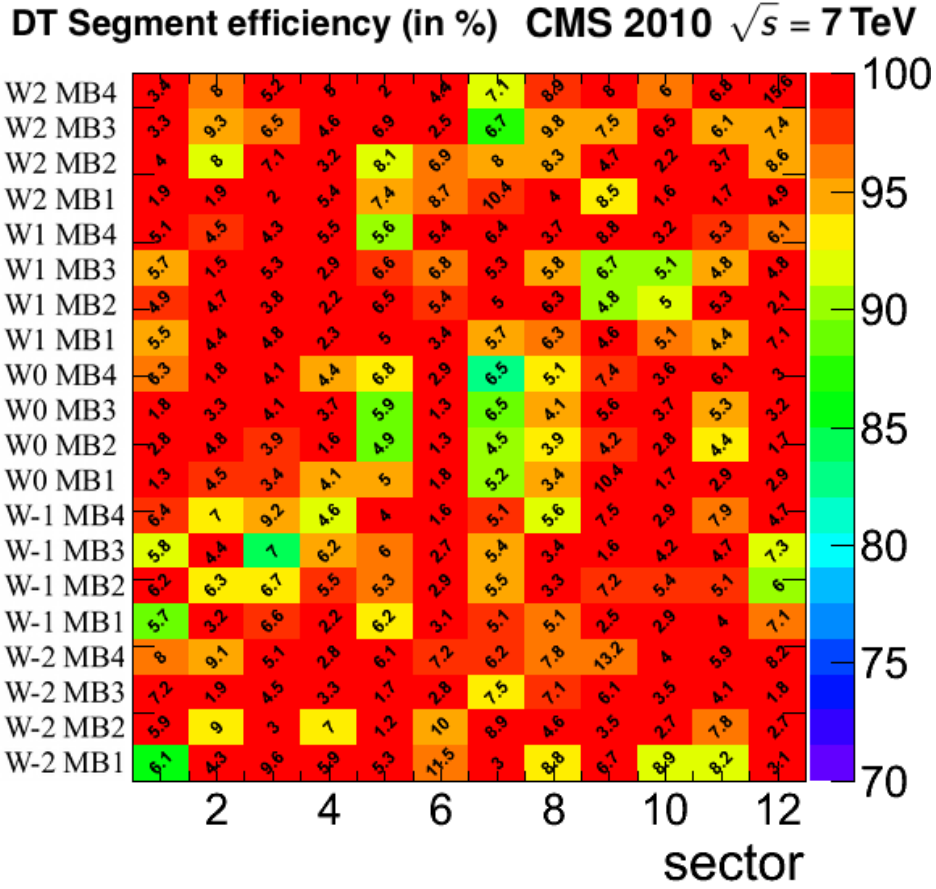
Figure 22. The DT segment reconstruction chamber-by-chamber percentage efficiency (sectors on the horizontal axis, stations and wheels on the vertical axis). Statistical uncertainties are shown as text within the boxes.

(several centimeters), and the resulting efficiencies are stable to within 1–2%. We thus assign a systematic uncertainty of 1–2% to the values in the table. Except in station 4, these systematic uncertainties dominate the statistical ones.

There is overall good agreement between data and MC simulation (see appendix B) within the uncertainties. For the CSCs, the segment efficiencies closely match the trigger primitive efficiencies of section 4.2. This is as expected, and is a crosscheck of the two independent pathways for CSC data, one to the L1 trigger and one to HLT and offline storage.

In summary, the reconstructed segment efficiency determined using the tag-and-probe method with data is at the level of 95–99% in all muon system stations with a systematic uncertainty of less than 2%. The main reasons for segment inefficiencies in the muon chambers are inefficient regions and non-operational electronic channels, although edge effects also affect the measurements, particularly transitions between the rings of CSCs.
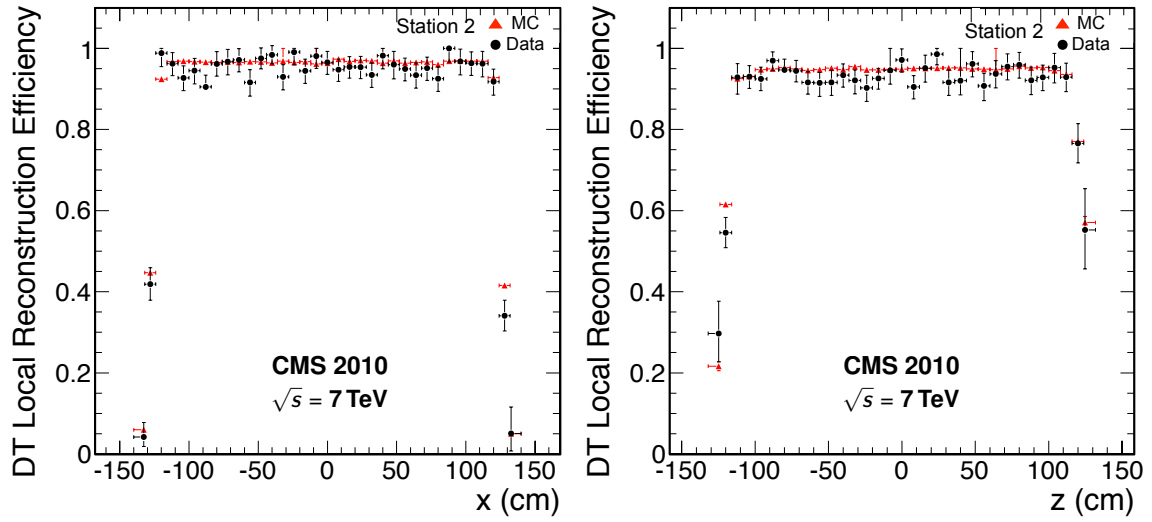
Figure 23. Segment reconstruction efficiency in the MB2 DT station and comparison with simulated data as a function of local *x* (left) and local *z* (right).
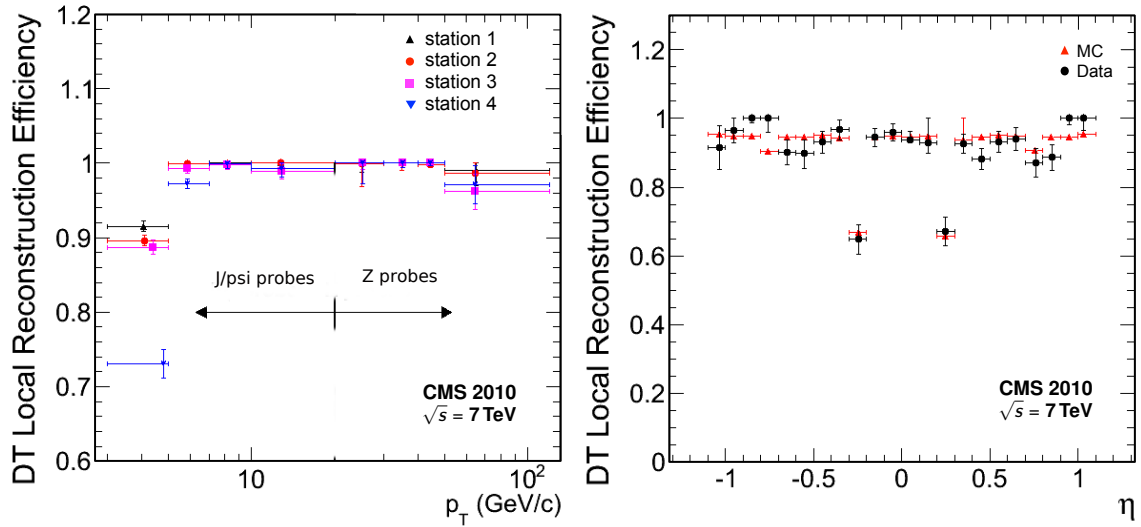
Figure 24. Segment reconstruction efficiency as a function of transverse momentum in the 4 barrel DT stations (left). Arrows indicate the ranges covered by probes originating from J/ψ and Z decays, and as a function of η in station 2 compared to simulated data (right).

7.2 Efficiency measurements from inclusive single muons

For the CSC system, detailed studies of the reconstruction efficiencies for rechits and segments in each chamber were made by using single prompt muons reconstructed from a data sample collected with jet triggers. Use of jet-triggered events avoids trigger biases in the muon sample, and a large number of muons could be obtained more rapidly than for the dimuon samples required for the tag-and-probe method. Stringent criteria, summarized in table 16, are used to select well-reconstructed muons originating from the proton-proton collision interaction point, and to reduce the contribution of non-prompt (decay) muons and hadronic punch-through.
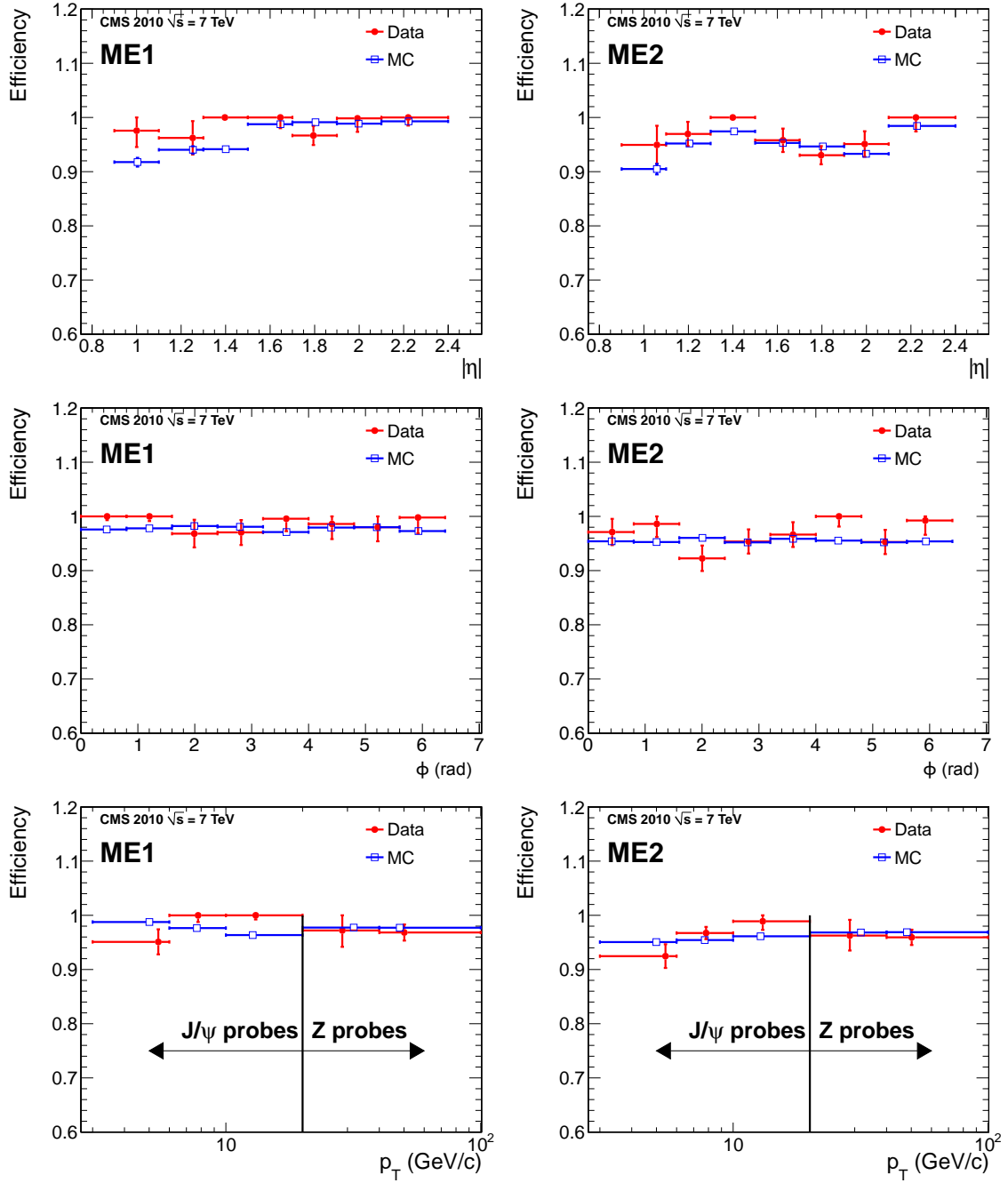
Figure 25. Comparison between measured (red; closed circles) and simulated (blue; open squares) segment reconstruction efficiencies as functions of η (top), ϕ (middle), and p_T (bottom) for endcap CSC stations ME1 (left) and ME2 (right). The vertical lines in the bottom plots separate the ranges covered by probes originating from J/ψ and Z decays. The statistical uncertainties are shown as vertical error bars. The horizontal error bars show the range of each bin, and within each bin the data point is positioned at the weighted average of all values within that bin.

Table 15. Local segment reconstruction efficiency for stations 1–4 of the barrel (DT) and endcap (CSC) muon systems.

	DT Efficiency (%)		CSC Efficiency (%)	
	Data	MC	Data	MC
Station 1	99.2 ± 0.4	98.05 ± 0.03	98.9 ± 0.9	97.8 ± 0.1
Station 2	99.0 ± 0.4	98.98 ± 0.03	96.8 ± 0.9	95.5 ± 0.1
Station 3	99.1 ± 0.4	99.08 ± 0.04	96.8 ± 0.9	94.1 ± 0.1
Station 4	98.9 ± 0.6	99.00 ± 0.04	94.9 ± 1.6	91.7 ± 0.2

Table 16. To be selected to contribute to efficiency measurements in the muon endcap, a muon probe must satisfy the following criteria:

1	be reconstructed separately in both the inner tracker and the muon system
2	have $p_T > 6\,\text{GeV}/c$ and $15 < |p| < 100\,\text{GeV}/c$ (to minimize multiple scattering and mis-reconstruction)
3	be consistent with originating at the interaction point (to reject decays in-flight and mis-reconstruction)
4	have a minimum number (11) of hits in the tracker system (to ensure a good momentum measurement)
5	have at least one hit in the muon system even after the combined fit to the tracker and muon detector measurements in which hits may be dropped according to quality-of-fit requirements (to reject decays in-flight and mis-reconstruction)
6	have good quality fits to both tracker hits alone and to the combination of tracker and muon hits
7	have hits in at least 2 muon stations (to reject punch-through by pions, kaons, and jets)
8	be the only muon in the same hemisphere in z

The inner track of the selected muon candidate is propagated through the magnetic field and the detector materials to the muon chambers. This defines the probe used to measure the reconstruction efficiencies. If a reconstructed object (rechit or segment) is found near the track propagation point (within a cone of aperture $\Delta R = 0.01$ around the track) in a given station, the probe is considered efficient. For stations 1, 2, and 3 the chamber being probed should not be the endpoint of the reconstructed muon. For chambers in station 4, this requirement is dropped.

The CSC system has been designed to be efficient for high-p_T tracks originating from the interaction region, and hence for incidence angles corresponding to straight lines from the interaction region. Low-p_T tracks can have a variety of incidence angles, because of the effects of the magnetic field and multiple scattering. Thus by requiring higher p_T probe tracks, systematic uncertainties resulting from incidence angle variations can be reduced, but at the same time increasing statistical uncertainties.

To minimize edge effects, the point at which the probe track intersects a chamber is required to be at least 10 cm from inefficient regions (high voltage boundaries and geometrical edges). This requirement excludes from the measurements strips and wires close to these regions, but should result

in the highest intrinsic chamber efficiencies. Figure 26 shows the rechit and segment efficiencies in these "active" regions for the CSC endcap stations and chambers. The segment efficiency is naturally defined per chamber as segments are built from the information of all 6 chamber layers. The rechit efficiency is defined per single layer of a chamber. Assuming that no correlation exists between layers (this assumption depends on the mechanism by which rechits are lost; for example, an inactive HV region could affect a single layer whereas an inactive cathode readout board could affect all 6 CSC layers) the CSC chamber rechit efficiency is defined as

$$\bar{\varepsilon} = \frac{\sum_i \varepsilon_i}{L} = \frac{\sum_i n_i}{N \times L} \tag{7.3}$$

with an estimated uncertainty of

$$\Delta\bar{\varepsilon} = \sqrt{\frac{\bar{\varepsilon} \times (1 - \bar{\varepsilon})}{L \times N}}, \tag{7.4}$$

where $L = 6$ is the number of CSC layers, ε_i is the efficiency in layer i ($i = 1, \dots, 6$), n_i is the number of efficient probes for layer i, and N is the number of all probes traversing the chamber.

With this method, the reconstruction efficiency is $96.4 \pm 0.1\%$ (stat.) and $97.0 \pm 0.1\%$ (stat.) for rechits and segments, respectively, averaged over all endcap CSCs and restricted to their "active" regions away from edges and high-voltage supports. The active region requirement is estimated to result in a systematic uncertainty of up to 0.5% on each value. These values also average over chamber regions with non-operational electronic modules, but exclude chambers that were providing no rechits, and are in agreement with the tag-and-probe results.

7.3 Rechit efficiency based on segment propagation

7.3.1 DT and CSC

The hit reconstruction efficiency can also be measured by using reconstructed local segments. In the absence of major hardware failures (HV faults, gas or readout problems), which may cause serious malfunctioning or signal losses in single cells or groups of cells, the signal production in different layers of the same chamber can be considered as a set of statistically independent processes. However, to reduce possible biases, loose selection criteria were applied to the reconstructed segments to discard low-quality segments.

In a barrel DT ϕ (θ) chamber, reconstructed segments were required to have at least 5 (3) hits, located in at least 4 out of 8 (3 out of 4) chamber layers, and a local inclination angle of $\psi < 40°$. In the endcap CSCs, segments were required to be close ($\Delta R < 1$; defined in section 4.2) to a probe muon track as described in table 16, and have at least 4 out of 6 layers.

Using the set of hits associated with a reconstructed segment, the segment was fitted again, once per layer, ignoring the information for that layer. In this way the position of the segment in the layer under study is determined in an unbiased way. Two kinds of efficiencies were considered: the efficiency to find a reconstructed hit within a cell, and the efficiency to actually associate a hit to the segment. The latter efficiency is by definition lower, as it includes the effects of the calibration and fitting procedures.

Figure 27 (top) shows both hit reconstruction and hit association efficiency as functions of the position in a DT cell. Apart from the known inefficiency induced by the cathode "I-beams" (see figure 5, right) at the edges of the cell [5], the hit reconstruction efficiency is $\geq 99\%$ everywhere.
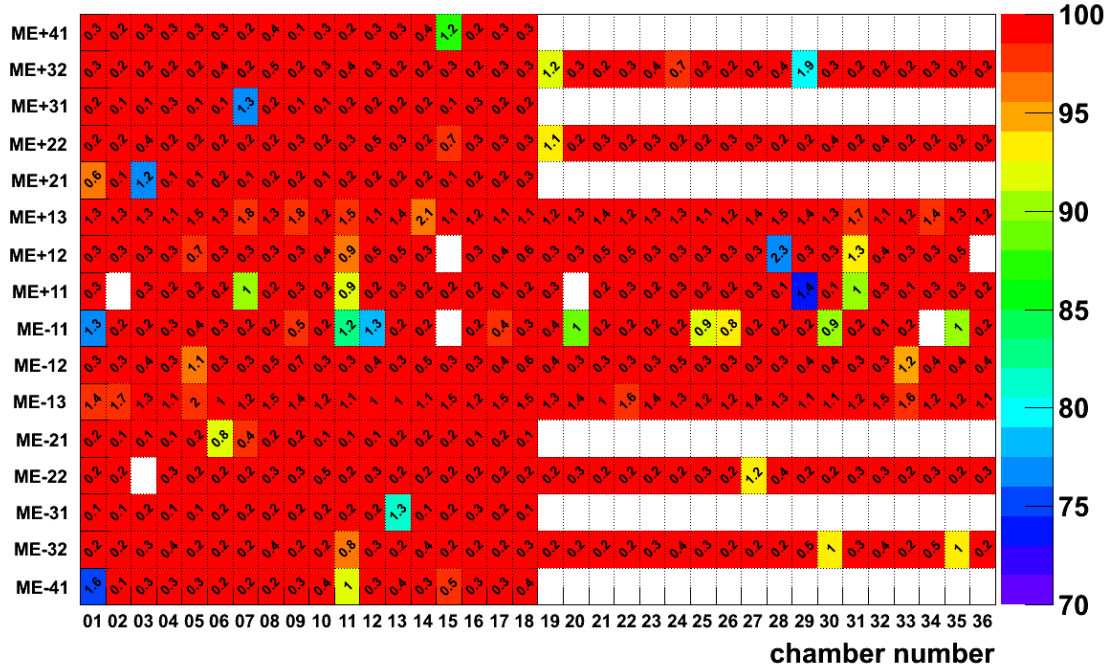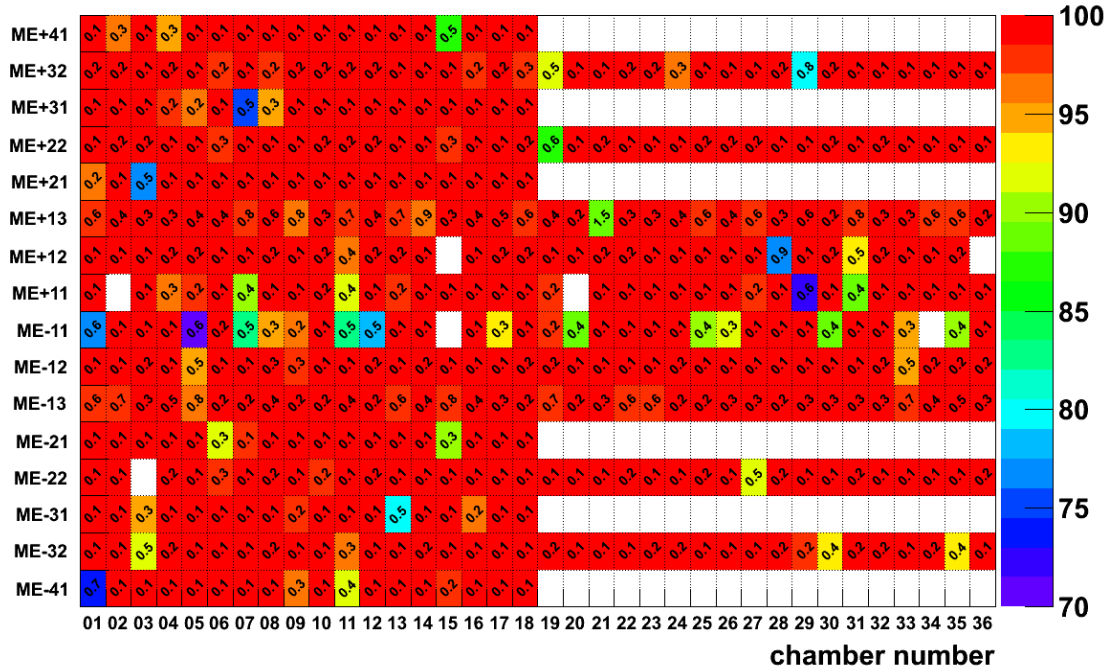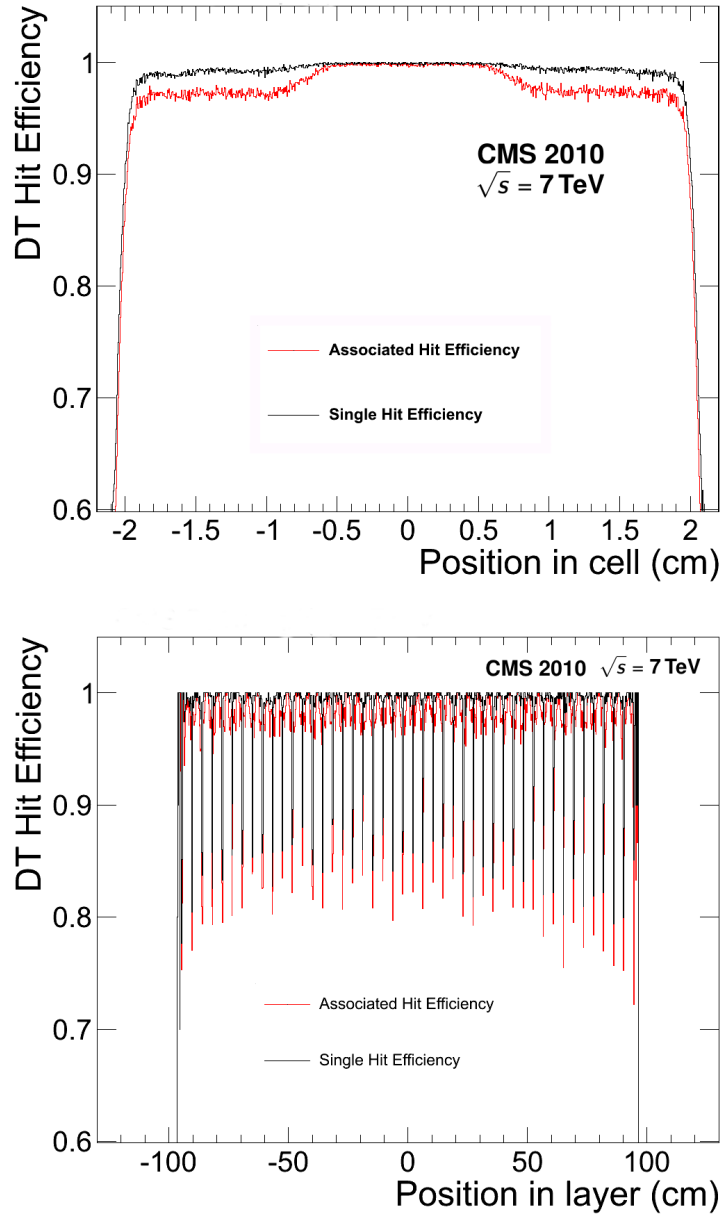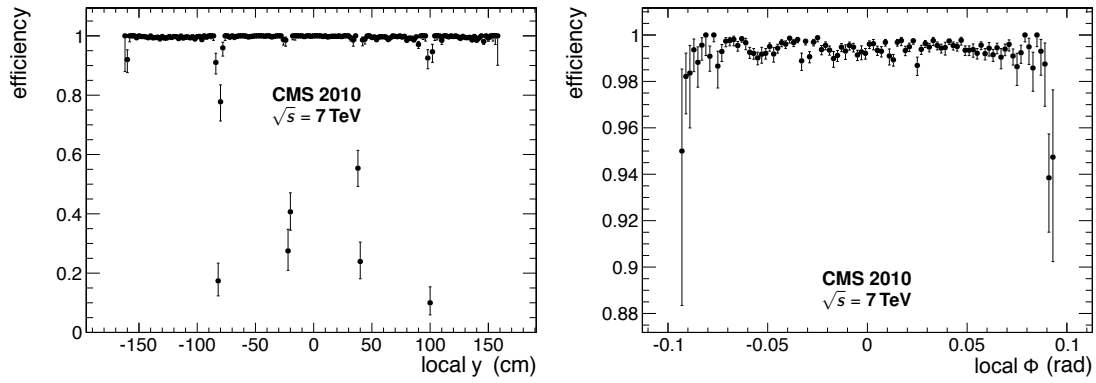
Figure 26. Reconstruction efficiency in "active" CSC regions (per chamber) for segments (top) and rechits (bottom). The number in each cell is the estimated statistical uncertainty. Note that there are only 18 chambers for types ME2/1, ME3/1, and ME4/1 because each chamber subtends $20°$ in ϕ, while all the rest cover $10°$.

Figure 27. Top: hit reconstruction (black) and association (red) efficiencies as a function of the track position in a DT cell. Bottom: hit reconstruction (black) and association (red) efficiencies as a function of the track position in a DT MB1 layer.

The hit association efficiency is, as expected, up to 2% lower, because it depends on the details of the calibration and contributions from δ rays. Indeed, because of the electronics dead time, δ rays may cause an early hit that masks the actual hit from a muon. In fact, the hit association efficiency matches the reconstruction efficiency in the central region of the cell, where this δ-ray effect is smaller. Figure 27 (bottom) shows the hit reconstruction and the hit association efficiencies as functions of the position in the layer for a subset of DT MB1 chambers. The efficiency is

Figure 28. CSC rechit reconstruction efficiency dependence on the local *y* coordinate (left) and on the local *φ* coordinate (right). Local *y* is measured by the anode wires, and local *φ* by the cathode strips.

approximately constant along the layer and the cell structure is clearly visible. Overall, the hit reconstruction efficiency in the barrel DT system is on average ≈98%, whereas the association efficiency is ≈96%.

Figure 28 shows the rechit efficiency in the endcap CSCs of station 2, ring 2, for all layers as a function of the local *y* coordinate (left) and the strip *φ* angle (right). Inefficient chamber regions located between the high voltage supports are clearly visible on the left plot. A slight inefficiency is observed at the boundaries between consecutive cathode readout boards (CFEB) in the *φ* efficiency plot (right). The rechit efficiency in the "active" CSC regions is well above 99.5%.

The association efficiency is not of critical concern in the CSCs due to the redundancy of 6 detection layers per chamber, but was measured to be between $(98.2 \pm 0.2)\%$ and $(98.7 \pm 0.2)\%$ for muons originating from cosmic rays [10] and with no layer dependence. The association inefficiency reflects the specific way δ rays influence the chamber readout and the subsequent reconstruction algorithm, and do not need to be the same for DT and CSC chambers.

7.3.2 RPC

The barrel and endcap RPC systems are mainly used as trigger detectors; however they also contribute to the muon reconstruction by providing additional position and time information in the barrel and endcap regions. Every RPC is located close to a DT or CSC and therefore the extrapolation of a segment reconstructed by the latter should point to a specific RPC strip and to a particular location within the strip. In a sense, an RPC can be considered as an additional DT or CSC layer. This allows the use of reconstructed DT and CSC segments as probes for determining the RPC efficiency and, more generally, for studying the hit cluster size, surveying the chamber geometry, performing electronics connectivity tests, and addressing system alignment issues.

Figure 29 summarizes the approach/technique. To validate this method, several MC simulations were performed, setting the RPC efficiency to different values and then measuring it with simulated data.

The RPC hit reconstruction efficiency is defined as the probability of finding an RPC reconstructed hit when a muon passes through the RPC under study. The efficiency is computed as the
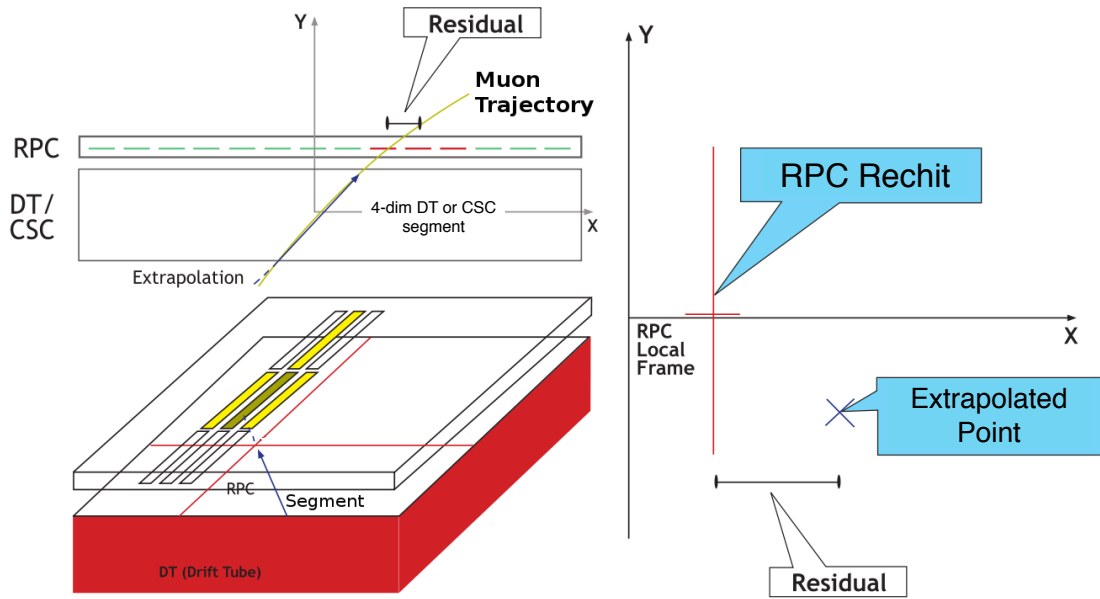
Figure 29. Sketch of the segment extrapolation technique.

ratio between the number of observed rechits and the expected number of hits, as estimated from segment extrapolation. A match between the extrapolated DT or CSC segment and the RPC rechit is identified when the distance between the border of the RPC cluster that contains the rechit and the extrapolated point is less than 4 strips (see table 11). This parameter was tuned to minimize small effects from strip masking (needed for some noisy channels) inside clusters without introducing significant bias from noise. To avoid edge effects, only probes that are more than 8 cm away from the chamber edges are considered.

The efficiency and its uncertainty are defined by eqs. (7.1) and (7.2), but the probes here are the DT and CSC segments and the passing probes are segments matched to RPC hits.

The measured efficiency is shown in figure 30, separately for the barrel (left) and endcap (right) RPCs. As can be seen, the efficiencies in the barrel and endcap chambers are comparable and around 95%, which satisfy the TDR requirements. The tail of lower efficiency chambers is a result of RPCs affected by electronics problems (e.g., a few dead channels) or not operating at the optimal voltage. Chambers that operated in single gap mode (6 in the barrel and 13 in the endcap) are excluded from the plot. The percentages of RPCs with efficiencies below 80% in the barrel and endcap are 1.2% and 1.3%, respectively. For the 2011 data-taking period, a set of calibration runs has been taken to tune the operating voltage chamber by chamber. In addition, a dedicated RPC monitoring stream was set up to detect any sign of aging effects, and to react quickly in case of problems by tuning the operating voltage accordingly.

Figures 31 and 32 show the hit reconstruction efficiency for individual RPCs in Wheel 0 of the barrel and in the 2 forward/backward endcaps, respectively. The plot color code shows the percentage efficiencies in 5% intervals. The errors, around 1%, are not shown in the plots. With
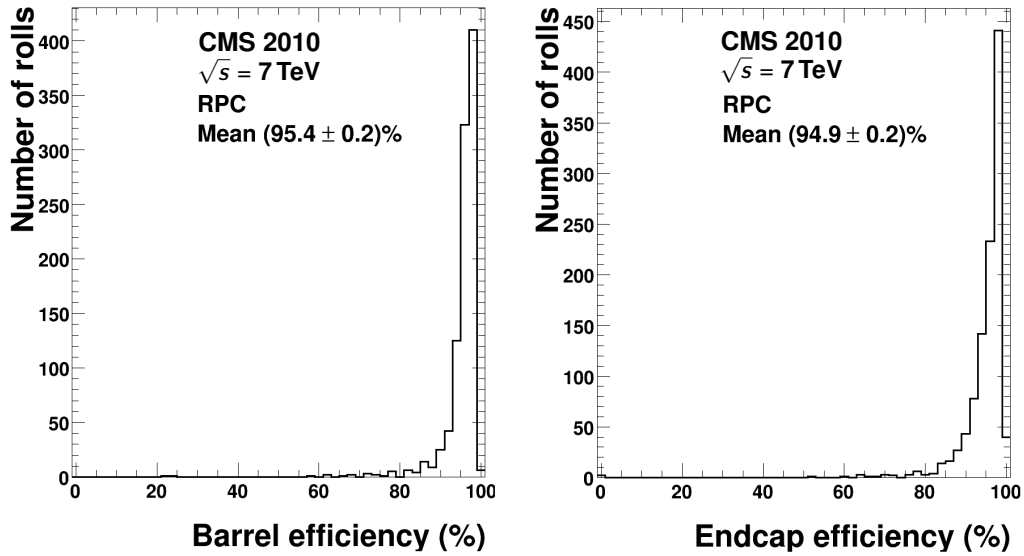
Figure 30. RPC efficiency distributions per chamber roll (see section 2.2) for the barrel (left) and endcap (right). The percentages of RPCs with efficiencies below 80% are 1.2% and 1.3% in the barrel and endcap, respectively. Chambers operated in single gap mode are excluded from the plot.

the exception of a few non-operating and unstable (low efficiency) chambers, the system has been performing according to expectations. Finally, figure 33 shows a high-resolution efficiency map for all the RB3 backward chambers in the barrel.

8 Radiation background in the muon system

Background radiation levels in the CMS muon system are an important consideration in its overall performance. Low-momentum primary and secondary muons, punch-through hadrons, and low-energy γ-rays and neutrons, together with LHC beam-induced backgrounds (primary and secondary particles produced in the interaction of the beams with collimators, residual gas, and beam pipe components) could affect the trigger performance and pattern recognition of muon tracks. In addition, excessive radiation levels can cause premature aging of the detectors. The 2010 proton-proton LHC running provides a good opportunity to measure the radiation backgrounds and compare them with simulation results, which strongly influenced the original system design [3, 26, 44].

The simulated radiation background levels inside and around the CMS detector during $\sqrt{s} =$ 7 TeV proton-proton collision running in 2010 (figure 34) confirm the main conclusions of previous simulation work and also demonstrate some asymmetry in the background rates around CMS owing to the presence of the CASTOR very forward calorimeter on the minus side of the detector ($z < 0$) at around $z = -15$ m.

8.1 Background measurement techniques

Each of the muon subsystems employs a different technology and different materials, thus each responds differently to the various backgrounds. On the one hand, for example, the CSC system
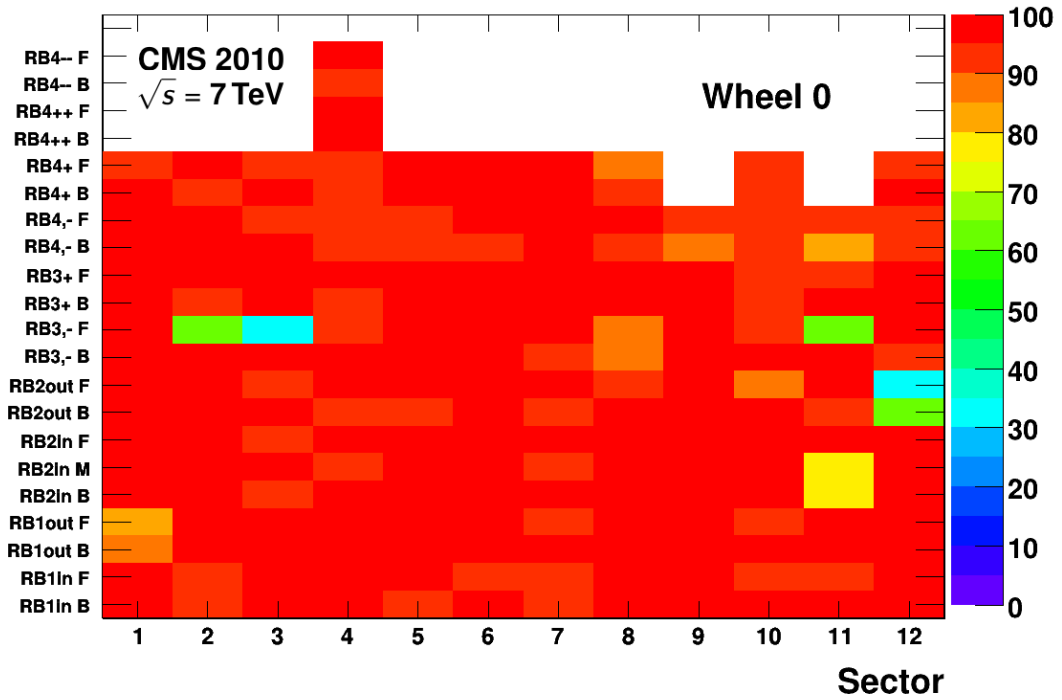
Figure 31. Percentage efficiency of Wheel 0 of the barrel RPC system. Chambers are grouped in sectors and stations; the *x* axis represents the sectors of the wheel and the *y* axis shows the chamber trigger sectors [2] for all layers. The plot has an odd shape because of the complexity of the RPC geometry: station 4 of sector 4 is composed of 4 different chambers, while station 4 of sectors 9 and 11 are composed of a single chamber instead of 2.

has 6 planes per chamber and typically requires 4 out of 6 planes to generate a track segment. Hence CSCs are relatively immune to neutrons, which generally affect only a single plane. On the other hand, the CSCs cannot distinguish punch-through background particles from genuine muon tracks. The RPC system provides a single hit per chamber from 2 gaps, and thus triggers on neutron hits. However, the RPC system has a very tight timing window of about 25 ns and is relatively unaffected by out-of-time signals. The DT system has 12 planes per chamber and is mostly immune to neutron hits. The timing window for the DTs, however, is large, and a high background rate could make track reconstruction difficult, and the event size could become too large for the readout.

As a result of these different technologies, each subsystem measures background rates in a different manner. The CSC system measures the trigger rate per chamber. To increase the sensitivity to backgrounds such as neutrons, the CSC trigger was run in a special configuration that requires only a single layer coincidence of wire and strip hits within a time window of 75 ns (instead of the nominal coincidence of 4 hits out of 6 layers). A coincidence of 2 or more hits from different layers that satisfy the single track criteria (a stub of hits pointing to the interaction point) is considered in this configuration as a single trigger event. Since this configuration is different from normal operation, these measurements of radiation load were taken during LHC fills after collisions had been established, but before CMS started taking physics data.
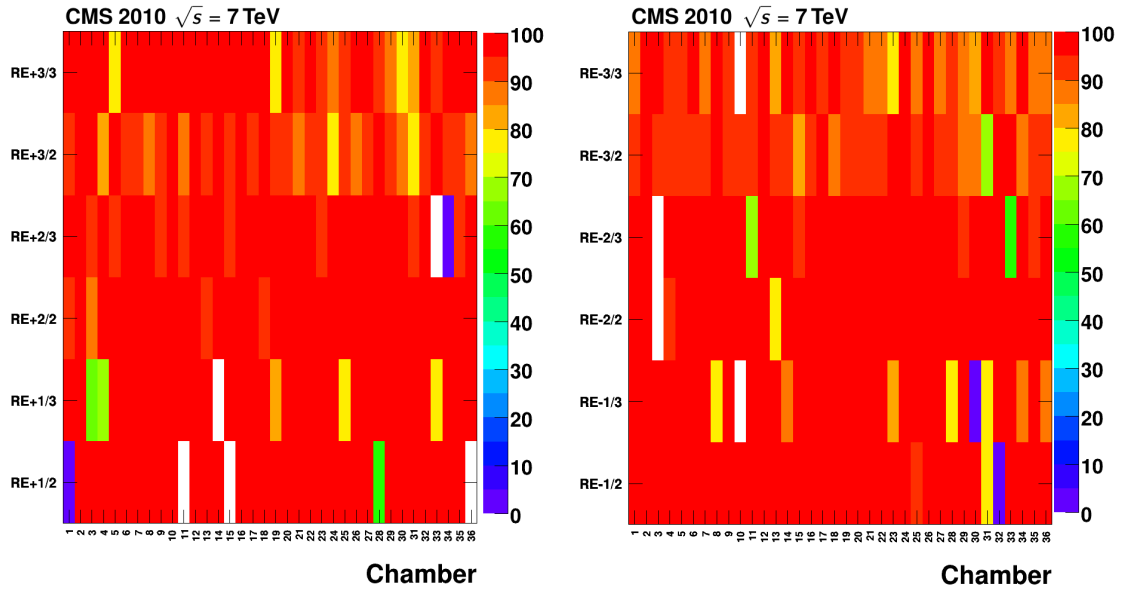
Figure 32. Percentage efficiency of the endcap RPCs. Chambers are grouped in stations (disks) and rings; chamber numbers are represented on the x axis and rings on the y axis, for the minus ($z < 0$) (left) and plus ($z > 0$) (right) endcaps.

The DTs selected a non-track background sample by requiring patterns with only 1 or 2 hits within a superlayer. By integrating over the full $1.25\,\mu$s readout window, the DTs measured rates of out-of-time backgrounds originating mainly from slow neutrons and punch-through activation, as well as contamination from hits that occurred during other bunch crossings (pileup). The time distribution of these hits within the full $1.25\,\mu$s integration window was checked to be flat, in contrast to that for signals generated by prompt muons from proton-proton collisions, which arrive roughly in a 300 to 700 ns time interval, corresponding to the drift time across an entire cell. (The lower limit of the prompt muon time window is due to time delays, which are accounted for in calibration; see section 3.1.1.) As a crosscheck, the DTs also took advantage of their long pipeline cycle ($1.25\,\mu$s) and measured the rate in a 250 ns time window where no signals are expected from in-time particles originating in the proton-proton collision that triggered the event. Consistent results were found.

The RPC average strip rate is calculated by using the incremental counts, performed at the level of the RPC DAQ board (link boards), normalized to the strip area. The noise level is estimated for each run and each chamber separately through a linear extrapolation to a value for an instantaneous luminosity of 0, which is then subtracted from the chamber rate. After this noise subtraction, the resulting RPC rate is divided by 2 to account for the 2 RPC gaps. Similarly, the corresponding CSC rate is divided by 6 to take into account the 6 CSC planes. The hit rate per DT channel is divided by the drift tube area. Results are therefore presented in units of $\mathrm{Hz\,layer^{-1}\,cm^{-2}}$ (or for RPCs, $\mathrm{Hz\,gap^{-1}\,cm^{-2}}$). These rates can be compared between detectors, and to MC simulation.

The no-collision background rates are not expected to be identical, as they depend on several factors such as intrinsic noise, signal threshold, natural radioactivity of the chamber constituent
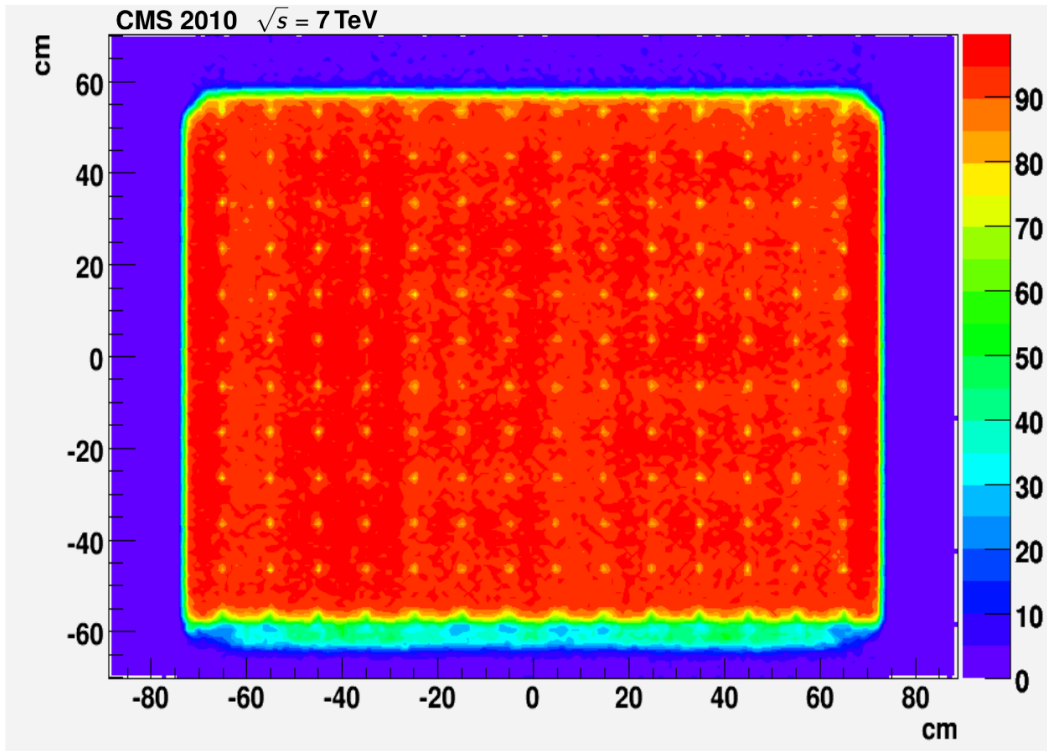
Figure 33. Local efficiency (in percent) during the 2010 LHC data-taking period for all RB3 backward barrel rolls. The low-efficiency points correspond to the location of the spacers in the gas gaps.

materials, and chamber location. The muon chambers were designed to detect minimum ionizing particles with nearly 100% efficiency, but they do not necessarily have identical efficiencies for detection of γ-rays and low energy neutrons, which are the main sources of background. The detector response to the background depends on the type and thickness of the constituent materials and on the gas mixture, and is a function of the energy of the detected particles. The DT no-collision background is about $0.0045\,\mathrm{Hz\,layer^{-1}\,cm^{-2}}$. The no-collision background levels seen by the CSCs are about $0.012\,\mathrm{Hz\,layer^{-1}\,cm^{-2}}$ for the chambers located inside the CMS steel and $0.015\,\mathrm{Hz\,layer^{-1}\,cm^{-2}}$ for the chambers located on the outer muon stations. The average RPC noise rate during the 2010 data-taking period is of the order of $0.05\,\mathrm{Hz\,gap^{-1}\,cm^{-2}}$, in good agreement with earlier measurements [11].

8.2 Background measurement results

Backgrounds for the CMS detector are expected to be high along the beam pipe and at high $|\eta|$. They are also expected to decrease with distance away from the beam pipe. In addition, backgrounds should be somewhat higher on the outside of CMS because the large amount of steel in CMS provides good shielding for chambers in the interior, a result that is supported by the background data presented in the next 3 subsections. For each case (i.e., dependence on z, r, and ϕ) we measure the background rates as a function of the luminosity, and later we use these data to extrapolate to the luminosities expected during future running of the LHC.
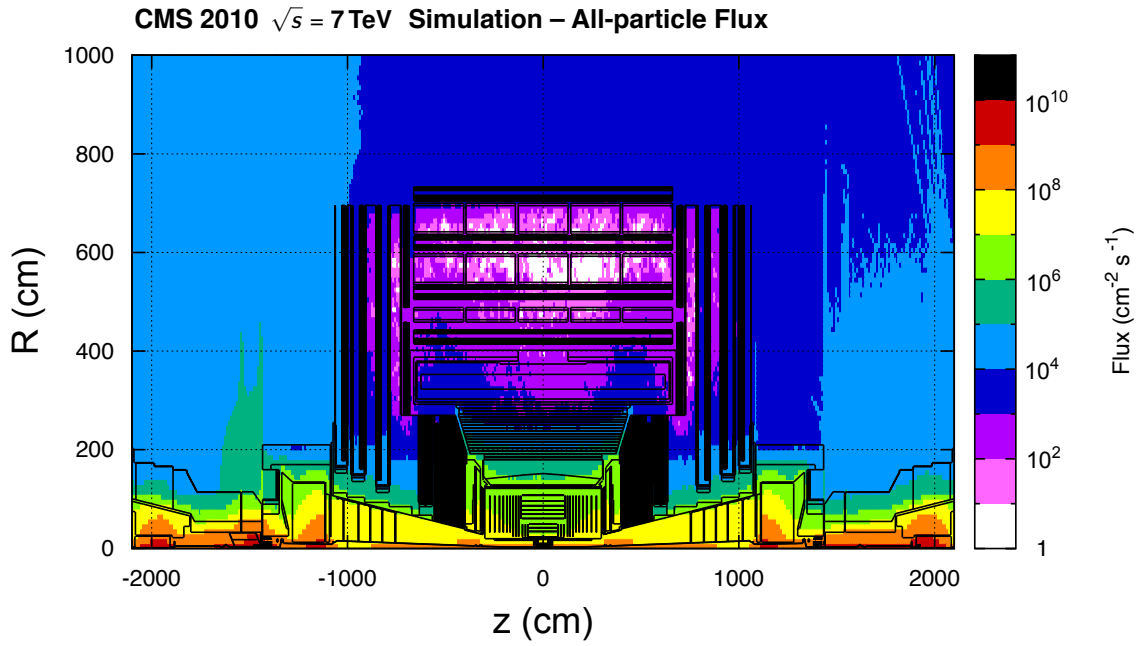
Figure 34. Simulated radiation background in the CMS cavern. CASTOR is located close to the beam pipe on the minus side ($z < 0$) in the very forward region at around $z = -15$ m.

The CSC rates are averaged over a ring area and the DT rates are averaged over all chambers in a wheel or station. The RPC rates, however, are the maximum observed rates over either the barrel wheels or stations, or the endcap disks or rings. Because of this and other differences in materials and thresholds, the RPCs typically report larger rates than the DTs or the CSCs.

8.2.1 Backgrounds as a function of azimuth and plus-minus asymmetry

To first order, CMS is a nearly symmetric detector in both azimuth and z, so no azimuthal dependence nor $+z/-z$ asymmetries in background are expected. Figure 35 shows the DT and RPC rates for the inner and outer stations of the barrel Wheel-2 and Wheel$+2$ (YB-1 and YB$+2$, respectively) as functions of azimuthal angle. As can be seen in the figure, the rates in the inner rings are symmetrical, but those in the outer chambers have a strong azimuthal dependence. For both subsystems, we observe a difference in rate of approximately a factor 20 between the top ($\phi = 1.6$ rad) and the bottom ($\phi = 5.2$ rad). This top-bottom asymmetry is due to non-symmetric features of CMS: the supports for the wheels and disks, and the steel flooring.

The outer DT chambers of the YB-2 wheel observe $\approx$20% higher background relative to the chambers located on the YB$+2$ wheel, while the RPCs do not see any $+z/-z$ asymmetry. The barrel RPC rates are about 2.5 times higher than the DT rates, but we note that, in addition to the different materials and technologies, the DT rates exclude prompt tracks whereas the RPCs do not. The endcap inner rings (figure 36) do not see any $+z/-z$ asymmetry, except for the ME2/1 rings, which display an asymmetry at a level of approximately 50% that is not yet understood. The outer muon chambers observe a noticeable asymmetry between the plus and minus sides of CMS. The CSCs in the minus endcap observe an approximately 20% larger rate relative to the plus side for
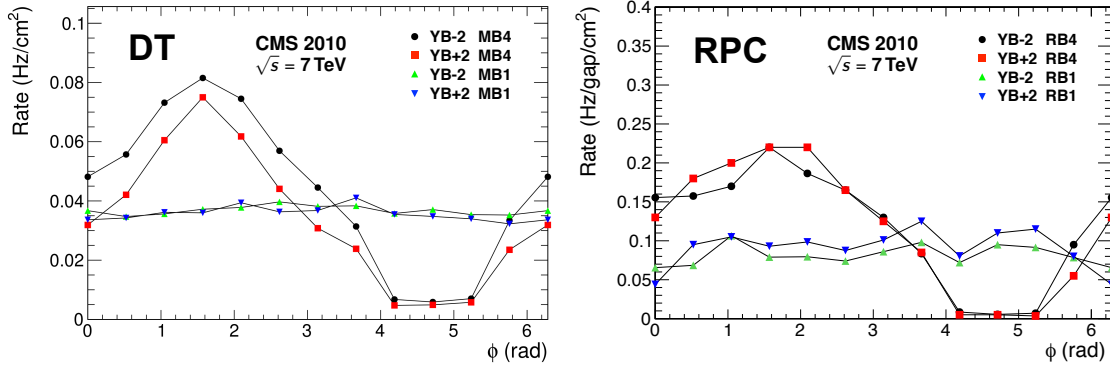
Figure 35. The background rates of DTs (left) and RPCs (right) located on the inner and outer stations of the external wheels as a function of the chamber azimuthal position at an instantaneous luminosity of $1.5 \times 10^{32}\,\mathrm{cm}^{-2}\,\mathrm{s}^{-1}$.

the ME3/2 rings, ≈30% for the ME2/2 rings, and ≈10% for the ME1/3 and ME4/1 rings. This kind of asymmetry, which is also observed by the outer station barrel DTs (≈20%), is qualitatively reproduced in FLUKA simulations (see figure 34) and is related to the presence of the CASTOR detector on the minus side of the CMS detector.

In the endcap region, a complete picture of the rates seen by the CSCs at an LHC luminosity of $1.9 \times 10^{32}\,\mathrm{cm}^{-2}\,\mathrm{s}^{-1}$ is shown in figure 36 as a function of the chamber angular position. The chambers of the inner endcap rings in all stations show no angular dependence, while some is apparent in the outer ring chambers. The ME2/2 and ME3/2 rings show a small angular dependence. The most prominent effect appears in the ME1/3 chambers, which are closest to the outer barrel stations in both endcaps. The plot shows a clear decrease in the rates of the bottom ME1/3 chambers, for $\phi \simeq 270°$, near the floor of the cavern. The azimuthal asymmetry in the endcaps is much smaller relative to that seen in the barrel. This is because the endcap chambers are located between steel disks, while the barrel outer chambers are unprotected from the surrounding background.

Adjacent chambers in many rings of both the minus and plus endcaps have different rates (figure 36). Adjacent chambers in a ring overlap to avoid inefficient regions between neighboring chambers. Thus there are both "back" chambers, which are mounted first on the steel disks, and "front" chambers, which are mounted on the top of the installed back chambers. The alternating effect in background rates appears in most rings, but not in the ME3/1 and ME1/3 rings, the latter which has only a single layer of chambers. The difference in the rates between the back and front chambers is typically a few percent for most of the rings, but reaches 10% for the ME1/2 ring and 20% for the ME1/1 chambers. Background rates oscillate between front and back chambers, with higher rates in the chambers located further away from the IP. This effect is due to the steeply rising background at high $|\eta|$. Chambers farther from the IP also span a slightly higher $|\eta|$ region and thus have higher background rates.

8.2.2 Backgrounds as a function of z

The average trigger rates for the inner rings of the endcaps, where MC simulations predict the highest rates, are shown as a function of the LHC luminosity in figure 37 (left). As expected, the
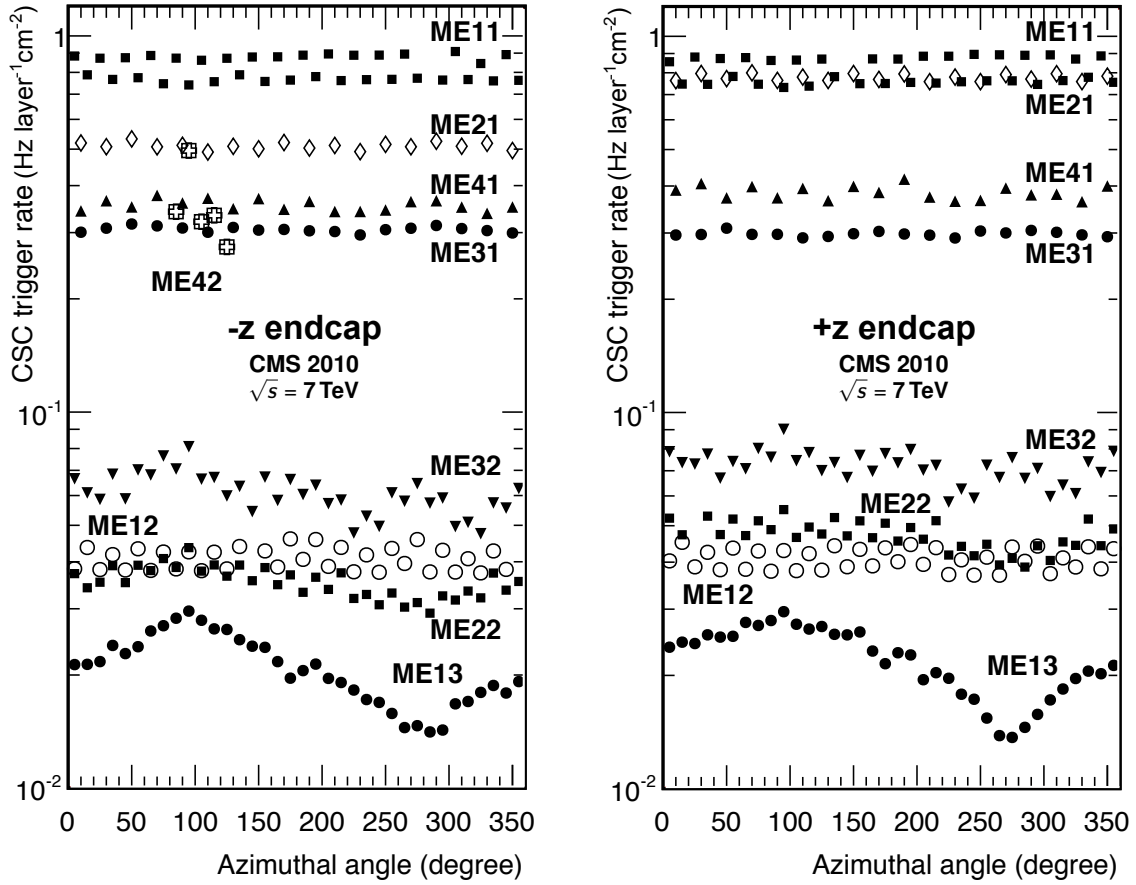
Figure 36. The CSC rate at the luminosity 1.9×10^{32} cm $^{-2}$ s $^{-1}$ as a function of the chamber angular position for the minus ($z < 0$) and plus ($z > 0$) endcaps.

CSC rates increase roughly linearly with the luminosity of the LHC. The largest rates are observed for the ME1/1 ring where, at the luminosity 1.9×10^{32} cm $^{-2}$ s $^{-1}$, the counting rate was up to 60 times the no-collision background rate. The background level drops with increasing distance from the IP and only at the outer station (ME4/1) does it slightly increase.

The maximum rates for the RE stations are also shown versus the LHC luminosity in figure 37 (right). The patterns are different because the RPC inner ring 1 has not yet been installed: the inner rings of the CSCs show a mostly decreasing background as *z* increases, whereas the endcap RPC data show the rates increasing with increasing *z*, with the highest rate measured in the third (external) disk, in agreement with the outer CSC rings. This reflects the different types of backgrounds near the beamline and on the outside of CMS. The increase in background for ME4/1 is consistent with this picture.

In the central η region, the behavior of the background is slightly different. The average DT rates versus luminosity are presented for the barrel wheels (YB0 is closest to the IP and YB$\pm$2 are farthest away) in figure 38 (left). The right plot shows the corresponding maximum RB rates. The patterns are roughly the same: rates increase as the chambers are farther from the IP.
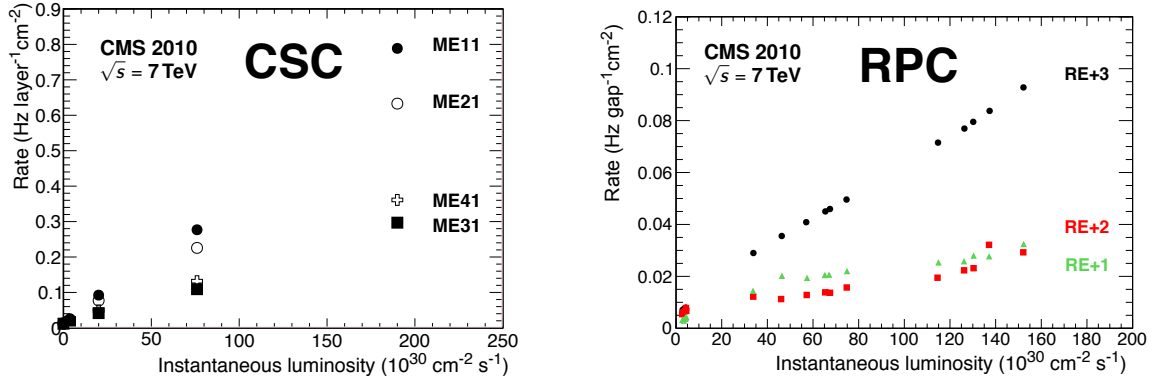
Figure 37. Left: the background rates for the CSC inner rings *vs.* luminosity (ME1/1 is closest to the IP; ME4/1 is farthest away). Right: the RPC background rate *vs.* the luminosity for the outer rings of RE (RE1 is closest to the IP; RE3 is farthest away). The differing ordering patterns between the CSC and endcap RPC rings reflect the different backgrounds near the beamline and on the outside of CMS.
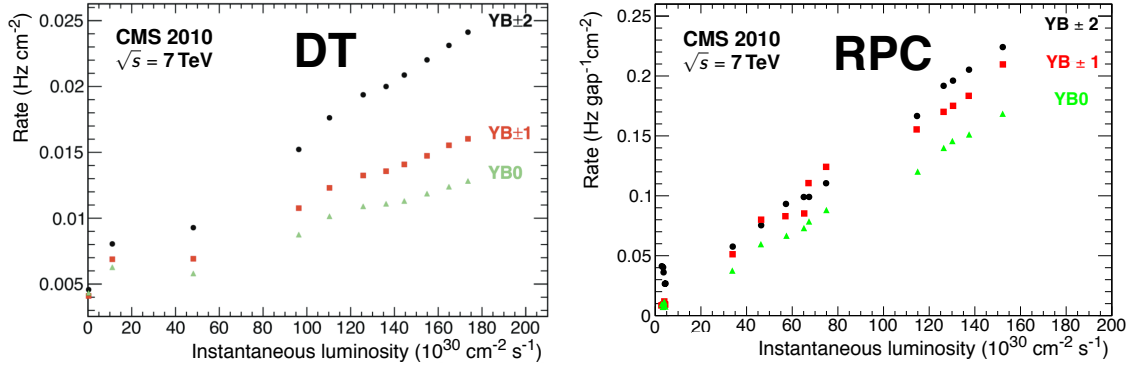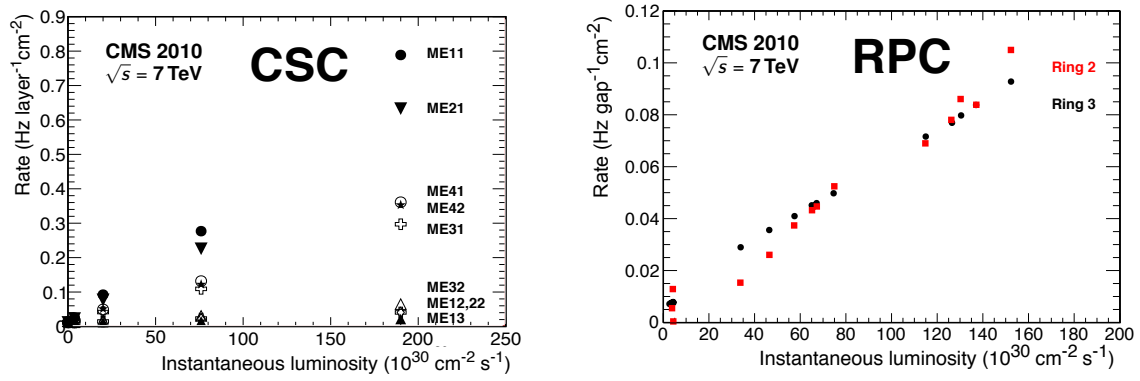

Figure 38. Left: the DT background rates *vs.* LHC luminosity for the barrel wheels (YB0 is closest to the IP, YB±2 are farthest away). Right: the RB backgrounds *vs.* luminosity for the barrel wheels. The patterns are similar, increasing as the distance from the IP increases. The difference in rates occurs, in part, because the RB rates are maximum rates whereas the DT rates are averages.

8.2.3 Backgrounds as a function of *r*

The background behavior as a function of *r* is somewhat different. The CSC inner ring rates are presented together with the rates of the outer CSC rings as a function of the luminosity in figure 39 (left). RPC rates were not integrated over ϕ, so for comparison, the right plot shows the RE3 rates for trigger sector 10 (corresponding to 10°azimuth at the top of CMS) in the 2 rings of station 3.

The outer CSC and RPC rings show a much smaller increase in rate with luminosity relative to the inner chambers. Only the ME4/2 chambers show an increase comparable to the inner ring chambers. This increase for ME4/2 is predicted by the simulations and is related to its position on the outside of the detector where the planned outermost shielding disk, called YE4, has not yet been installed [3, 26, 44]. In spite of their different materials and gas mixtures, the rates seen by the CSCs and RPCs at the same locations are in good agreement. For example, the average ME3/2 rate at a luminosity of 1.9×10^{32} cm^{-2} s^{-1} is about 0.07 Hz layer^{-1} cm^{-2} while the RE3/2 and RE3/3

Figure 39. Left: the average CSC background rates *vs.* luminosity for all the endcap rings. Right: the maximum RE rates *vs.* luminosity for the top trigger sector 10 in the 2 rings of station RE3.
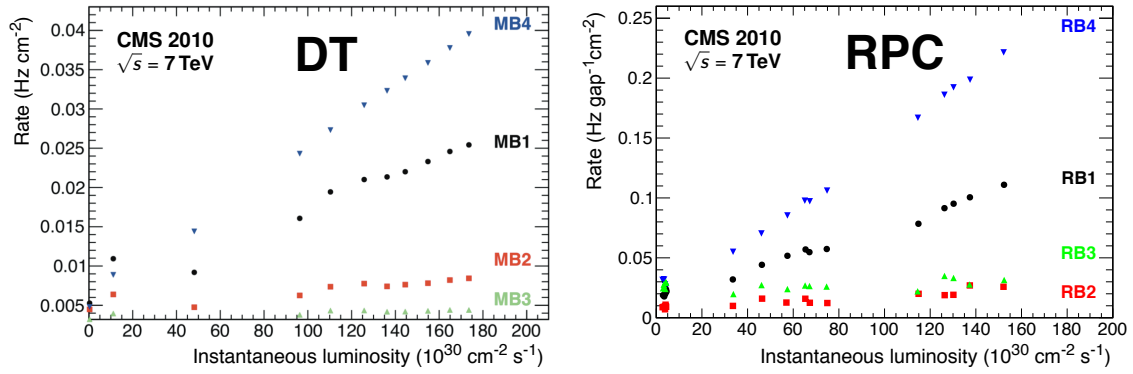
Figure 40. Left: the DT rates *vs.* luminosity for each of the 4 stations (MB1 is closest to the beam line and MB4 farthest away). Right: the RPC background rate *vs.* the LHC luminosity for the same 4 stations. Here the background rates are relatively low for RB2 and RB3. RB1 (closest to the beam line) has a higher rate, but RB4 (farthest from the beam line) has the highest rate because it is on the outside of the detector and measures the backgrounds outside CMS.

rates are at the level of $0.1\,\mathrm{Hz\,gap^{-1}\,cm^{-2}}$. It should be noted that the CSC rates are averaged over the entire ring, while the RE rates are the maximum rates observed in that ring.

For the central region ($|\eta| < 0.9$), the *r* dependence of the background is shown in figure 40, which presents the DT and the RPC measured rates in the barrel stations as functions of the LHC luminosity. The largest rates are observed by the DTs and RPCs for the last and first muon stations. The chambers of these stations are exposed to different sources of background. The inner chambers are sensitive to activation caused by leakage of particles from the hadron calorimeter, while the outer station chambers are mostly exposed to the slow neutron gas permeating the cavern. The DTs and RPCs located in stations 2 and 3 detect much smaller rates. They are well protected against the above mentioned backgrounds by the steel of the barrel wheels.
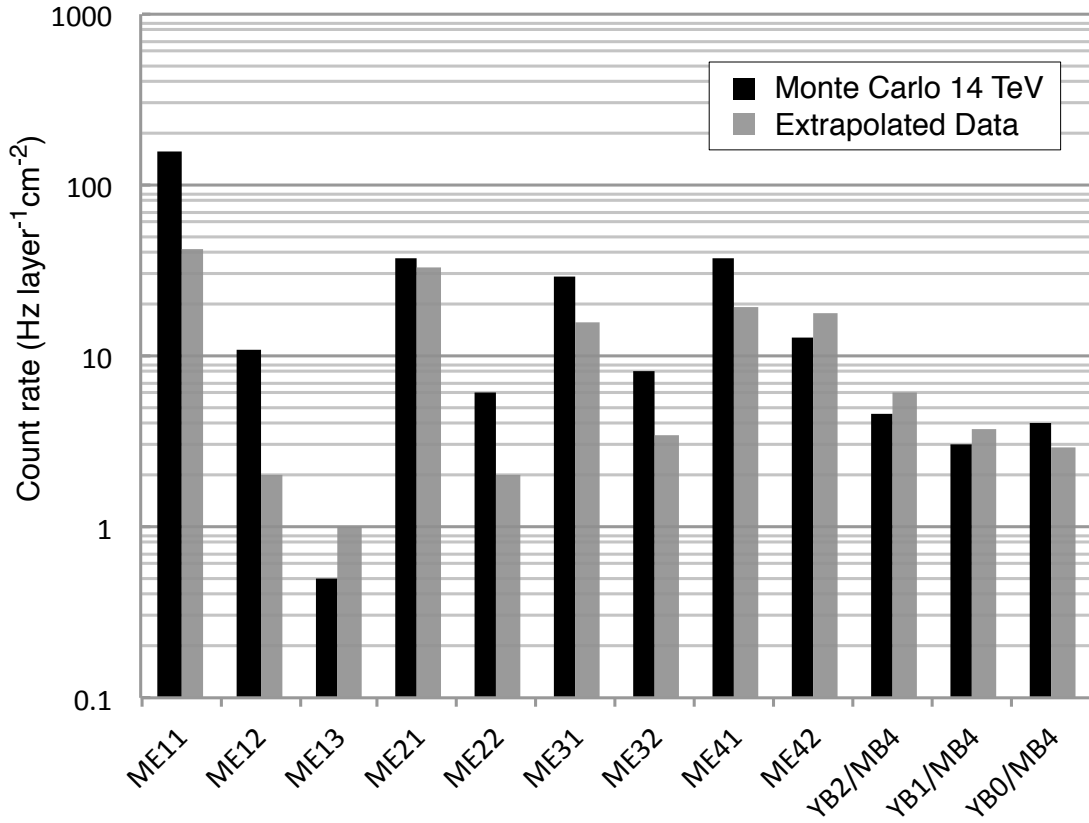
Figure 41. Radiation background rates in the CMS muon system projected for an LHC luminosity of $10^{34}\,cm^{-2}\,s^{-1}$. The data results are linearly extrapolated from 2010 measurements at LHC luminosities up to $1.8 \times 10^{32}\,cm^{-2}\,s^{-1}$.

8.3 Extrapolation to higher luminosity

Based on current measurements of the background levels, the rates seen in the muon system can be extrapolated to higher luminosities. The results of linear extrapolations to LHC peak instantaneous luminosity values of $10^{34}\,cm^{-2}\,s^{-1}$ are presented in figure 41 along with MC predictions [26].

For the barrel wheels, only the expected neutron background level is taken into consideration. For the endcap rings, all particle fluences are included. Note that the MC simulations were for an LHC beam energy of 7 TeV, whereas the data were accumulated at 3.5 TeV.

Figure 41 shows that the simulated levels are larger than the extrapolated measured rates in locations where the background levels are highest. Although the ME1/1 rate is higher than the others, it is notably less than the prediction. The extrapolated rates are slightly higher than the predicted levels of background only for the chambers of the outer stations because they are not shielded. It is expected that the addition of the YE4 shielding disk currently under construction will alleviate the high rates indicated for the ME4/1 and ME4/2 chambers.

9 Alignment

Precise measurement of muons up to the TeV/c momentum range requires the DTs and CSCs to be aligned with respect to each other, and to the central tracking system, with an accuracy of a few hundred microns, comparable to their intrinsic spatial resolution. The RPCs are already aligned to the limit of their spatial resolution, which is about 1 cm. The muon transverse momentum is measured from the curvature of tracks in the r-ϕ plane. The precision on displacements in the r-ϕ direction and rotations of chambers around their local axis parallel to z is therefore directly related to the momentum resolution. In both of these degrees of freedom, the alignment system is designed to achieve resolutions of 100–150 μm and 40 μrad for both the MB1 and ME1/1 chambers, which have the largest weight in the muon momentum measurement. Alignment in other degrees of freedom affects the momentum measurement as higher-order corrections. This section describes the muon alignment procedure and its performance.

To determine the positions and orientations of the muon chambers, the CMS alignment strategy combines precise survey and photogrammetry information, measurements from an optical based hardware alignment system, and the results of alignment procedures based on muon tracks.

The muon hardware alignment system consists of rigid structures in the barrel yoke, in the gaps between the different wheels, and between the barrel and endcap yokes, and of a set of straight line monitors running nearly radially along the surface of the endcap chambers of the forward disks. The 2 systems are connected to each other and to the central tracker by a link system. The link system consists of 2 floating rigid carbon fiber rings on the first 2 endcap iron disks close to the gaps that separate the barrel and endcap iron structures at $\eta = 0.9$–1.2. These rings are connected via a redundant network of laser lines and proximity sensors to rigid structures on the faces of the tracker and on the outer wheels of the barrel, and to plates that reference the positions of the chambers on the first endcap station. The link thus provides a relatively robust connection between the 3 detector systems. Further details about the track and hardware based alignment methods are given in refs. [13] and [14], respectively.

9.1 Muon barrel alignment

The DTs in the barrel are aligned independently by the hardware alignment system and by the use of muon tracks. The current CMS reconstruction uses the results of the hardware alignment, which is based on rigid, radial carbon fiber structures called modules for alignment of barrel (MAB) that are supported on the faces of the 5 wheels of the CMS steel yoke. A dedicated reconstruction program called the CMS object-oriented code for optical alignment (COCOA) [45] is used to transform the various optical measurements into DT chamber positions.

The hardware barrel alignment performs a complete alignment of all DTs in stations 1, 2, and 3 in a single computation. The fourth DT station is added in a second step to the resulting aligned structure from the previous calculation. The motivation for this factorization is two-fold: the computational problem becomes significantly simpler, allowing the reconstruction program to run much faster, and the knowledge of camera positions mounted on the MABs is less precisely known near the zone of the outer station, and therefore the internal barrel structure is essentially not affected by excluding station 4.

Table 17. The RMS of the differences in r-ϕ and z for all DTs in each wheel between photogrammetry and barrel alignment at B = 0 T after correcting for overall wheel movements.

Barrel Wheel	$\Delta r\phi$ RMS (μm)	Δz RMS (μm)
YB+2	476	826
YB+1	433	1260
YB0	707	989
YB−1	445	822
YB−2	625	847

Once all DTs and MABs are aligned relative to each other, the resulting barrel structure is treated as a floating rigid body, which must be positioned and oriented in space with respect to the inner tracker. The positions of the 12 external barrel MABs (6 on each end of the barrel) are reconstructed independently by the barrel alignment system (in an arbitrary reference frame) and by the link system. An initial tracker-barrel "cross-alignment" is therefore achieved by fitting the external MABs of the aligned, rigid barrel to the MAB positions determined by the link system. This cross-alignment is further refined by a track-based alignment method, which uses internally aligned tracker and muon barrel systems and obtains their relative position and orientation using only a few tens of thousands of global muon tracks from proton-proton collisions.

9.1.1 Validation

Alignment results must be validated before they can be used for track reconstruction and data reprocessing. The barrel alignment is validated by 3 independent cross-checks: comparison of photogrammetry measurements with alignment results obtained from measurements in the absence of magnetic field (0 T), residuals of standalone muon segments extrapolated to a neighboring station, and comparison with an independent track-based alignment of chambers.

An estimate of the accuracy of the barrel alignment can be obtained by comparing the results from geometry reconstruction at 0 T with photogrammetry measurements, in which all MABs and DTs in the same wheel are measured simultaneously. Care must be taken when comparing photogrammetry measurements, which are taken with an open detector, to alignment measurements after detector closing. Since wheels can move and tilt upon closing of neighboring structures, and since the same MABs are used to measure DTs sitting on different wheels, only the relative positions of DTs within each wheel can be expected to agree. For this reason, all comparisons are made independently for each wheel. Large disagreements between photogrammetry and alignment reveal an overall wheel movement between the 2 sets of measurements, as illustrated in figure 42 (top) for YB+2. After correcting for this movement, the phi sectors within each wheel can be compared, as shown in figure 42 (bottom). Table 17 shows the RMS differences between the results of photogrammetry and alignment at 0 T in r-ϕ and z for all DTs in each wheel, after correcting for collective wheel movements.

Another test of the barrel alignment makes use of standalone muon tracks that are reconstructed with chamber positions updated after alignment. Track segments inside a given DT are extrapolated into the DT of the next station in the same wheel and sector, and the residuals between the extrapolated segments and the actual track segments are studied. Figure 43 shows the distri-
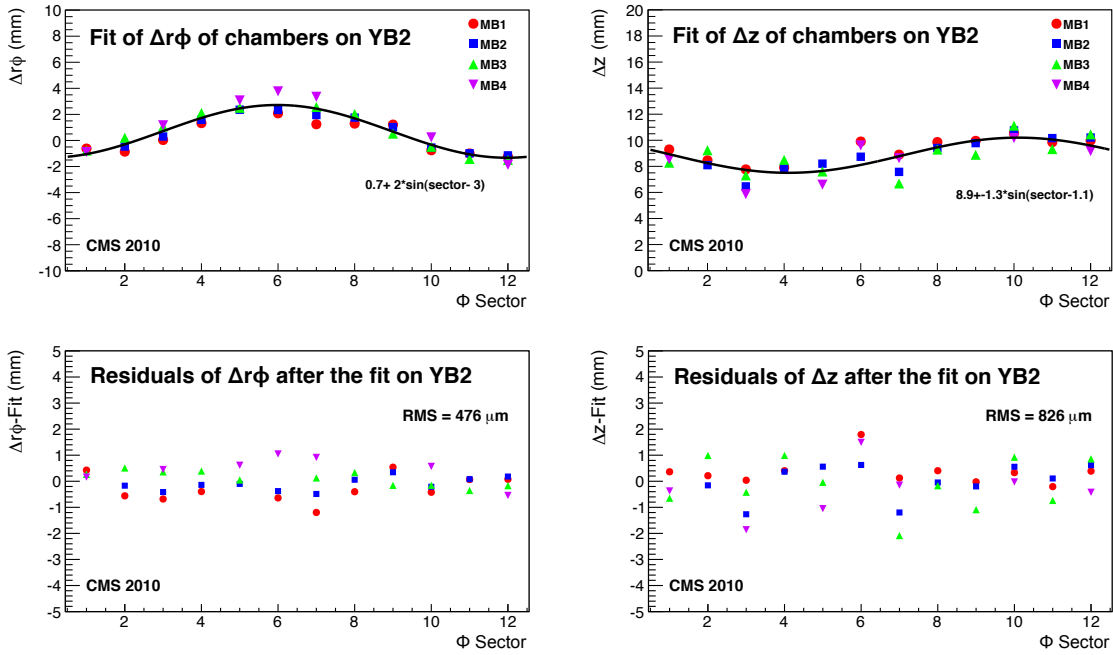
Figure 42. Differences in r-ϕ (left) and z (right) between photogrammetry measurements and barrel alignment at 0 T for DTs in YB+2 before (top) and after (bottom) correcting for the relative overall wheel movement.

butions of the residuals for all such DT pairs for the 4 coordinates measured by DTs before and after hardware alignment. In the absence of systematic effects, the mean values of these residuals are expected to be close to 0, while the RMSs of the distributions receive a contribution from the alignment precision (both for the overall chamber position and for the internal DT alignment) and from other tracking effects. The improvement of the distributions of the residuals after alignment is clearly visible.

Finally, the hardware and track-based alignment results are compared. Both alignments successfully reproduce the overall large corrections needed with respect to the design geometry, in which all chambers are placed at their design position. These corrections are mostly due to vertical and axial compression of the wheels due to the huge gravitational and magnetic forces acting on them. In MB1, both alignments agree in r-ϕ within $\approx 750\,\mu$m, consistent with the precision expected for the statistically limited track-based alignment. The agreement for stations 2, 3, and 4 worsens from 1 to 2 mm, as expected from multiple scattering effects and longer track propagation in the track-based alignment.

9.2 Muon endcap alignment

The muon endcap was aligned by using information from 4 different sources: photogrammetry, the muon endcap alignment system, tracks from beam halo muons, and tracks from muons produced in proton-proton collisions. Some of these sources supply measurements of the same alignment parameters, allowing cross-checks between the sources. The different alignment procedures sometimes apply to different subsets of the 3 spatial and 3 angular coordinates that specify each chamber
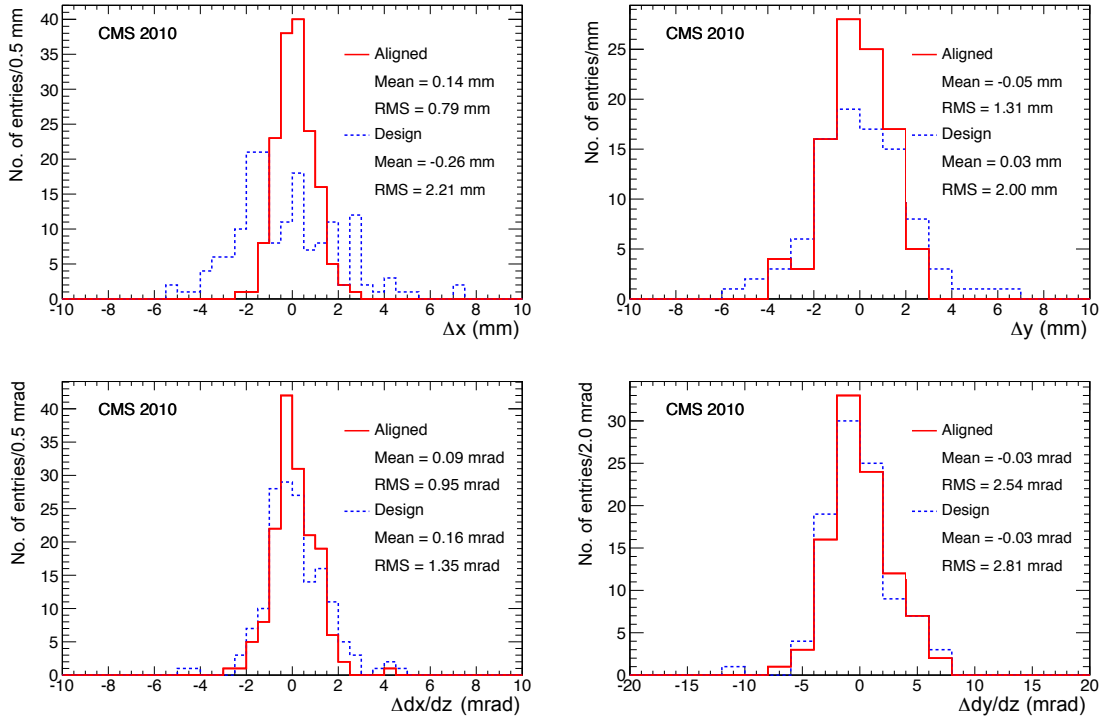
Figure 43. The difference before ("design"; blue, dashed lines) and after (red, solid lines) alignment between the measured and extrapolated standalone muon track segments going from one DT station to the next in the same wheel and sector for all such DT pairs in the 4 coordinates measured by DTs: local x, y, dx/dz, and dy/dz.

in the system. For example, alignment of entire disks (rings) of CSCs leads to an overall correction to the coordinates of each CSC in the disk. To combine the sources and procedures, the alignment corrections must be derived in a sequence of steps carefully chosen to ensure that as the alignment of a given coordinate is improved, the quality of alignment in other coordinates achieved in previous steps is maintained. For example, local z coordinates of chambers are taken initially from the hardware alignment system and are relatively insensitive to the track-based alignment procedure, but after improving the alignment in the orthogonal coordinates, some improvement in the z alignment can be obtained from the track-based procedure. Since the corrections from successive steps may be interdependent, the entire process is iterated until the results converge.

9.2.1 Measurement of disk bending with the muon endcap alignment system

The muon endcaps suffer a significant deformation when the solenoid is powered up to its operating field strength of 3.8 T. Some CSC chambers can move towards the center of the detector by as much as 14 mm, and they can rotate around their local x axis by as much as 3.5 mrad. The hardware endcap alignment system measures these movements by means of laser beams running nearly radially across each disk as described in detail in ref. [14].
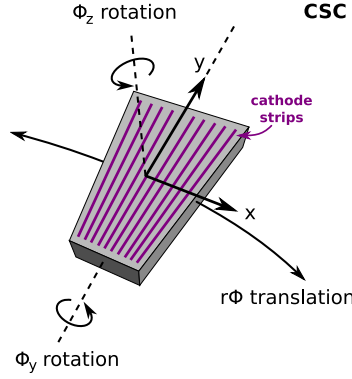
Figure 44. Schematic CSC chamber, indicating the local coordinate system.

9.2.2 Alignment of overlapping chambers using beam halo muons

The CSC chambers overlap slightly along their edges, and muons passing through these narrow regions provide information about the relative displacement of the neighboring chambers. To obtain individual chamber positions from the pairwise chamber information, the following objective function is minimized:

$$\chi^2 = \sum_{m_{ij}}^{\text{constraints}} \frac{(m_{ij} - A_i + A_j)^2}{\sigma_{ij}^2} + \lambda \left(\frac{1}{N_{\text{chambers}}} \sum_i^{\text{chambers}} A_i \right)^2, \tag{9.1}$$

where A_i are the chamber coordinates to optimize, $m_{ij} \pm \sigma_{ij}$ are the pairwise chamber measurements, and λ is a Lagrange multiplier to constrain the floating coordinate system. Two types of constraints are used: beam halo tracks and photogrammetry measurements, with the latter applied only to pairs of chambers that were missing track data on account of failed readout electronics (14 out of 396 pairs of neighboring chambers). The alignment proceeds in steps, first aligning r-ϕ positions (in which case the A_i are interpreted as positions and m_{ij} are residuals), then ϕ_z angles (in which case the A_i are chamber angles and m_{ij} are angle residuals), and repeating until the procedure converges. Definitions of the CSC local coordinates are illustrated in figure 44. The alignment fully converged after a single $r\phi$ pass and ϕ_z pass.

Although photogrammetry information was used to constrain some of the chambers, much larger weights were given to the beam halo data, in inverse proportion to the square of the measurement uncertainties in the 2 methods. The level of agreement between the track-based technique and photogrammetry is 0.3–0.6 mm (figure 45). This is much smaller than the typical scale of chamber corrections from the design geometry (2–3 mm).

9.2.3 Whole-ring placement using muons from proton-proton collisions

To complete the endcap alignment, the internally aligned rings must be aligned relative to one another and to the tracker. Tracks from the tracker were propagated to the muon chambers and whole-ring corrections were derived from the pattern of r-ϕ residuals as a function of global ϕ. A constant offset in the residuals is interpreted as a rotation of the ring in ϕ_z, while terms proportional to $\cos\phi$ and $\sin\phi$ are interpreted as displacements in global x and y, respectively.
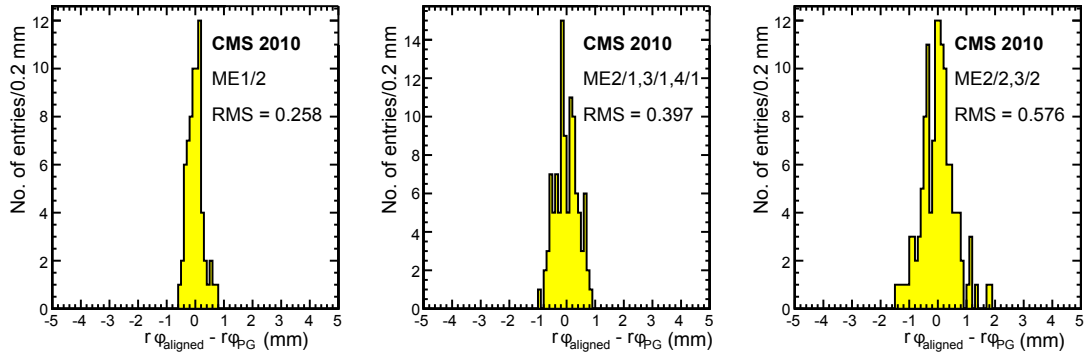
Figure 45. Chamber positions after internal-ring alignment compared with photogrammetry, split by ring. (ME1/1 chambers were not measured by the photogrammetry method.)
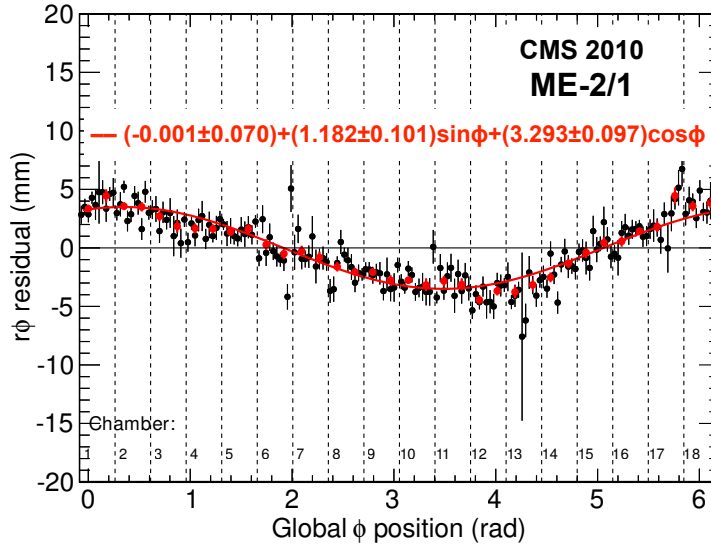
Figure 46. Residuals plot used to align a ring before alignment corrections are applied. Black points are a profile derived from truncated-Gaussian peak fits in each ϕ bin, and red points are the average of peak fits for μ^- and μ^+ separately. Three parameters of the fitted curve are interpreted as 3 alignment degrees of freedom. Vertical dashed lines indicate the boundaries between chambers.

Figure 46 provides an example of an alignment fit result for ring ME$-$2/1. The alignment was performed in a single pass, with a second iteration to verify self-consistency.

To cross-check the alignment with a qualitatively different method, beam halo tracks crossing an entire endcap (3 or 4 stations, depending on the distance from the beamline) were used to calculate residuals by extrapolating segments from one station to another. Figure 47 shows an example in which ME+3/1 segments were propagated linearly (no corrections for material or magnetic field) to ME+4/1. These plots were not used to perform the alignment, so the fact that the strong ϕ trend observed before alignment is eliminated in the aligned geometry adds confidence to the result.
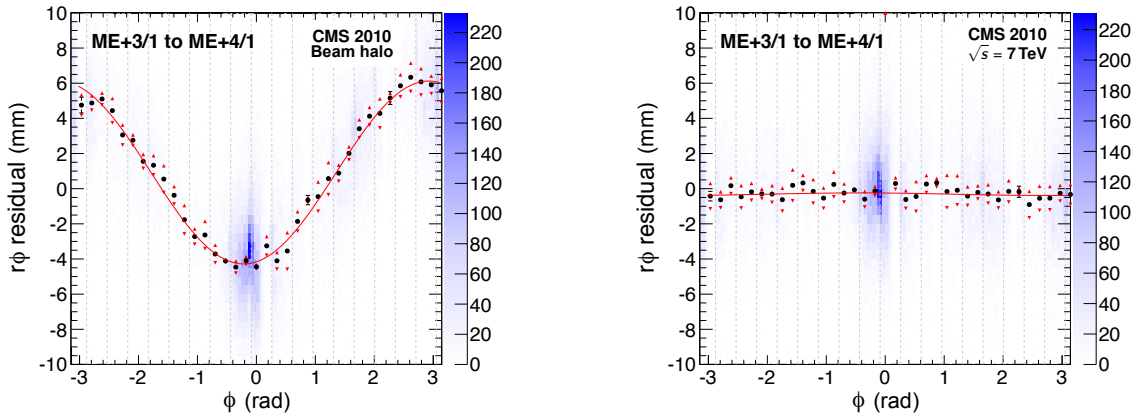
Figure 47. Residuals from beam halo tracks used to cross-check the alignment performed with collisions. The individual residuals are shown as the underlying blue scatterplot, in bins of 2.5° in ϕ and 0.5 mm in distance, with the density indicated by the right-hand scale. The symbols in these plots have the same meaning as in figure 46, though residuals were calculated differently (see text). Left: before alignment. Right: after alignment using collisions (not beam halo).

9.3 Alignment impact on physics performance

The most important test for any calibration or alignment is to study the effect it has on reconstructed quantities. In the case of muon alignment, higher-level objects related to muon tracks must be studied. Note that by design the momentum resolution is dominated by the central tracker for muons with transverse momentum below 200 GeV/c. A well-aligned muon system is therefore expected to induce minor beneficial changes at reconstruction level for low momentum global muons, and to improve global muon measurements for very energetic muons.

Figure 48 shows distributions of muon-related quantities for low momentum muon tracks from proton-proton collisions collected during 2010. The solid red and dotted black distributions correspond to the aligned and design (no alignment corrections) muon chamber geometries, respectively. From the top-left figure one can see that the alignment corrections lead to an improvement in normalized χ^2 for global tracks. The top-right plot shows the difference in track curvature (q/p_T) measured for the same muon when it is reconstructed as a global muon (including tracker information and therefore dominated by it) and as a standalone muon, which includes only muon chamber hits. This difference is indicative of the curvature resolution of the muon spectrometer (assuming the tracker resolution to be much better for low momentum muons). The bottom plots show an improvement in the dimuon mass resolution in the Z region. At least 1 standalone muon is required to see an improvement, since the invariant mass resolution for pairs of global muons at these energies is controlled by the tracker information.

To see the effect of the alignment on highly energetic muons, cosmic-ray muons must be used, because there were very few muon tracks above 200 GeV/c from proton-proton collisions in 2010. Cosmic muons collected in 2010 traversing CMS from top to bottom are split into a "top" and a "bottom" leg, and the momentum resolution is inferred from the difference in momentum measured for each leg separately. Figure 49 shows the q/p_T resolution as a function of muon p_T for

– 70 –
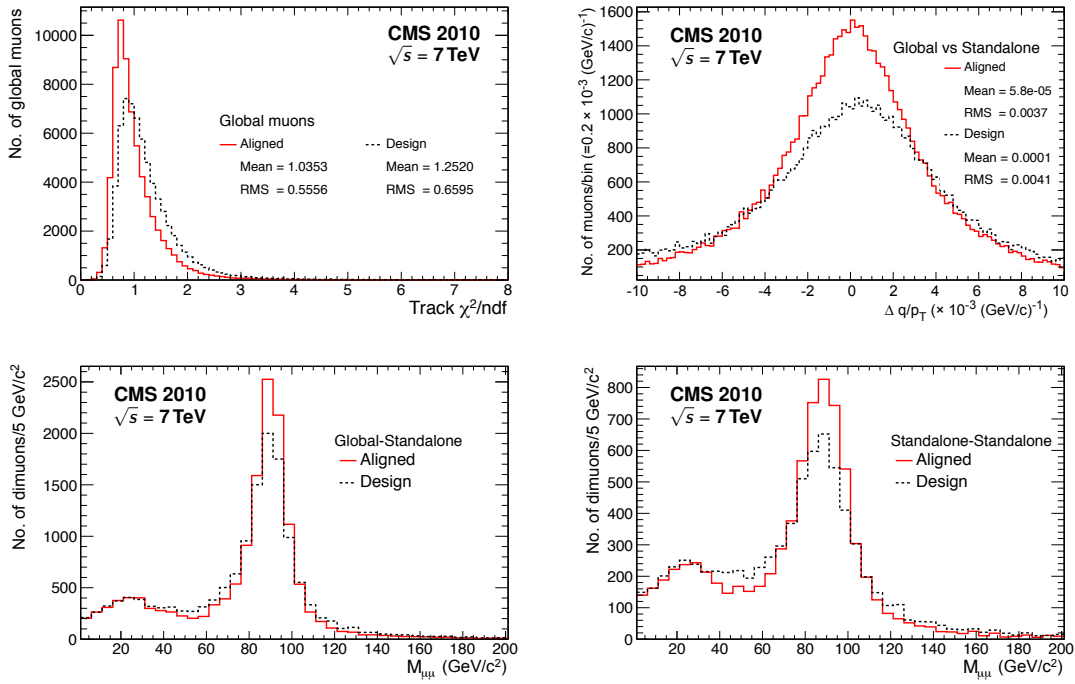
Figure 48. Muon track quantities reconstructed with design (black, dashed line) and aligned (red, solid line) muon chamber positions. Top-left: normalized χ^2 for global muon tracks. Top-right: difference in $q/p_{\rm T}$ between muons reconstructed as global and as standalone. Bottom: dimuon invariant mass for global-standalone muon pairs (left) and standalone-standalone muon pairs (right).

barrel muons reconstructed with the tracker plus the aligned muon geometry. For this figure, muons are reconstructed by a special algorithm that discards muon hits originating from electromagnetic showers induced by muon bremsstrahlung, as described in detail in ref. [15]. Muons reconstructed by using only the tracker are also shown for comparison. It can be seen that the aligned muon geometry improves the momentum measurement for values above 200 GeV/c, where muons reconstructed by using muon chamber hits have a better resolution than tracker-only muons.

10 Data quality monitoring

The primary goal of CMS data quality monitoring (DQM) [25] is to maximize the amount of high-quality data by identifying problems as early as possible. The DQM for the muon detectors focuses on monitoring the condition and efficiency of the detectors. Good efficiency is indicated by a uniform distribution of hits across the detectors (allowing for acceptance) and a low rate of readout errors. Additional monitoring plots are available to investigate issues more deeply.

The DQM checks are made online and offline. The online checks provide fast response to obvious problems — unpowered regions, problems with data acquisition, or improper calibrations — and a first evaluation of the suitability of the data. The offline checks use the information available from full event reconstruction with calibration and different trigger paths to provide a
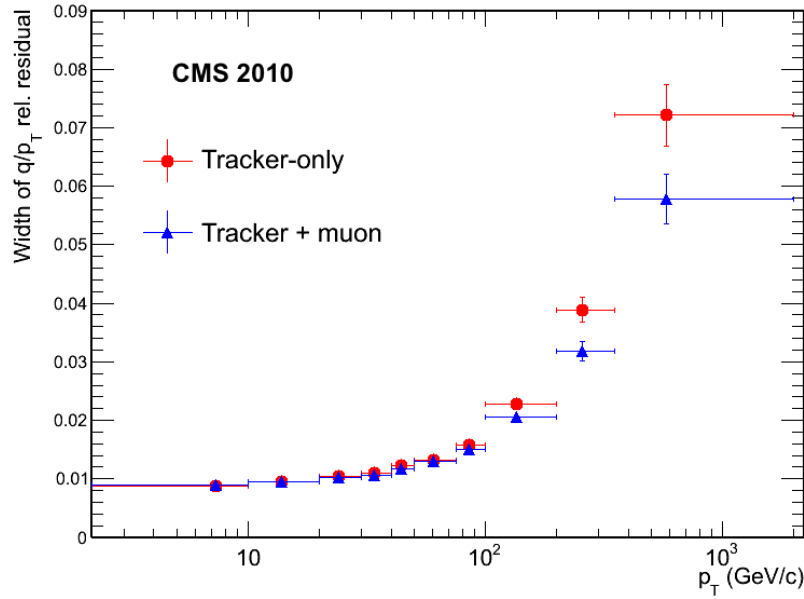
Figure 49. Widths of distributions of the difference between the q/p_T values for cosmic tracks reconstructed in the top and bottom parts of the apparatus. Both the central tracker-only and the central tracker plus aligned muon chamber cases are shown. The widths were obtained from Gaussian fits.

more detailed evaluation of the data. Offline DQM is used to certify the quality of reconstructed data and validate calibration results, software releases, and simulated data.

10.1 Online monitoring

In 2010, operation of the CMS detector moved from constant reliance on subdetector experts to become the responsibility of a central shift crew. Subdetector experts are on call for problems not readily solvable by the shift crew. With respect to the muon systems, the shift crew is responsible for raising the HV applied to the chambers after beam injection and lowering the HV when beams are dumped. Online monitoring of data quality is also part of the central shift crew duties. A special stream of events is used to perform DQM operations online [46]. The stream contains detector and trigger raw data, L1 and HLT summary results, in addition to HLT by-products essential for monitoring trigger algorithms. Events are delivered to data quality monitoring applications at about 10 Hz. Delivery speed depends strongly on the rate of event data processing. There is no event sorting or handling, and no guarantee that parallel applications receive the same events.

The raw data stream is checked for readout errors, the occupancy of detector channels, and the rates of muon trigger primitives. Catching readout errors is a vital and unique part of the online monitoring. For example, format errors in the data stream can indicate that the detector readout is out of synchronization with the L1 trigger, or that a rapid sequence of trigger accepts has overflowed the readout buffers. These and a multitude of other possible errors are monitored during running. The readout system can tolerate and recover from periodic errors, but persistent errors indicate a problem that needs expert attention.

There are differences in specifics among the 3 subdetector types of the muon system, but the basics are the same. At this stage, data are declared good if a large fraction (at least 95%) of the detector channels register hits. A small number of readout errors is tolerated. If there are problems, the shifter can consult more detailed monitoring information to diagnose the problem. Detector experts are called to resolve potential problems as soon as possible.

Histograms aggregating information from the detectors and procedures for using them to evaluate the muon system operational integrity have been developed for the shift crew.

10.2 Offline monitoring

The offline DQM runs as part of the normal reconstruction process on all raw data at the tier-0 computing center (CERN), and as part of later re-reconstruction at the tier-1 centers using improved software or calibration and alignment information. It is also part of the standard validation procedure for new CMS software releases, for simulated data, and for updated alignment and calibration values. Here we focus specifically on the DQM performed on newly acquired data. Offline DQM of reconstructed data is carried out first by offline DQM shifters, then by members of the subdetector groups, normally with a latency period of a few days.

Standard data certification checks for readout errors and measures the detector occupancies again, as done in the online checks, but in greater detail. We can now look at reconstructed data from the accepted minimum bias stream, single-muon trigger stream, or dimuon trigger stream. Except at the very low luminosities of early LHC operation, the minimum bias event rate is small, often yielding poor statistics for judging detector performance.

Additional sources of information are available to aid the experts in the final pronouncement on data quality. These include logbooks for the subsystems, the insights of field managers and hardware experts, and information from full event reconstruction.

In addition, the DT and CSC systems monitor segment-related information. Monitored quantities include the following:

- the distribution across the detector of the rate of reconstructed segments;

- the distribution of residuals between hits and reconstructed segments (mean and RMS);

- the efficiency of matching hits to segments and/or matching segments to standalone tracks;

- timing of hits and segments;

- gas gain and noise in the chambers.

As an example, the overview in figure 50 shows the DT plots to be checked by the off-line shifter for data taken at the end of October 2010.

10.3 Quality of muon system operation in 2010

The muon system performed very well during the 2010 data-taking period. Generally, more than 98% of the channels were operational, and all the systems produced high-quality data for nearly all collision runs. These results are summarized in table 18. While the problems that affected data quality varied, the muon systems were responsible for the loss of less than 0.5% of CMS running time in 2010. The overall loss of CMS running time from all sources was 9%.
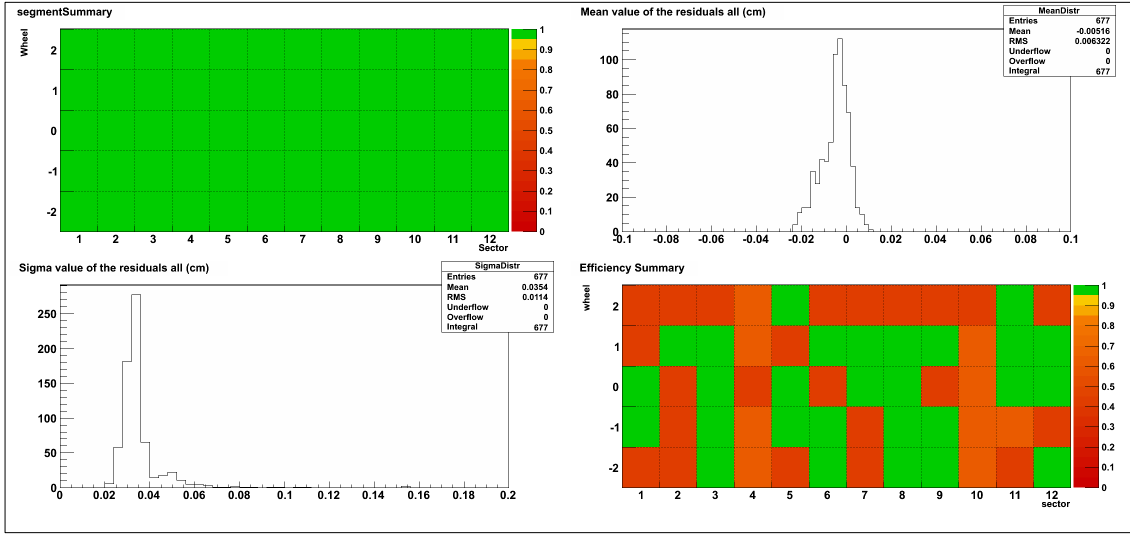
Figure 50. DQM GUI screen shot of a DT frame with DQM plots chosen to determine the quality of the data taken by the DTs for a single run taken during the last period of data taking in 2010. The plots are as follows: a summary of segment occupancy by wheel and sector (upper left), the means (upper right) and sigmas (lower left) of the distributions of the segment-hit residuals for each chamber, and the segment efficiency summary (lower right).

Table 18. Summary of the operational performance of the muon systems during 2010.

	DT	CSC	RPC
Fraction of operating subsystem channels at end of 2010 pp collision running	99.8%	98.5%	98.8%
Fraction of recorded pp collision data for which subsystem was operating	99.3%	99.1%	99.7%
Fraction of recorded pp collision data certified good	99.3%	99.0%	99.0%

11 Conclusions

We studied the performance of the CMS muon system by using a data sample corresponding to an integrated luminosity of $40\,\text{pb}^{-1}$ of proton-proton collisions at $\sqrt{s} = 7\,\text{TeV}$ in 2010 at the LHC. The sustained operation of all 3 subsystems (cathode strip chambers, drift tubes, and resistive plate chambers) at high efficiency demonstrated their robustness and reliability. The studies reported here show that the performance of the muon system meets the design parameters and is well reproduced by Monte Carlo simulation:

- The timing and synchronization of the system exceed the design specifications, achieving better than 99% in-time triggering.

- Precise calibration procedures have been established; they are particularly crucial for the DT system, where they are required for optimal local reconstruction.

- The CSC and DT systems provide fast trigger segments for the muon level-1 trigger, which closely match fully reconstructed segments offline with an efficiency above 96%.

- The efficiency for reconstructing local segments and hits is on average about 95% per muon station in the CSC and DT systems. The detection efficiency of the RPC layers is typically between 95 and 98%.

- Spatial resolutions for hits in all muon subdetector systems reach or exceed the design requirements in the Muon TDR [3] .

- Offline reconstructed times for hits and segments in the CSC and DT systems have resolutions of 3 ns or better.

- Backgrounds were measured and found to be controllable and largely in accordance with simulation.

- Alignment results using both hardware and reconstructed track-based techniques are compatible and provide the appropriate precision in detector positions for the reconstruction of muon tracks [15].

Data from proton-proton collisions at the LHC have enabled us to perform studies of muon system performance under operational conditions, and confirm that this performance matches or exceeds the design specifications.

Acknowledgments

A   Electronics performance

In a large experiment, like CMS, that is constructed in a large underground cavern, most of the detector is inaccessible except rarely during long shutdown periods. Furthermore, CMS is built in multiple layers and opening it for repairs or modifications takes considerable time and effort. Moreover, collision running quickly turns the experimental cavern into a highly radioactive environment, which increases the difficulty of servicing detector components. (In fact, the CMS detector was nearly inaccessible between March 2010 and March 2013 when it was opened again.) Therefore, each component of CMS must be robust and have a low failure rate. The collision running of 2010 presents an opportunity to assess the ability of the electronics to function reliably over many months.

Overall, the reliability of the electronic components was outstanding. Table 19 shows the number of failures that occurred in the on-chamber electronics (nearly all were inaccessible). For

Table 19. Failure rates for the various types of on-chamber muon system electronics. The number of failed boards during the 2010 running period is indicated followed by the percentage of the particular type of electronics this number represents. The acronyms identifying the boards are defined in the corresponding sections of the text.

Type	DT	CSC	RPC
Front-end boards	Superlayer 1 (0.15%)	CFEB 8 (0.3%)	0
	Front-end boards (FEB) 3 (0.03%)	AFEB 0 (0.0%)	
	Trigger boards (TRB) 1 (0.07%)	ALCT 1 (0.2%)	
Low voltage (LV)	0	3 LV cables (0.6%)	5 chambers (0.5%)
High voltage (HV)	26 channels (0.01%)	5 channels (0.5%)	39 channels (5.6%)

both the DTs and the CSCs, the board failure rate was less than 1% for all on-chamber electronics over the 2010 running period.

Although the on-chamber electronics failure rate was quite small, this does not mean that maintenance was unnecessary. Most of the off-chamber electronics was accessible during machine access periods and boards could be replaced or repaired.

The DTs had a variety of failures in accessible modules and all the faulty components were replaced. There were 11 failures in the low-voltage (LV) connectors, which were fixed by reseating the connector. There were 15 high-voltage (HV) power supply failures (5.0%). Among the readout electronics there were 3 DAQ board failures. There were the following failures in the trigger sector: 1 trigger selector collector (TSC) optical transmission (optoTX) mezzanine board (1.7%), 3 TSC input mezzanine boards (1.2%), and 2 TSC optical receiver (optoRX) boards (2.4%). In addition, 1 crate controller failed (10.0%).

The major maintenance issue for the CSCs was the high rate of reloading firmware. The EPROMs needed to be reloaded often; hardly a week went by without a firmware upload. In the CSC system, DAQ motherboards (DMB) and trigger motherboards (TMB) had to be replaced at a rate of roughly 1 every 2 months. Another challenging problem was a drop in the 3.3 V input to the TMB boards. This was finally traced to corrosion on the TMB fuses, which were replaced with ones with gold contacts.

The RPC maintenance problems during 2010 were relatively minor and easily resolved. An HV supply trip occurred about once a month. In the LV system, the failure rates were 3 CAEN A3009 power supply boards (3.2%), 1 A3016 power supply board (1.6%), and 1 A1676 branch controller board (5.9%). There were the following failures in the readout boards: 11 master link boards (2.2%), 3 slave link boards (1.0%), and 4 control boards (3.3%). These boards were all replaced during local stops and did not cause major interruptions during data taking.

The DT, CSC, and RPC systems were responsible for 1.1%, 5%, and 1.2% of the total CMS downtime in 2010, respectively.

Most off-chamber maintenance was accomplished during the frequent short accesses associated with LHC problems. Based on the 2010 running experience, we expect that the increase of luminosity for future running should not cause any notable rise in the failure rates for any muon system.

B Detector simulation

Simulation of the CMS detector is crucial in understanding the features, behavior, and appearance of real and hypothesized physics events in the component subdetectors. It was of course also critical in designing and optimizing the detectors, both in geometry and operating characteristics, before construction.

The CMS muon system consists of 3 different technologies: cathode strip chambers (CSC), drift chambers (DT), and resistive plate chambers (RPC). In each case a muon passing through a sensitive gas volume of the detector causes ionization of the gas. The free electrons drift towards an anode where a signal can be read out, and the positive ions drift more slowly towards a cathode. In the neighborhood of an anode wire, where the electric field reaches high values, gas amplification occurs and an image pulse is induced on the cathode plane. If the cathode is divided into strips, the location of the pulse, and hence the position of the ionizing particle, can be determined from the relative pulse heights on the strips. The CSCs and RPCs have relatively short drift distances (and hence short drift times) whereas the DTs have longer drift distances (and longer drift times). The DTs generate a precise hit location using precise measurement of the drift times, whereas the CSCs and RPCs use fine-grained cathode strips to measure the hit location.

The CMS experiment employs the GEANT4 package v6.2 [47] for the most precise and detailed simulation of detector operation and performance. GEANT4 uses a detailed model of the detector geometry and material composition to simulate the physics processes that occur as particles interact with the detector. These include energy loss (and energy deposition in the detectors) and multiple scattering, the bending of charged tracks due to the magnetic field, and the production — and subsequent tracking — of secondary particles. The output from this process is a collection of "GEANT4 simhits", for each subdetector, which provide information about the passage of each track through a sensitive detector volume. For example, in a subdetector sensitive to the passage of charged tracks, like all 3 types of detector in the muon system, a simhit contains the particle type, its energy, the position of entry to and exit from the detector volume, and the energy loss that occurred between the entry and exit points. In the muon system, the sensitive detector volume is a gas volume equivalent to a CSC layer, a DT cell, or a RPC single-gap module (double-gap RPC modules are approximated with a single active volume, called a "roll").

A further level of simulation is required to turn simhits into the quantities (e.g., charge, time, and position) that are recorded by the data acquisition system from the actual detectors. Owing to the hardware differences between the component subdetectors, this level of simulation must be subdetector specific. CMS generically refers to this process as "digitization" since it typically involves conversion of simulated analog quantities in the detectors into digitized quantities representing those read out from the electronic channels of the real detector (although these too may be digitized samples of analog quantities.) The output from digitization is a collection of "digi" objects. These were originally designed to be types of a common CMS-wide data structure intermediate between raw data and reconstructed data, and optimized for use in the reconstruction. Reconstruction is the process of interpreting the detector information in terms of particles interacting in those detectors; for example, in the muon detectors, the reconstruction includes the process of converting detected signals on electronic channels first to points in space, "rechits", at which a muon has crossed a detector, and then the construction of a momentum vector for a muon compatible with giving rise to those hits.

The overall output of the simulation of the muon system, for various physics event processes giving rise to muons, will be collections of simhits, digis, rechits, muon track segments (in chambers), and fully reconstructed muon tracks. These incorporate charges, times, positions, momenta, and any other quantities that are important to model, which can be compared with those from real data.

The comparison of real and simulated data allows us to monitor and improve the detector operating characteristics; to define and examine the muon trigger; and to diagnose malfunctioning chambers, faulty firmware, or problems arising in software at any stage of the detector operation from hardware to reconstruction. We can also model the effects of increasing luminosity (e.g., pileup, bunch structure, and dead time) and various potential backgrounds (including halo associated with the accelerated beams, cosmic rays, and effects induced by slow neutrons.)

B.1 GEANT4-level simulation

All 3 muon subdetectors provide a detailed and realistic description of the idealized geometry of the detectors, incorporated within the overall CMS geometrical description. This also provides a detailed specification of the materials composing the detector, including — in addition to the materials of the detectors proper — shielding, cables, and electronics modules. The ideal geometry model we use matches the hierarchical GEANT4 model, and this allows the local coordinates of the chambers in the system to be related to their global coordinates in the overall global coordinate system of CMS. Each chamber is typically considered to be a rigid body, with a geometrical specification given in terms of the physical dimensions, together with the global coordinates of a symmetry center, and a rotation matrix specifying its orientation in the global frame. The process of "alignment" of the detector leads to corrections to these ideal values in order that the actual positions of the chambers are known in the global frame. In either the ideal or real case, these geometrical specifications allow us to transform between the local and global coordinates.

It is important to note that not every aspect of a detector needs to be fully and precisely specified in this geometry. For example, in the CSC case, the geometries of the cathode strips and anode wires are not specified at this level (i.e., in terms of the global coordinate system). They are modeled locally only, within each chamber, and then transformation of their associated values to and from the global frame can be made as required using the overall geometry of the parent chamber.

B.2 Digitization

Each muon subdetector requires a specific simulation of the electronics and readout of that system. Each of the 3 digitizer packages starts from the GEANT4 simhits in the detector and produces one or more collections of digis, representing the different quantities read out from the detector:

- For DTs, each digi consists of a TDC time associated with an individual drift cell;

- For CSCs, 6 types of digis are created, corresponding to readout channels for strips, wire groups, and di-strip comparators, as well as for level-1 trigger local charged tracks (LCT) in the anode, cathode, and combined views;

- For RPCs, a digi is a pair of values: the fired strip code and the corresponding bunch crossing.

These digis are then packed into raw data format and stored. Subsequent reconstruction starts from the raw data format, just as in the case of real data.

B.2.1 DT digitization

The determination of the position of particles in the DT detectors is based on the measurement of the drift time of ionization electrons. An accurate modeling of the cell response, including the TDC measurement of the drift time information, is essential for a reliable simulation of physics events. The simulation of the cell response consists of the computation of the drift time of the electrons produced by ionization.

The simulation must reproduce not only the average behavior of the cell as a function of the track parameters and of the magnetic field, but also the smearing of the drift times, which determines the cell resolution. This is achieved with a parameterization of the drift cell behavior based on a detailed simulation with the GARFIELD package [22]. The drift time is parameterized as a function of the distance of the simulated hit from the wire, the incidence angle of the muon, and the magnetic field components parallel and orthogonal to the wire. This time is smeared according to a Gaussian-based distribution.

Hits from energetic δ-rays and any other secondaries (e.g., e^+e^- from pair production) crossing the whole cell are handled in the same way as muons. For the case of several hits in the same cell, the drift times are computed independently, but separate digis are created only if the difference in drift times is larger than the configurable dead time. The δ rays produced in the gas are ignored, since they are already generated by GARFIELD and their effect is included (statistically) in the parameterization. Soft electrons stopping in the gas cannot be handled by the parameterization and are currently ignored. Most of these hits cover a very short path and are not expected to produce a detectable signal.

Finally, since the DTs are time measuring devices, the delays contributing to the TDC measurement must be accounted for. The time-of-flight of the muons from the interaction point to the cell and the propagation time of the signal along the anode wire are added to the simulated time.

The emulation of the DT local trigger electronics uses as input the simulated signals produced as described above.

B.2.2 CSC digitization

The CSC digitization simulates the ionization of the CSC gas by generating a sequence of random steps along the line between a simhit entry and exit point, the end of each step corresponding to a collision between the ionizing particle and a gas molecule. At each collision energy transfer can occur, and if the transfer exceeds the ionization threshold of the gas, ionization occurs and a δ electron is produced. If of sufficient energy, such δ electrons can produce further ionization. The energy losses and the number of collisions per cm of gas used in the generation are based on tables extracted from GEANT4, created within the framework of the photoabsorption ionization model (which in effect extends the usual Bethe-Bloch equation to situations like thin layers of gas, where it is not directly applicable). This procedure results in a set of clusters of electrons distributed "randomly" across the gas gap, along the line defined by the simhit. Typically, about 100 free electrons are produced per gas gap.

These electrons then drift towards the anode plane, driven by the electric field, based on parameterizations of results from more detailed GEANT4 simulation. These provide the average drift times and drift distances along the wire direction (due to Lorentz drift in the magnetic field), and their variances, and hence specify Gaussian distributions from which random samplings can be made electron by electron. The parameterizations are functions of 3 variables: the magnetic field and the distances to the wire in both the direction of the wire plane and the direction perpendicular to the plane. Two sets of parameterizations were used, one for the ME1/1 chambers, which have smaller gas gaps and operate in high magnetic fields, and one for the others. The ME1/1 chambers have wires that are tilted at 29° to compensate for the relatively large Lorentz drift contribution, which tends to spread the collected charge; tilting the wires minimizes this dispersion. ME1/1 chambers have typical drift times of 20–40 ns, while the other chambers have drift times of 20–60 ns.

When an electron reaches a wire, the characteristic MWPC gas amplification is simulated: an avalanche of charge is created, according to a parameterized distribution, with factors to account for charge collection efficiency. We also account for electron attachment loss during drift through the gas. The charge on the wire is amplified and shaped into a signal on the readout channel of the corresponding wire group, according to the known specifications (delays, pulse-shaping, and amplification) of the actual hardware. The charge on the wire also induces image charge on the cathode plane: charge is induced on the 5 nearest cathode strips, according to the Gatti distribution [48], which models the expected charge distribution shape. Here too the charge on each strip is amplified and shaped into a signal on the strip readout channel according to the hardware specifications of the real electronics. The overall signals, which are represented as histograms of charge, are superimposed for all drift electrons and for all simhits contributing to that channel.

A "wire digi" contains 16 bits, each of which represents a 25 ns time bin. A bit is set for the corresponding time bin when the wire pulse exceeds a fixed threshold. To model random noise on the signal the simpler approach of applying, for each channel, a random Gaussian fluctuation to this threshold value is used.

The simulation of the cathode readout is more complex since it must take into account pedestal noise, which is correlated between switched capacitor array (SCA) time bins, and crosstalk between signal channels. The CSC calibration procedure provides a covariance matrix for the time-correlated pedestal noise; this is of dimension 8×8, since there are 8 SCA time bins per channel. The diagonal elements are taken from the measured widths of the pedestals in each time bin. All these measured values are stored in the standard CMS conditions data database, and can be accessed according to a date, or run number, of validity. A Cholesky decomposition of this covariance matrix then provides the appropriate matrix to apply to a vector of uncorrelated random pedestal noise values to give a vector of pedestal noise values with the appropriate covariance properties of the real CSC system. Crosstalk between channels is simulated by likewise making use of channel-specific values that represent the crosstalk measured in the periodic calibration procedure of the real CSC detector, and stored in the conditions data databases. Crosstalk typically results in a 10% transfer of charge from one strip to a neighbor. Since the crosstalk has a component proportional to the slope of the neighboring signal, it typically causes neighboring signals to peak earlier than the main signal. The cathode signal is split into 2 paths, with the trigger path resulting in "comparator digis", and the data path resulting in "strip digis".

The timings of the wire, strip, and comparator signals are tuned by first subtracting a time corresponding to the distance from the center of the readout element to the interaction point, divided by the speed of light. The speed of signal propagation from the hit position to the readout is measured in data, and was taken into account. Finally, we fine tune the centering of the timing using configurable constants for each ring of chambers.

The final step of the simulation involves modeling the level-1 trigger. The inputs are the wire and comparator digis, and the outputs are the 3 types of digi containing LCT information. Finally, we pack all the digis into the CSC raw data format. Just as in the hardware, some zero suppression of the strip signals is applied, based on the "pre-trigger" (i.e., early stages of the trigger algorithm). In the simulation this occurs during the cathode LCT simulation.

B.2.3 RPC digitization

Each RPC has up to 96 readout strips. The simulation of the real physical processes taking place inside the RPC is a complex and computer-intensive task. Therefore the RPC digitization is mostly parameterized. The digitization task is to assign 0, 1, or more digis to a hit and to simulate the detector noise.

The default digitization algorithm uses the following parameters from a dedicated database:

- efficiency parameter for each readout strip, i.e., 96 values per roll;

- noise rate parameter for each readout strip, i.e., 96 values per roll;

- timing parameter for each roll, i.e., 1 value per roll;

- cluster size distribution for each roll, i.e., 100 values per roll.

If the roll is hit by an ionizing particle, the digitizing algorithm will assign a digi to it with a probability defined by the efficiency parameter. The number of adjacent fired strips is calculated using an empirical cluster size distribution for each chamber. The impact point position is used to decide the fired strip coordinates. The signal propagation time and the timing parameter are used to decide the bunch crossing. Digis due to noise are simulated according to a Poisson distribution. Inter-roll crosstalk is negligible. The actual detectors have some dead or masked strips, which are treated in a very simple way by the digitization algorithm: the corresponding efficiency and noise rate parameters are set to 0 in the database.

The simulation parameters are updated regularly. Presently, 3 sets of parameters values are used:

- the "ideal" conditions (e.g., efficiency 95%);

- the parameters estimated using the cosmic-ray data;

- the parameters estimated by the proton-proton collision data.

While we lack the amount of data necessary to estimate the efficiency of each strip, the overall roll efficiency is well estimated. Thus, the efficiency averaged over a roll is assigned to each strip in the roll. The efficiency parameters are relatively constant over long periods of time, and are

updated a few times per year. The noisy and non-operational strips, however, may change run by run and are constantly monitored and updated in the database. Every database update is followed by a validation procedure. All of the simulation parameters are estimated using dedicated detector performance analysis. The same analysis is used to validate the simulation and compare it to data, with which it is in good agreement.

References

[1] L. Evans and P. Bryant, *LHC Machine*, 2008 *JINST* **3** S08001.

[2] CMS collaboration, *The CMS experiment at the CERN LHC*, 2008 *JINST* **3** S08004.

[3] CMS collaboration, *The CMS muon project: Technical Design Report*, CERN-LHCC-97-032 (1997).

[4] CMS collaboration, *Calibration of the CMS drift tube chambers and measurement of the drift velocity with cosmic rays*, 2010 *JINST* **5** T03016 [arXiv:0911.4895].

[5] CMS collaboration, *Performance of the CMS drift tube chambers with cosmic rays*, 2010 *JINST* **5** T03015 [arXiv:0911.4855].

[6] CMS collaboration, *Performance of the CMS drift-tube local trigger with cosmic rays*, 2010 *JINST* **5** T03003 [arXiv:0911.4893].

[7] CMS collaboration, *CMS data processing workflows during an extended cosmic ray run*, 2010 *JINST* **5** T03006 [arXiv:0911.4842].

[8] CMS collaboration, *Precise mapping of the magnetic field in the CMS barrel yoke using cosmic rays*, 2010 *JINST* **5** T03021 [arXiv:0910.5530].

[9] M.C. Fouz-Iglesias et al., *Measurement of drift velocity in the CMS barrel muon chambers at the CMS magnet test cosmic challenge*, CMS Note 2008-003 (2008).

[10] CMS collaboration, *Performance of the CMS cathode strip chambers with cosmic rays*, 2010 *JINST* **5** T03018 [arXiv:0911.4992].

[11] CMS collaboration, *Performance study of the CMS barrel resistive plate chambers with cosmic rays*, 2010 *JINST* **5** T03017 [arXiv:0911.4045].

[12] CMS collaboration, *Fine synchronization of the CMS muon drift-tube local trigger using cosmic rays*, 2010 *JINST* **5** T03004 [arXiv:0911.4904].

[13] CMS collaboration, *Alignment of the CMS muon system with cosmic-ray and beam-halo muons*, 2010 *JINST* **5** T03020 [arXiv:0911.4022].

[14] CMS collaboration, *Aligning the CMS muon chambers with the muon alignment system during an extended cosmic ray run*, 2010 *JINST* **5** T03019 [arXiv:0911.4770].

[15] CMS collaboration, *Performance of CMS muon reconstruction in pp collision events at $\sqrt{s} = 7$ TeV*, 2012 *JINST* **7** P10002 [arXiv:1206.4071].

[16] G. Charpak, G. Melchart, G. Petersen and F. Sauli, *High accuracy localization of minimum ionizing particles using the cathode induced charge center of gravity readout*, *Nucl. Instrum. Meth.* **167** (1979) 455.

[17] J. Christiansen, *HPTDC high performance time to digital converter*, CERN/EP-MIC, version 2.1, CERN, Geneva (2002).

[18] G. Altenhoefer, *Development of a drift chamber for drift velocity monitoring in the CMS barrel muon system*, Ph.D. thesis, III. Physikalisches Institut A, RWTH Aachen University, Aachen, Germany (2006) [http://web.physik.rwth-aachen.de/˜hebbeker/theses/altenhoefer_diploma.pdf].

[19] J. Frangenheim, *Measurements of the drift velocity using a small gas chamber for monitoring of the CMS muon system*, Ph.D. thesis, III. Physikalisches Institut A, RWTH Aachen University, Aachen, Germany (2007) [http://web.physik.rwth-aachen.de/˜hebbeker/theses/frangenheim_diploma.pdf].

[20] G. Abbiendi et al., *Offline calibration procedure of the CMS drift tube detectors*, 2009 *JINST* **4** P05002.

[21] N. Amapane et al., *Local muon reconstruction in the drift tube detectors*, CMS Note 2009-008 (2009).

[22] R. Veenhof, *Garfield, a Drift-Chamber Simulation Program User's Guide*, http://garfield.web.cern.ch/garfield/ (1994).

[23] R. Breedon et al., *Performance and radiation testing of a low-noise switched capacitor array for the CMS endcap muon system*, in proceedings of *6*th *Workshop on Electronics for LHC Experiments*, Cracow, Poland (2000), CMS-CR-2000-013.

[24] B.G. Bylsma et al., *The cathode strip chamber data acquisition electronics for CMS*, *Nucl. Instrum. Meth.* **A 600** (2009) 661.

[25] L. Tuura, A. Meyer, I. Segoni and G. Della Ricca, *CMS data quality monitoring: Systems and experiences*, *J. Phys. Conf. Ser.* **219** (2010) 072020.

[26] CMS collaboration, *CMS TriDAS project: Technical Design Report, Volume 1: The Trigger System*, CMS TDR CERN/LHCC 2000-038 (2000).

[27] P. Arce et al., *Bunched beam test of the CMS drift tubes local muon trigger*, *Nucl. Instrum. Meth.* **A 534** (2004) 441.

[28] M. Aldaya et al., *Results of the first integration test of the CMS drift tubes muon trigger*, *Nucl. Instrum. Meth.* **A 579** (2007) 951.

[29] J. Troska et al., *Implementation of the timing, trigger and control system of the CMS experiment*, *IEEE T. Nucl. Sci.* **53** (2006) 834.

[30] J. Hauser et al., *Experience with trigger electronics for the CSC system of CMS*, in proceedings of *Tenth workshop on electronics for LHC and future experiments*, Boston, MA, U.S.A., 13–17 September 2004, CERN-2004-010.

[31] H. Czyrkowski et al., *New developments on resistive plate chambers for high rate operation*, *Nucl. Instrum. Meth.* **A 419** (1998) 490.

[32] CMS collaboration, *CMS Physics: Technical Design Report Volume 1: Detector Performance and Software*, CMS TDR CERN/LHCC 2006-001 (2006).

[33] CMS collaboration, *Measurements of inclusive W and Z cross sections in pp collisions at $\sqrt{s} = 7$ TeV*, *JHEP* **01** (2011) 080 [arXiv:1012.2466].

[34] A.C. Rencher, *Linear Models in Statistics*, John Wiley & Sons Inc., N.Y., U.S.A. (2000).

[35] N.R. Draper and H. Smith, *Applied Regression Analysis*, third edition, John Wiley & Sons Inc., N.Y., U.S.A. (1998).

[36] Yu.V. Ershov et al., *Cathode strip chamber for CMS ME1/1 endcap muon station*, *Phys. Part. Nucl. Lett.* **3** (2006) 183.

[37] I.A. Golutvin et al., *ME1/1 cathode strip chambers for CMS experiment*, *Phys. Part. Nucl. Lett.* **6** (2009) 348.

[38] M. Benettoni et al., *CMS DT Chambers: Optimized measurement of cosmic cays crossing time in absence of magnetic field*, CMS Note 2008-017 (2008).

[39] M. Abbrescia et al., *Beam test results on double-gap resistive plate chambers proposed for CMS experiment*, *Nucl. Instrum. Meth.* **A 414** (1998) 135.

[40] E. Gatti, A. Longoni, P. Semenza and H. Okuno, *Optimum geometry for strip cathodes or grids in MWPC for avalanche localization along the anode wires*, *Nucl. Instrum. Meth.* **163** (1979) 83.

[41] J. S. Gordon and E. Mathieson, *Cathode charge distributions in multiwire chambers: I. Measurement and theory*, *Nucl. Instrum. Meth.* **227** (1984) 267.

[42] J. S. Gordon and E. Mathieson, *Cathode charge distributions in multiwire chambers: II. Approximate and empirical formulae*, *Nucl. Instrum. Meth.* **227** (1984) 277.

[43] C. Clopper and E. S. Pearson, *The use of confidence or fiducial limits illustrated in the case of the binomial*, *Biometrika* **26** (1934) 404.

[44] M. Huhtinen, *Optimization of the CMS forward shielding*, CMS Note 2000-068 (2000).

[45] P. Arce, *Object oriented software for simulation and reconstruction of big alignment systems*, *Nucl. Instrum. Meth.* **A 502** (2003) 696.

[46] CMS collaboration, *Commissioning of the CMS High-Level Trigger with Cosmic Rays*, 2010 *JINST* **5** T03005 [arXiv:0911.4889].

[47] GEANT4 collaboration, *GEANT4: a simulation toolkit*, *Nucl. Instrum. Meth.* **A 506** (2003) 250.

[48] E. Gatti, A. Longoni, R.A. Boie and V. Radeka, *Analysis of the position resolution in centroid measurements in Mwpc*, *Nucl. Instrum. Meth.* **188** (1981) 327.

The CMS collaboration

Yerevan Physics Institute, Yerevan, Armenia

S. Chatrchyan, V. Khachatryan, A.M. Sirunyan, A. Tumasyan

Institut für Hochenergiephysik der OeAW, Wien, Austria

W. Adam, E. Aguilo, T. Bergauer, M. Dragicevic, J. Erö, C. Fabjan[1], M. Friedl, R. Frühwirth[1], V.M. Ghete, N. Hörmann, J. Hrubec, M. Jeitler[1], W. Kiesenhofer, V. Knünz, M. Krammer[1], I. Krätschmer, D. Liko, I. Mikulec, M. Pernicka[†], D. Rabady[2], B. Rahbaran, C. Rohringer, H. Rohringer, R. Schöfbeck, J. Strauss, A. Taurok, W. Waltenberger, C.-E. Wulz[1]

National Centre for Particle and High Energy Physics, Minsk, Belarus

V. Mossolov, N. Shumeiko, J. Suarez Gonzalez

Universiteit Antwerpen, Antwerpen, Belgium

M. Bansal, S. Bansal, T. Cornelis, E.A. De Wolf, X. Janssen, S. Luyckx, L. Mucibello, S. Ochesanu, B. Roland, R. Rougny, M. Selvaggi, H. Van Haevermaet, P. Van Mechelen, N. Van Remortel, A. Van Spilbeeck

Vrije Universiteit Brussel, Brussel, Belgium

F. Blekman, S. Blyweert, J. D'Hondt, R. Gonzalez Suarez, A. Kalogeropoulos, M. Maes, A. Olbrechts, W. Van Doninck, P. Van Mulders, G.P. Van Onsem, I. Villella

Université Libre de Bruxelles, Bruxelles, Belgium

B. Clerbaux, G. De Lentdecker, V. Dero, A.P.R. Gay, T. Hreus, A. Léonard, P.E. Marage, A. Mohammadi, T. Reis, L. Thomas, C. Vander Velde, P. Vanlaer, J. Wang

Ghent University, Ghent, Belgium

V. Adler, K. Beernaert, A. Cimmino, S. Costantini, G. Garcia, M. Grunewald, B. Klein, J. Lellouch, A. Marinov, J. Mccartin, A.A. Ocampo Rios, D. Ryckbosch, N. Strobbe, F. Thyssen, M. Tytgat, S. Walsh, E. Yazgan, N. Zaganidis

Université Catholique de Louvain, Louvain-la-Neuve, Belgium

S. Basegmez, G. Bruno, R. Castello, L. Ceard, C. Delaere, T. du Pree, D. Favart, L. Forthomme, A. Giammanco[3], J. Hollar, V. Lemaitre, J. Liao, O. Militaru, C. Nuttens, D. Pagano, A. Pin, K. Piotrzkowski, J.M. Vizan Garcia

Université de Mons, Mons, Belgium

N. Beliy, T. Caebergs, E. Daubie, G.H. Hammad

Centro Brasileiro de Pesquisas Fisicas, Rio de Janeiro, Brazil

G.A. Alves, M. Correa Martins Junior, T. Martins, M.E. Pol, M.H.G. Souza

Universidade do Estado do Rio de Janeiro, Rio de Janeiro, Brazil

W.L. Aldá Júnior, W. Carvalho, A. Custódio, E.M. Da Costa, D. De Jesus Damiao, C. De Oliveira Martins, S. Fonseca De Souza, H. Malbouisson, M. Malek, D. Matos Figueiredo, L. Mundim, H. Nogima, W.L. Prado Da Silva, A. Santoro, L. Soares Jorge, A. Sznajder, A. Vilela Pereira

Universidade Estadual Paulista [a], Universidade Federal do ABC [b], São Paulo, Brazil

T.S. Anjos[b], C.A. Bernardes[b], F.A. Dias[a,4], T.R. Fernandez Perez Tomei[a], E.M. Gregores[b], C. Lagana[a], F. Marinho[a], P.G. Mercadante[b], S.F. Novaes[a], Sandra S. Padula[a]

Institute for Nuclear Research and Nuclear Energy, Sofia, Bulgaria

V. Genchev[2], P. Iaydjiev[2], S. Piperov, M. Rodozov, S. Stoykova, G. Sultanov, V. Tcholakov, R. Trayanov, M. Vutova

University of Sofia, Sofia, Bulgaria

A. Dimitrov, R. Hadjiiska, V. Kozhuharov, L. Litov, B. Pavlov, P. Petkov

Institute of High Energy Physics, Beijing, China

J.G. Bian, G.M. Chen, H.S. Chen, C.H. Jiang, D. Liang, S. Liang, X. Meng, J. Tao, J. Wang, X. Wang, Z. Wang, H. Xiao, M. Xu, J. Zang, Z. Zhang

State Key Laboratory of Nuclear Physics and Technology, Peking University, Beijing, China

C. Asawatangtrakuldee, Y. Ban, Y. Guo, Q. Li, W. Li, S. Liu, Y. Mao, S.J. Qian, D. Wang, L. Zhang, W. Zou

Universidad de Los Andes, Bogota, Colombia

C. Avila, J.P. Gomez, B. Gomez Moreno, A.F. Osorio Oliveros, J.C. Sanabria

Technical University of Split, Split, Croatia

N. Godinovic, D. Lelas, R. Plestina[5], D. Polic, I. Puljak[2]

University of Split, Split, Croatia

Z. Antunovic, M. Kovac

Institute Rudjer Boskovic, Zagreb, Croatia

V. Brigljevic, S. Duric, K. Kadija, J. Luetic, D. Mekterovic, S. Morovic

University of Cyprus, Nicosia, Cyprus

A. Attikis, M. Galanti, G. Mavromanolakis, J. Mousa, C. Nicolaou, F. Ptochos, P.A. Razis

Charles University, Prague, Czech Republic

M. Finger, M. Finger Jr.

Academy of Scientific Research and Technology of the Arab Republic of Egypt, Egyptian Network of High Energy Physics, Cairo, Egypt

A.A. Abdelalim[6], Y. Assran[7], S. Elgammal[6], A. Ellithi Kamel[8], M.A. Mahmoud[9], A. Radi[10,11]

National Institute of Chemical Physics and Biophysics, Tallinn, Estonia

M. Kadastik, M. Müntel, M. Raidal, L. Rebane, A. Tiko

Department of Physics, University of Helsinki, Helsinki, Finland

P. Eerola, G. Fedi, M. Voutilainen

Helsinki Institute of Physics, Helsinki, Finland

J. Härkönen, A. Heikkinen, V. Karimäki, R. Kinnunen, M.J. Kortelainen, T. Lampén, K. Lassila-Perini, S. Lehti, T. Lindén, P. Luukka, T. Mäenpää, T. Peltola, E. Tuominen, J. Tuominiemi, E. Tuovinen, D. Ungaro, L. Wendland

Lappeenranta University of Technology, Lappeenranta, Finland

K. Banzuzi, A. Karjalainen, A. Korpela, T. Tuuva

DSM/IRFU, CEA/Saclay, Gif-sur-Yvette, France

M. Besancon, S. Choudhury, M. Dejardin, D. Denegri, B. Fabbro, J.L. Faure, F. Ferri, S. Ganjour, A. Givernaud, P. Gras, G. Hamel de Monchenault, P. Jarry, E. Locci, J. Malcles, L. Millischer, A. Nayak, J. Rander, A. Rosowsky, M. Titov

Laboratoire Leprince-Ringuet, Ecole Polytechnique, IN2P3-CNRS, Palaiseau, France

S. Baffioni, F. Beaudette, L. Benhabib, L. Bianchini, M. Bluj[12], P. Busson, C. Charlot, N. Daci, T. Dahms, M. Dalchenko, L. Dobrzynski, A. Florent, R. Granier de Cassagnac, M. Haguenauer, P. Miné, C. Mironov, I.N. Naranjo, M. Nguyen, C. Ochando, P. Paganini, D. Sabes, R. Salerno, Y. Sirois, C. Veelken, A. Zabi

Institut Pluridisciplinaire Hubert Curien, Université de Strasbourg, Université de Haute Alsace Mulhouse, CNRS/IN2P3, Strasbourg, France

J.-L. Agram[13], J. Andrea, D. Bloch, D. Bodin, J.-M. Brom, M. Cardaci, E.C. Chabert, C. Collard, E. Conte[13], F. Drouhin[13], J.-C. Fontaine[13], D. Gelé, U. Goerlach, P. Juillot, A.-C. Le Bihan, P. Van Hove

Centre de Calcul de l'Institut National de Physique Nucleaire et de Physique des Particules, CNRS/IN2P3, Villeurbanne, France

F. Fassi, D. Mercier

Université de Lyon, Université Claude Bernard Lyon 1, CNRS-IN2P3, Institut de Physique Nucléaire de Lyon, Villeurbanne, France

S. Beauceron, N. Beaupere, O. Bondu, G. Boudoul, S. Brochet, J. Chasserat, R. Chierici[2], D. Contardo, P. Depasse, H. El Mamouni, J. Fay, S. Gascon, M. Gouzevitch, B. Ille, T. Kurca, M. Lethuillier, L. Mirabito, S. Perries, L. Sgandurra, V. Sordini, Y. Tschudi, P. Verdier, S. Viret

Institute of High Energy Physics and Informatization, Tbilisi State University, Tbilisi, Georgia

Z. Tsamalaidze[14]

RWTH Aachen University, I. Physikalisches Institut, Aachen, Germany

C. Autermann, S. Beranek, B. Calpas, M. Edelhoff, L. Feld, N. Heracleous, O. Hindrichs, R. Jussen, K. Klein, J. Merz, A. Ostapchuk, A. Perieanu, F. Raupach, J. Sammet, S. Schael, D. Sprenger, H. Weber, B. Wittmer, V. Zhukov[15]

RWTH Aachen University, III. Physikalisches Institut A, Aachen, Germany

F. Adamczyk, A. Adolf, M. Ata, K. Bosseler, J. Caudron, E. Dietz-Laursonn, D. Duchardt, M. Erdmann, G. Fetchenhauer, R. Fischer, J.H. Frohn, J. Grooten, A. Güth, T. Hebbeker, C. Heidemann, E. Hermens, G. Hilgers, K. Hoepfner, D. Klingebiel, P. Kreuzer, R. Kupper, H.R. Lampe, M. Merschmeyer, A. Meyer, M. Olschewski, P. Papacz, B. Philipps, H. Pieta, H. Reithler, W. Reuter, S.A. Schmitz, L. Sonnenschein, J. Steggemann, H. Szczesny, D. Teyssier, S. Thüer, M. Weber

RWTH Aachen University, III. Physikalisches Institut B, Aachen, Germany

M. Bontenackels, V. Cherepanov, Y. Erdogan, G. Flügge, H. Geenen, M. Geisler, W. Haj Ahmad, F. Hoehle, B. Kargoll, T. Kress, Y. Kuessel, J. Lingemann[2], A. Nowack, L. Perchalla, O. Pooth, P. Sauerland, A. Stahl

Deutsches Elektronen-Synchrotron, Hamburg, Germany

M. Aldaya Martin, J. Behr, W. Behrenhoff, U. Behrens, M. Bergholz[16], A. Bethani, K. Borras, A. Burgmeier, A. Cakir, L. Calligaris, A. Campbell, E. Castro, F. Costanza, D. Dammann, C. Diez Pardos, G. Eckerlin, D. Eckstein, G. Flucke, A. Geiser, I. Glushkov, P. Gunnellini, S. Habib, J. Hauk, G. Hellwig, H. Jung, M. Kasemann, P. Katsas, C. Kleinwort, H. Kluge, A. Knutsson, M. Krämer, D. Krücker, E. Kuznetsova, W. Lange, J. Leonard, W. Lohmann[16], B. Lutz, R. Mankel, I. Marfin, M. Marienfeld, I.-A. Melzer-Pellmann, A.B. Meyer, J. Mnich, A. Mussgiller, S. Naumann-Emme, O. Novgorodova, J. Olzem, H. Perrey, A. Petrukhin, D. Pitzl, A. Raspereza, P.M. Ribeiro Cipriano, C. Riedl, E. Ron, M. Rosin, J. Salfeld-Nebgen, R. Schmidt[16], T. Schoerner-Sadenius, N. Sen, A. Spiridonov, M. Stein, R. Walsh, C. Wissing

University of Hamburg, Hamburg, Germany

V. Blobel, H. Enderle, J. Erfle, U. Gebbert, M. Görner, M. Gosselink, J. Haller, T. Hermanns, R.S. Höing, K. Kaschube, G. Kaussen, H. Kirschenmann, R. Klanner, J. Lange, F. Nowak, T. Peiffer, N. Pietsch, D. Rathjens, C. Sander, H. Schettler, P. Schleper, E. Schlieckau, A. Schmidt, M. Schröder, T. Schum, M. Seidel, J. Sibille[17], V. Sola, H. Stadie, G. Steinbrück, J. Thomsen, L. Vanelderen

Institut für Experimentelle Kernphysik, Karlsruhe, Germany

C. Barth, J. Berger, C. Böser, T. Chwalek, W. De Boer, A. Descroix, A. Dierlamm, M. Feindt, M. Guthoff[2], C. Hackstein, F. Hartmann[2], T. Hauth[2], M. Heinrich, H. Held, K.H. Hoffmann, U. Husemann, I. Katkov[15], J.R. Komaragiri, P. Lobelle Pardo, D. Martschei, S. Mueller, Th. Müller, M. Niegel, A. Nürnberg, O. Oberst, A. Oehler, J. Ott, G. Quast, K. Rabbertz, F. Ratnikov, N. Ratnikova, S. Röcker, F.-P. Schilling, G. Schott, H.J. Simonis, F.M. Stober, D. Troendle, R. Ulrich, J. Wagner-Kuhr, S. Wayand, T. Weiler, M. Zeise

Institute of Nuclear and Particle Physics (INPP), NCSR Demokritos, Aghia Paraskevi, Greece

G. Anagnostou, G. Daskalakis, T. Geralis, S. Kesisoglou, A. Kyriakis, D. Loukas, I. Manolakos, A. Markou, C. Markou, E. Ntomari

University of Athens, Athens, Greece

L. Gouskos, T.J. Mertzimekis, A. Panagiotou, N. Saoulidou

University of Ioánnina, Ioánnina, Greece

I. Evangelou, C. Foudas, P. Kokkas, N. Manthos, I. Papadopoulos, V. Patras

KFKI Research Institute for Particle and Nuclear Physics, Budapest, Hungary

G. Bencze, C. Hajdu, P. Hidas, D. Horvath[18], F. Sikler, V. Veszpremi, G. Vesztergombi[19]

Institute of Nuclear Research ATOMKI, Debrecen, Hungary

N. Beni, S. Czellar, J. Molnar, J. Palinkas, Z. Szillasi

University of Debrecen, Debrecen, Hungary

J. Karancsi, P. Raics, Z.L. Trocsanyi, B. Ujvari, G. Zilizi

Panjab University, Chandigarh, India

S.B. Beri, V. Bhatnagar, N. Dhingra, R. Gupta, M. Kaur, M.Z. Mehta, N. Nishu, L.K. Saini, A. Sharma, J.B. Singh

University of Delhi, Delhi, India

Ashok Kumar, Arun Kumar, S. Ahuja, A. Bhardwaj, B.C. Choudhary, S. Malhotra, M. Naimuddin, K. Ranjan, V. Sharma, R.K. Shivpuri

Saha Institute of Nuclear Physics, Kolkata, India

S. Banerjee, S. Bhattacharya, S. Dutta, B. Gomber, Sa. Jain, Sh. Jain, R. Khurana, S. Sarkar, M. Sharan

Bhabha Atomic Research Centre, Mumbai, India

A. Abdulsalam, D. Dutta, S. Kailas, V. Kumar, A.K. Mohanty[2], L.M. Pant, P. Shukla

Tata Institute of Fundamental Research - EHEP, Mumbai, India

T. Aziz, S. Ganguly, M. Guchait[20], A. Gurtu[21], M. Maity[22], G. Majumder, K. Mazumdar, G.B. Mohanty, B. Parida, K. Sudhakar, N. Wickramage

Tata Institute of Fundamental Research - HECR, Mumbai, India

S. Banerjee, S. Dugad

Institute for Research in Fundamental Sciences (IPM), Tehran, Iran

H. Arfaei[23], H. Bakhshiansohi, S.M. Etesami[24], A. Fahim[23], M. Hashemi[25], H. Hesari, A. Jafari, M. Khakzad, M. Mohammadi Najafabadi, S. Paktinat Mehdiabadi, B. Safarzadeh[26], M. Zeinali

INFN Sezione di Bari ^{a}, Università di Bari ^{b}, Politecnico di Bari ^{c}, Bari, Italy

M. Abbrescia^{a,b}, L. Barbone^{a,b}, C. Calabria^{a,b}, S.S. Chhibra^{a,b}, A. Clemente^a, A. Colaleo^a, D. Creanza^{a,c}, N. De Filippis^{a,c}, M. De Palma^{a,b}, G. De Robertis^a, L. Fiore^a, M. Franco^a, G. Iaselli^{a,c}, N. Lacalamita^a, F. Loddo^a, G. Maggi^{a,c}, M. Maggi^a, B. Marangelli^{a,b}, S. My^{a,c}, S. Nuzzo^{a,b}, G. Papagni^a, A. Pompili^{a,b}, G. Pugliese^{a,c}, A. Ranieri^a, G. Selvaggi^{a,b}, L. Silvestris^a, G. Singh^{a,b}, R. Venditti^{a,b}, P. Verwilligen^a, G. Zito^a

INFN Sezione di Bologna ^{a}, Università di Bologna ^{b}, Bologna, Italy

G. Abbiendi^a, A.C. Benvenuti^a, M. Boldini^a, D. Bonacorsi^{a,b}, S. Braibant-Giacomelli^{a,b}, L. Brigliadori^{a,b}, V.D. Cafaro^a, P. Capiluppi^{a,b}, A. Castro^{a,b}, F.R. Cavallo^a, M. Cuffiani^{a,b}, I. D'Antone^a, G.M. Dallavalle^a, F. Fabbri^a, A. Fanfani^{a,b}, D. Fasanella^{a,b}, P. Giacomelli^a, V. Giordano^a, C. Grandi^a, L. Guiducci^{a,b}, S. Marcellini^a, G. Masetti^a, M. Meneghelli^{a,b,2}, A. Montanari^a, F.L. Navarria^{a,b}, F. Odorici^a, G. Pellegrini^a, A. Perrotta^a, F. Primavera^{a,b}, A.M. Rossi^{a,b}, T. Rovelli^{a,b}, G.P. Siroli^{a,b}, G. Torromeo^a, N. Tosi^{a,b}, R. Travaglini^{a,b}

INFN Sezione di Catania ^{a}, Università di Catania ^{b}, Catania, Italy

S. Albergo^{a,b}, G. Cappello^{a,b}, M. Chiorboli^{a,b}, S. Costa^{a,b}, R. Potenza^{a,b}, A. Tricomi^{a,b}, C. Tuve^{a,b}

INFN Sezione di Firenze [a], Università di Firenze [b], Firenze, Italy

G. Barbagli[a], V. Ciulli[a,b], C. Civinini[a], R. D'Alessandro[a,b], E. Focardi[a,b], S. Frosali[a,b], E. Gallo[a], S. Gonzi[a,b], M. Meschini[a], S. Paoletti[a], G. Sguazzoni[a], A. Tropiano[a,b]

INFN Laboratori Nazionali di Frascati, Frascati, Italy

L. Benussi, S. Bianco, S. Colafranceschi[27], F. Fabbri, D. Piccolo, G. Saviano[27]

INFN Sezione di Genova [a], Università di Genova [b], Genova, Italy

P. Fabbricatore[a], R. Musenich[a], S. Tosi[a,b]

INFN Sezione di Milano-Bicocca [a], Università di Milano-Bicocca [b], Milano, Italy

A. Benaglia[a], F. De Guio[a,b], L. Di Matteo[a,b,2], S. Fiorendi[a,b], S. Gennai[a,2], A. Ghezzi[a,b], S. Malvezzi[a], R.A. Manzoni[a,b], A. Martelli[a,b], A. Massironi[a,b], D. Menasce[a], L. Moroni[a], M. Paganoni[a,b], D. Pedrini[a], S. Ragazzi[a,b], N. Redaelli[a], S. Sala[a], T. Tabarelli de Fatis[a,b]

INFN Sezione di Napoli [a], Università di Napoli 'Federico II' [b], Università della Basilicata (Potenza) [c], Università G. Marconi (Roma) [d], Napoli, Italy

S. Buontempo[a], C.A. Carrillo Montoya[a], F. Cassese[a], N. Cavallo[a,c], A. De Cosa[a,b,2], F. Fabozzi[a,c], A.O.M. Iorio[a,b,2], L. Lista[a], S. Meola[a,d,2], M. Merola[a], P. Paolucci[a,2], G. Passeggio[a], L. Roscilli[a], A. Vanzanella[a]

INFN Sezione di Padova [a], Università di Padova [b], Università di Trento (Trento) [c], Padova, Italy

P. Azzi[a], N. Bacchetta[a,2], P. Bellan[a,b], M. Bellato[a], M. Benettoni[a], A. Branca[a,b,2], R. Carlin[a,b], P. Checchia[a], T. Dorigo[a], F. Gasparini[a,b], F. Gonella[a], A. Gozzelino[a], K. Kanishchev[a,c], S. Lacaprara[a], I. Lazzizzera[a,c], M. Margoni[a,b], A.T. Meneguzzo[a,b], F. Montecassiano[a], M. Passaseo[a], J. Pazzini[a,b], M. Pegoraro[a], N. Pozzobon[a,b], P. Ronchese[a,b], F. Simonetto[a,b], E. Torassa[a], M. Tosi[a,b], A. Triossi[a], S. Vanini[a,b], S. Ventura[a], P. Zotto[a,b], G. Zumerle[a,b]

INFN Sezione di Pavia [a], Università di Pavia [b], Pavia, Italy

G. Belli[a,b†], M. Gabusi[a,b], G. Musitelli[a], R. Nardo[a], S.P. Ratti[a,b], C. Riccardi[a,b], P. Torre[a,b], A. Vicini[a], P. Vitulo[a,b]

INFN Sezione di Perugia [a], Università di Perugia [b], Perugia, Italy

M. Biasini[a,b], G.M. Bilei[a], L. Fanò[a,b], P. Lariccia[a,b], G. Mantovani[a,b], M. Menichelli[a], A. Nappi[a,b†], F. Romeo[a,b], A. Saha[a], A. Santocchia[a,b], A. Spiezia[a,b], S. Taroni[a,b]

INFN Sezione di Pisa [a], Università di Pisa [b], Scuola Normale Superiore di Pisa [c], Pisa, Italy

P. Azzurri[a,c], G. Bagliesi[a], J. Bernardini[a], T. Boccali[a], G. Broccolo[a,c], R. Castaldi[a], R.T. D'Agnolo[a,c,2], R. Dell'Orso[a], F. Fiori[a,b,2], L. Foà[a,c], A. Giassi[a], A. Kraan[a], F. Ligabue[a,c], T. Lomtadze[a], L. Martini[a,28], A. Messineo[a,b], F. Palla[a], A. Rizzi[a,b], A.T. Serban[a,29], P. Spagnolo[a], P. Squillacioti[a,2], R. Tenchini[a], G. Tonelli[a,b], A. Venturi[a], P.G. Verdini[a]

INFN Sezione di Roma [a], Università di Roma [b], Roma, Italy

L. Barone[a,b], F. Cavallari[a], D. Del Re[a,b], M. Diemoz[a], C. Fanelli[a,b], M. Grassi[a,b,2], E. Longo[a,b], P. Meridiani[a,2], F. Micheli[a,b], S. Nourbakhsh[a,b], G. Organtini[a,b], R. Paramatti[a], S. Rahatlou[a,b], M. Sigamani[a], L. Soffi[a,b]

INFN Sezione di Torino [a]**, Università di Torino** [b]**, Università del Piemonte Orientale (Novara)** [c]**, Torino, Italy**

G. Alampi[a], N. Amapane[a,b], R. Arcidiacono[a,c], S. Argiro[a,b], M. Arneodo[a,c], C. Biino[a], N. Cartiglia[a], S. Casasso[a,b], M. Costa[a,b], D. Dattola[a], G. Dellacasa[a], N. Demaria[a], G. Dughera[a], D. Grasso[a], D. Kostylev[a], G. Kostyleva[a], C. Mariotti[a,2], S. Maselli[a], P. Mereu[a], E. Migliore[a,b], V. Monaco[a,b], M. Musich[a,2], M. Nervo[a,b], M.M. Obertino[a,c], R. Panero[a], N. Pastrone[a], M. Pelliccioni[a], C. Peroni[a,b], A. Potenza[a,b], A. Romero[a,b], M. Ruspa[a,c], R. Sacchi[a,b], M. Scalise[a], A. Solano[a,b], A. Staiano[a], E. Vacchieri[a], A. Zampieri[a]

INFN Sezione di Trieste [a]**, Università di Trieste** [b]**, Trieste, Italy**

S. Belforte[a], V. Candelise[a,b], M. Casarsa[a], F. Cossutti[a], G. Della Ricca[a,b], B. Gobbo[a], M. Marone[a,b,2], D. Montanino[a,b,2], A. Penzo[a], A. Schizzi[a,b]

Kangwon National University, Chunchon, Korea

T.Y. Kim, S.K. Nam

Kyungpook National University, Daegu, Korea

S. Chang, D.H. Kim, G.N. Kim, D.J. Kong, H. Park, D.C. Son, T. Son

Chonnam National University, Institute for Universe and Elementary Particles, Kwangju, Korea

J.Y. Kim, Zero J. Kim, S. Song

Korea University, Seoul, Korea

S. Choi, D. Gyun, B. Hong, M. Jo, H. Kim, T.J. Kim, K.S. Lee, D.H. Moon, S.K. Park, Y. Roh

University of Seoul, Seoul, Korea

M. Choi, J.H. Kim, C. Park, I.C. Park, S. Park, G. Ryu

Sungkyunkwan University, Suwon, Korea

Y. Choi, Y.K. Choi, J. Goh, M.S. Kim, E. Kwon, B. Lee, J. Lee, S. Lee, H. Seo, I. Yu

Vilnius University, Vilnius, Lithuania

M.J. Bilinskas, I. Grigelionis, M. Janulis, A. Juodagalvis

Centro de Investigacion y de Estudios Avanzados del IPN, Mexico City, Mexico

H. Castilla-Valdez, E. De La Cruz-Burelo, I. Heredia-de La Cruz, R. Lopez-Fernandez, J. Martínez-Ortega, A. Sanchez-Hernandez, L.M. Villasenor-Cendejas

Universidad Iberoamericana, Mexico City, Mexico

S. Carrillo Moreno, F. Vazquez Valencia

Benemerita Universidad Autonoma de Puebla, Puebla, Mexico

H.A. Salazar Ibarguen

Universidad Autónoma de San Luis Potosí, San Luis Potosí, Mexico

E. Casimiro Linares, A. Morelos Pineda, M.A. Reyes-Santos

University of Auckland, Auckland, New Zealand

D. Krofcheck

University of Canterbury, Christchurch, New Zealand

A.J. Bell, P.H. Butler, R. Doesburg, S. Reucroft, H. Silverwood

National Centre for Physics, Quaid-I-Azam University, Islamabad, Pakistan

M. Ahmad, M.I. Asghar, J. Butt, H.R. Hoorani, S. Khalid, W.A. Khan, T. Khurshid, S. Qazi, M.A. Shah, M. Shoaib

National Centre for Nuclear Research, Swierk, Poland

H. Bialkowska, B. Boimska, T. Frueboes, M. Górski, M. Kazana, K. Nawrocki, K. Romanowska-Rybinska, M. Szleper, G. Wrochna, P. Zalewski

Institute of Experimental Physics, Faculty of Physics, University of Warsaw, Warsaw, Poland

G. Brona, K. Bunkowski, M. Cwiok, W. Dominik, K. Doroba, A. Kalinowski, M. Konecki, J. Krolikowski, M. Misiura

Laboratório de Instrumentação e Física Experimental de Partículas, Lisboa, Portugal

N. Almeida, P. Bargassa, A. David, P. Faccioli, P.G. Ferreira Parracho, M. Gallinaro, J. Seixas, J. Varela, P. Vischia

Joint Institute for Nuclear Research, Dubna, Russia

I. Belotelov, A. Golunov, I. Golutvin, N. Gorbounov, I. Gramenitski, A. Kamenev, V. Karjavin, A. Kurenkov, A. Lanev, A. Makankin, P. Moisenz, V. Palichik, V. Perelygin, S. Shmatov, D. Smolin, S. Vasil'ev, A. Zarubin

Petersburg Nuclear Physics Institute, Gatchina (St. Petersburg), Russia

S. Evstyukhin, V. Golovtsov, Y. Ivanov, V. Kim, P. Levchenko, V. Murzin, V. Oreshkin, I. Smirnov, V. Sulimov, L. Uvarov, S. Vavilov, A. Vorobyev, An. Vorobyev

Institute for Nuclear Research, Moscow, Russia

Yu. Andreev, A. Dermenev, S. Gninenko, N. Golubev, M. Kirsanov, N. Krasnikov, V. Matveev, A. Pashenkov, D. Tlisov, A. Toropin

Institute for Theoretical and Experimental Physics, Moscow, Russia

V. Epshteyn, M. Erofeeva, V. Gavrilov, M. Kossov, N. Lychkovskaya, V. Popov, G. Safronov, S. Semenov, I. Shreyber, V. Stolin, E. Vlasov, A. Zhokin

P.N. Lebedev Physical Institute, Moscow, Russia

V. Andreev, M. Azarkin, I. Dremin, M. Kirakosyan, A. Leonidov, G. Mesyats, S.V. Rusakov, A. Vinogradov

Skobeltsyn Institute of Nuclear Physics, Lomonosov Moscow State University, Moscow, Russia

A. Belyaev, E. Boos, M. Dubinin[4], L. Dudko, A. Ershov, A. Gribushin, A. Kaminskiy[30], V. Klyukhin, O. Kodolova, I. Lokhtin, A. Markina, S. Obraztsov, M. Perfilov, S. Petrushanko, A. Popov, L. Sarycheva[†], V. Savrin

State Research Center of Russian Federation, Institute for High Energy Physics, Protvino, Russia

I. Azhgirey, I. Bayshev, S. Bitioukov, V. Grishin[2], V. Kachanov, D. Konstantinov, V. Krychkine, V. Petrov, R. Ryutin, A. Sobol, L. Tourtchanovitch, S. Troshin, N. Tyurin, A. Uzunian, A. Volkov

University of Belgrade, Faculty of Physics and Vinca Institute of Nuclear Sciences, Belgrade, Serbia

P. Adzic[31], M. Djordjevic, M. Ekmedzic, D. Krpic[31], J. Milosevic

Centro de Investigaciones Energéticas Medioambientales y Tecnológicas (CIEMAT), Madrid, Spain

M. Aguilar-Benitez, J. Alcaraz Maestre, P. Arce, J.M. Barcala, C. Battilana, C. Burgos Lazaro, E. Calvo, J.M. Cela Ruiz, M. Cerrada, M. Chamizo Llatas, N. Colino, B. De La Cruz, A. Delgado Peris, D. Domínguez Vázquez, C. Fernandez Bedoya, J.P. Fernández Ramos, A. Ferrando, J. Flix, M.C. Fouz, P. Garcia-Abia, O. Gonzalez Lopez, S. Goy Lopez, J.M. Hernandez, M.I. Josa, J. Marin, G. Merino, A. Molinero, J.J. Navarrete, Á. Navarro Tobar, J.C. Oller, J. Puerta Pelayo, A. Quintario Olmeda, I. Redondo, L. Romero, J. Santaolalla, M.S. Soares, C. Willmott

Universidad Autónoma de Madrid, Madrid, Spain

C. Albajar, G. Codispoti, J.F. de Trocóniz

Universidad de Oviedo, Oviedo, Spain

H. Brun, J. Cuevas, J. Fernandez Menendez, S. Folgueras, I. Gonzalez Caballero, L. Lloret Iglesias, J. Piedra Gomez

Instituto de Física de Cantabria (IFCA), CSIC-Universidad de Cantabria, Santander, Spain

J.A. Brochero Cifuentes, I.J. Cabrillo, A. Calderon, S.H. Chuang, J. Duarte Campderros, M. Felcini[32], M. Fernandez, G. Gomez, J. Gonzalez Sanchez, A. Graziano, C. Jorda, A. Lopez Virto, J. Marco, R. Marco, C. Martinez Rivero, F. Matorras, F.J. Munoz Sanchez, T. Rodrigo, A.Y. Rodríguez-Marrero, A. Ruiz-Jimeno, L. Scodellaro, I. Vila, R. Vilar Cortabitarte

CERN, European Organization for Nuclear Research, Geneva, Switzerland

D. Abbaneo, E. Auffray, G. Auzinger, M. Bachtis, P. Baillon, A.H. Ball, D. Barney, J.F. Benitez, C. Bernet[5], G. Bianchi, P. Bloch, A. Bocci, A. Bonato, C. Botta, H. Breuker, T. Camporesi, G. Cerminara, T. Christiansen, J.A. Coarasa Perez, D. d'Enterria, A. Dabrowski, A. De Roeck, S. Di Guida, M. Dobson, N. Dupont-Sagorin, A. Elliott-Peisert, B. Frisch, W. Funk, G. Georgiou, M. Giffels, D. Gigi, K. Gill, D. Giordano, M. Girone, M. Giunta, F. Glege, R. Gomez-Reino Garrido, P. Govoni, S. Gowdy, R. Guida, S. Gundacker, J. Hammer, M. Hansen, P. Harris, C. Hartl, J. Harvey, B. Hegner, A. Hinzmann, V. Innocente, P. Janot, K. Kaadze, E. Karavakis, K. Kousouris, P. Lecoq, Y.-J. Lee, P. Lenzi, C. Lourenço, N. Magini, T. Mäki, M. Malberti, L. Malgeri, M. Mannelli, L. Masetti, F. Meijers, S. Mersi, E. Meschi, R. Moser, M.U. Mozer, M. Mulders, P. Musella, E. Nesvold, L. Orsini, E. Palencia Cortezon, E. Perez, L. Perrozzi, A. Petrilli, A. Pfeiffer, M. Pierini, M. Pimiä, D. Piparo, G. Polese, L. Quertenmont, A. Racz, W. Reece, J. Rodrigues Antunes, G. Rolandi[33], C. Rovelli[34], M. Rovere, H. Sakulin, F. Santanastasio, C. Schäfer, C. Schwick, I. Segoni, S. Sekmen, A. Sharma, P. Siegrist, P. Silva,

M. Simon, P. Sphicas[35], D. Spiga, A. Tsirou, G.I. Veres[19], J.R. Vlimant, H.K. Wöhri, S.D. Worm[36], W.D. Zeuner

Paul Scherrer Institut, Villigen, Switzerland

W. Bertl, K. Deiters, W. Erdmann, K. Gabathuler, R. Horisberger, Q. Ingram, H.C. Kaestli, S. König, D. Kotlinski, U. Langenegger, F. Meier, D. Renker, T. Rohe

Institute for Particle Physics, ETH Zurich, Zurich, Switzerland

L. Bäni, P. Bortignon, M.A. Buchmann, B. Casal, N. Chanon, A. Deisher, G. Dissertori, M. Dittmar, M. Donegà, M. Dünser, P. Eller, J. Eugster, K. Freudenreich, C. Grab, D. Hits, P. Lecomte, W. Lustermann, A.C. Marini, P. Martinez Ruiz del Arbol, N. Mohr, F. Moortgat, C. Nägeli[37], P. Nef, F. Nessi-Tedaldi, F. Pandolfi, L. Pape, F. Pauss, M. Peruzzi, F.J. Ronga, M. Rossini, L. Sala, A.K. Sanchez, A. Starodumov[38], B. Stieger, M. Takahashi, L. Tauscher[†], A. Thea, K. Theofilatos, D. Treille, C. Urscheler, R. Wallny, H.A. Weber, L. Wehrli

Universität Zürich, Zurich, Switzerland

C. Amsler[39], V. Chiochia, S. De Visscher, C. Favaro, M. Ivova Rikova, B. Kilminster, B. Millan Mejias, P. Otiougova, P. Robmann, H. Snoek, S. Tupputi, M. Verzetti

National Central University, Chung-Li, Taiwan

Y.H. Chang, K.H. Chen, C. Ferro, C.M. Kuo, S.W. Li, W. Lin, Y.J. Lu, A.P. Singh, R. Volpe, S.S. Yu

National Taiwan University (NTU), Taipei, Taiwan

P. Bartalini, P. Chang, Y.H. Chang, Y.W. Chang, Y. Chao, K.F. Chen, C. Dietz, U. Grundler, W.-S. Hou, Y. Hsiung, K.Y. Kao, Y.J. Lei, R.-S. Lu, D. Majumder, E. Petrakou, X. Shi, J.G. Shiu, Y.M. Tzeng, X. Wan, M. Wang

Chulalongkorn University, Bangkok, Thailand

B. Asavapibhop, N. Srimanobhas

Cukurova University, Adana, Turkey

A. Adiguzel, M.N. Bakirci[40], S. Cerci[41], C. Dozen, I. Dumanoglu, E. Eskut, S. Girgis, G. Gokbulut, E. Gurpinar, I. Hos, E.E. Kangal, T. Karaman, G. Karapinar[42], A. Kayis Topaksu, G. Onengut, K. Ozdemir, S. Ozturk[43], A. Polatoz, K. Sogut[44], D. Sunar Cerci[41], B. Tali[41], H. Topakli[40], L.N. Vergili, M. Vergili

Middle East Technical University, Physics Department, Ankara, Turkey

I.V. Akin, T. Aliev, B. Bilin, S. Bilmis, M. Deniz, H. Gamsizkan, A.M. Guler, K. Ocalan, A. Ozpineci, M. Serin, R. Sever, U.E. Surat, M. Yalvac, E. Yildirim, M. Zeyrek

Bogazici University, Istanbul, Turkey

E. Gülmez, B. Isildak[45], M. Kaya[46], O. Kaya[46], S. Ozkorucuklu[47], N. Sonmez[48]

Istanbul Technical University, Istanbul, Turkey

K. Cankocak

National Scientific Center, Kharkov Institute of Physics and Technology, Kharkov, Ukraine

L. Levchuk

University of Bristol, Bristol, United Kingdom

J.J. Brooke, E. Clement, D. Cussans, H. Flacher, R. Frazier, J. Goldstein, M. Grimes, G.P. Heath, H.F. Heath, L. Kreczko, S. Metson, D.M. Newbold[36], K. Nirunpong, A. Poll, S. Senkin, V.J. Smith, T. Williams

Rutherford Appleton Laboratory, Didcot, United Kingdom

L. Basso[49], K.W. Bell, A. Belyaev[49], C. Brew, R.M. Brown, D.J.A. Cockerill, J.A. Coughlan, K. Harder, S. Harper, J. Jackson, B.W. Kennedy, E. Olaiya, D. Petyt, B.C. Radburn-Smith, C.H. Shepherd-Themistocleous, I.R. Tomalin, W.J. Womersley

Imperial College, London, United Kingdom

R. Bainbridge, G. Ball, R. Beuselinck, O. Buchmuller, D. Colling, N. Cripps, M. Cutajar, P. Dauncey, G. Davies, M. Della Negra, W. Ferguson, J. Fulcher, D. Futyan, A. Gilbert, A. Guneratne Bryer, G. Hall, Z. Hatherell, J. Hays, G. Iles, M. Jarvis, G. Karapostoli, L. Lyons, A.-M. Magnan, J. Marrouche, B. Mathias, R. Nandi, J. Nash, A. Nikitenko[38], J. Pela, M. Pesaresi, K. Petridis, M. Pioppi[50], D.M. Raymond, S. Rogerson, A. Rose, M.J. Ryan, C. Seez, P. Sharp[†], A. Sparrow, M. Stoye, A. Tapper, M. Vazquez Acosta, T. Virdee, S. Wakefield, N. Wardle, T. Whyntie

Brunel University, Uxbridge, United Kingdom

M. Chadwick, J.E. Cole, P.R. Hobson, A. Khan, P. Kyberd, D. Leggat, D. Leslie, W. Martin, I.D. Reid, P. Symonds, L. Teodorescu, M. Turner

Baylor University, Waco, U.S.A.

K. Hatakeyama, H. Liu, T. Scarborough

The University of Alabama, Tuscaloosa, U.S.A.

O. Charaf, C. Henderson, P. Rumerio

Boston University, Boston, U.S.A.

A. Avetisyan, T. Bose, C. Fantasia, A. Heister, P. Lawson, D. Lazic, J. Rohlf, D. Sperka, J. St. John, L. Sulak

Brown University, Providence, U.S.A.

J. Alimena, S. Bhattacharya, G. Christopher, D. Cutts, Z. Demiragli, A. Ferapontov, A. Garabedian, U. Heintz, S. Jabeen, G. Kukartsev, E. Laird, G. Landsberg, M. Luk, M. Narain, D. Nguyen, M. Segala, T. Sinthuprasith, T. Speer

University of California, Davis, Davis, U.S.A.

R. Breedon, G. Breto, M. Calderon De La Barca Sanchez, S. Chauhan, M. Chertok, J. Conway, R. Conway, P.T. Cox, J. Dolen, R. Erbacher, M. Gardner, B. Holbrook, R. Houtz, W. Ko, A. Kopecky, R. Lander, O. Mall, T. Miceli, D. Pellett, F. Ricci-Tam, B. Rutherford, M. Searle, J. Smith, M. Squires, M. Tripathi, R. Vasquez Sierra, R. Yohay

University of California, Los Angeles, U.S.A.

V. Andreev, D. Cline, R. Cousins, J. Duris, S. Erhan, P. Everaerts, C. Farrell, J. Hauser, M. Ignatenko, C. Jarvis, G. Rakness, P. Schlein[†], P. Traczyk, V. Valuev, M. Weber, X. Yang

University of California, Riverside, Riverside, U.S.A.

J. Babb, R. Clare, M.E. Dinardo, J. Ellison, J.W. Gary, F. Giordano, G. Hanson, H. Liu, O.R. Long, A. Luthra, H. Nguyen, S. Paramesvaran, J. Sturdy, S. Sumowidagdo, R. Wilken, S. Wimpenny

University of California, San Diego, La Jolla, U.S.A.

W. Andrews, J.G. Branson, G.B. Cerati, S. Cittolin, D. Evans, A. Holzner, R. Kelley, M. Lebourgeois, J. Letts, I. Macneill, B. Mangano, S. Padhi, C. Palmer, G. Petrucciani, M. Pieri, M. Sani, V. Sharma, S. Simon, E. Sudano, M. Tadel, Y. Tu, A. Vartak, S. Wasserbaech[51], F. Würthwein, A. Yagil, J. Yoo

University of California, Santa Barbara, Santa Barbara, U.S.A.

D. Barge, R. Bellan, C. Campagnari, M. D'Alfonso, T. Danielson, K. Flowers, P. Geffert, F. Golf, J. Incandela, C. Justus, P. Kalavase, D. Kovalskyi, V. Krutelyov, S. Lowette, R. Magaña Villalba, N. Mccoll, V. Pavlunin, J. Ribnik, J. Richman, R. Rossin, D. Stuart, W. To, C. West

California Institute of Technology, Pasadena, U.S.A.

A. Apresyan, A. Bornheim, J. Bunn, Y. Chen, E. Di Marco, J. Duarte, M. Gataullin, D. Kcira, Y. Ma, A. Mott, H.B. Newman, C. Rogan, M. Spiropulu, V. Timciuc, J. Veverka, R. Wilkinson, S. Xie, Y. Yang, R.Y. Zhu

Carnegie Mellon University, Pittsburgh, U.S.A.

V. Azzolini, A. Calamba, R. Carroll, T. Ferguson, Y. Iiyama, D.W. Jang, Y.F. Liu, M. Paulini, H. Vogel, I. Vorobiev

University of Colorado at Boulder, Boulder, U.S.A.

J.P. Cumalat, B.R. Drell, W.T. Ford, A. Gaz, E. Luiggi Lopez, J.G. Smith, K. Stenson, K.A. Ulmer, S.R. Wagner

Cornell University, Ithaca, U.S.A.

J. Alexander, A. Chatterjee, N. Eggert, L.K. Gibbons, B. Heltsley, W. Hopkins, A. Khukhunaishvili, B. Kreis, N. Mirman, G. Nicolas Kaufman, J.R. Patterson, A. Ryd, E. Salvati, W. Sun, W.D. Teo, J. Thom, J. Thompson, J. Tucker, J. Vaughan, Y. Weng, L. Winstrom, P. Wittich

Fairfield University, Fairfield, U.S.A.

D. Winn

Fermi National Accelerator Laboratory, Batavia, U.S.A.

S. Abdullin, M. Albrow, J. Anderson, G. Apollinari, L.A.T. Bauerdick, A. Beretvas, J. Berryhill, P.C. Bhat, K. Burkett, J.N. Butler, N. Chester, V. Chetluru, H.W.K. Cheung, F. Chlebana, S. Cihangir, D.P. Eartly, V.D. Elvira, I. Fisk, J. Freeman, Y. Gao, D. Green, O. Gutsche, J. Hanlon, R.M. Harris, J. Hirschauer, B. Hooberman, S. Jindariani, M. Johnson, U. Joshi, B. Klima, S. Kunori, S. Kwan, C. Leonidopoulos[52], J. Linacre, D. Lincoln, R. Lipton, J. Lykken, K. Maeshima, J.M. Marraffino, S. Maruyama, D. Mason, P. McBride, K. Mishra, S. Mrenna, Y. Musienko[53], C. Newman-Holmes, V. O'Dell, O. Prokofyev, V. Rasmislovich, E. Sexton-Kennedy, S. Sharma, W.J. Spalding, L. Spiegel, L. Taylor, S. Tkaczyk, N.V. Tran, L. Uplegger, E.W. Vaandering, R. Vidal, J. Whitmore, W. Wu, F. Yang, J.C. Yun

University of Florida, Gainesville, U.S.A.

D. Acosta, P. Avery, V. Barashko, D. Bourilkov, M. Chen, T. Cheng, S. Das, M. De Gruttola, G.P. Di Giovanni, D. Dobur, A. Drozdetskiy, R.D. Field, M. Fisher, Y. Fu, I.K. Furic, J. Gartner, J. Hugon, B. Kim, J. Konigsberg, A. Korytov, A. Kropivnitskaya, T. Kypreos, J.F. Low, A. Madorsky, K. Matchev, P. Milenovic[54], G. Mitselmakher, L. Muniz, M. Park, R. Remington, A. Rinkevicius, P. Sellers, N. Skhirtladze, M. Snowball, J. Yelton, M. Zakaria

Florida International University, Miami, U.S.A.

V. Gaultney, S. Hewamanage, L.M. Lebolo, S. Linn, P. Markowitz, G. Martinez, J.L. Rodriguez

Florida State University, Tallahassee, U.S.A.

T. Adams, A. Askew, J. Bochenek, J. Chen, B. Diamond, S.V. Gleyzer, J. Haas, S. Hagopian, V. Hagopian, M. Jenkins, K.F. Johnson, H. Prosper, V. Veeraraghavan, M. Weinberg

Florida Institute of Technology, Melbourne, U.S.A.

M.M. Baarmand, B. Dorney, M. Hohlmann, H. Kalakhety, I. Vodopiyanov, F. Yumiceva

University of Illinois at Chicago (UIC), Chicago, U.S.A.

M.R. Adams, I.M. Anghel, L. Apanasevich, Y. Bai, V.E. Bazterra, R.R. Betts, I. Bucinskaite, J. Callner, R. Cavanaugh, O. Evdokimov, L. Gauthier, C.E. Gerber, D.J. Hofman, S. Khalatyan, F. Lacroix, C. O'Brien, C. Silkworth, D. Strom, P. Turner, N. Varelas

The University of Iowa, Iowa City, U.S.A.

U. Akgun, E.A. Albayrak, B. Bilki[55], W. Clarida, F. Duru, S. Griffiths, J.-P. Merlo, H. Mermerkaya[56], A. Mestvirishvili, A. Moeller, J. Nachtman, C.R. Newsom, E. Norbeck, Y. Onel, F. Ozok[57], S. Sen, P. Tan, E. Tiras, J. Wetzel, T. Yetkin[58], K. Yi

Johns Hopkins University, Baltimore, U.S.A.

B.A. Barnett, B. Blumenfeld, S. Bolognesi, D. Fehling, G. Giurgiu, A.V. Gritsan, G. Hu, P. Maksimovic, M. Swartz, A. Whitbeck

The University of Kansas, Lawrence, U.S.A.

P. Baringer, A. Bean, G. Benelli, R.P. Kenny III, M. Murray, D. Noonan, S. Sanders, R. Stringer, G. Tinti, J.S. Wood

Kansas State University, Manhattan, U.S.A.

A.F. Barfuss, T. Bolton, I. Chakaberia, A. Ivanov, S. Khalil, M. Makouski, Y. Maravin, S. Shrestha, I. Svintradze

Lawrence Livermore National Laboratory, Livermore, U.S.A.

J. Gronberg, D. Lange, F. Rebassoo, D. Wright

University of Maryland, College Park, U.S.A.

A. Baden, B. Calvert, S.C. Eno, J.A. Gomez, N.J. Hadley, R.G. Kellogg, M. Kirn, T. Kolberg, Y. Lu, M. Marionneau, A.C. Mignerey, K. Pedro, A. Peterman, A. Skuja, J. Temple, M.B. Tonjes, S.C. Tonwar

Massachusetts Institute of Technology, Cambridge, U.S.A.

A. Apyan, G. Bauer, J. Bendavid, W. Busza, E. Butz, I.A. Cali, M. Chan, V. Dutta, G. Gomez Ceballos, M. Goncharov, Y. Kim, M. Klute, K. Krajczar[59], A. Levin, P.D. Luckey, T. Ma, S. Nahn, C. Paus, D. Ralph, C. Roland, G. Roland, M. Rudolph, G.S.F. Stephans, F. Stöckli, K. Sumorok, K. Sung, D. Velicanu, E.A. Wenger, R. Wolf, B. Wyslouch, M. Yang, Y. Yilmaz, A.S. Yoon, M. Zanetti, V. Zhukova

University of Minnesota, Minneapolis, U.S.A.

S.I. Cooper, B. Dahmes, A. De Benedetti, G. Franzoni, A. Gude, J. Haupt, S.C. Kao, K. Klapoetke, Y. Kubota, J. Mans, N. Pastika, R. Rusack, M. Sasseville, A. Singovsky, N. Tambe, J. Turkewitz

University of Mississippi, Oxford, U.S.A.

L.M. Cremaldi, R. Kroeger, L. Perera, R. Rahmat, D.A. Sanders

University of Nebraska-Lincoln, Lincoln, U.S.A.

E. Avdeeva, K. Bloom, S. Bose, D.R. Claes, A. Dominguez, M. Eads, J. Keller, I. Kravchenko, J. Lazo-Flores, S. Malik, G.R. Snow

State University of New York at Buffalo, Buffalo, U.S.A.

A. Godshalk, I. Iashvili, S. Jain, A. Kharchilava, A. Kumar, S. Rappoccio

Northeastern University, Boston, U.S.A.

G. Alverson, E. Barberis, D. Baumgartel, M. Chasco, J. Haley, D. Nash, T. Orimoto, D. Trocino, D. Wood, J. Zhang

Northwestern University, Evanston, U.S.A.

A. Anastassov, K.A. Hahn, A. Kubik, L. Lusito, N. Mucia, N. Odell, R.A. Ofierzynski, B. Pollack, A. Pozdnyakov, M. Schmitt, S. Stoynev, M. Velasco, S. Won

University of Notre Dame, Notre Dame, U.S.A.

L. Antonelli, D. Berry, A. Brinkerhoff, K.M. Chan, M. Hildreth, C. Jessop, D.J. Karmgard, J. Kolb, K. Lannon, W. Luo, S. Lynch, N. Marinelli, D.M. Morse, T. Pearson, M. Planer, R. Ruchti, J. Slaunwhite, N. Valls, M. Wayne, M. Wolf

The Ohio State University, Columbus, U.S.A.

B. Bylsma, L.S. Durkin, C. Hill, R. Hughes, K. Kotov, T.Y. Ling, D. Puigh, M. Rodenburg, C. Vuosalo, G. Williams, B.L. Winer

Princeton University, Princeton, U.S.A.

E. Berry, P. Elmer, V. Halyo, P. Hebda, J. Hegeman, A. Hunt, P. Jindal, S.A. Koay, D. Lopes Pegna, P. Lujan, D. Marlow, T. Medvedeva, M. Mooney, J. Olsen, P. Piroué, X. Quan, A. Raval, H. Saka, D. Stickland, C. Tully, J.S. Werner, A. Zuranski

University of Puerto Rico, Mayaguez, U.S.A.

E. Brownson, A. Lopez, H. Mendez, J.E. Ramirez Vargas

Purdue University, West Lafayette, U.S.A.

E. Alagoz, V.E. Barnes, D. Benedetti, G. Bolla, D. Bortoletto, M. De Mattia, A. Everett, Z. Hu, M. Jones, O. Koybasi, M. Kress, A.T. Laasanen, N. Leonardo, V. Maroussov, P. Merkel,

D.H. Miller, N. Neumeister, I. Shipsey, D. Silvers, A. Svyatkovskiy, M. Vidal Marono, H.D. Yoo, J. Zablocki, Y. Zheng

Purdue University Calumet, Hammond, U.S.A.

S. Guragain, N. Parashar

Rice University, Houston, U.S.A.

A. Adair, B. Akgun, C. Boulahouache, K.M. Ecklund, F.J.M. Geurts, W. Li, B.P. Padley, R. Redjimi, J. Roberts, J. Zabel

University of Rochester, Rochester, U.S.A.

B. Betchart, A. Bodek, Y.S. Chung, R. Covarelli, P. de Barbaro, R. Demina, Y. Eshaq, T. Ferbel, A. Garcia-Bellido, P. Goldenzweig, J. Han, A. Harel, D.C. Miner, D. Vishnevskiy, M. Zielinski

The Rockefeller University, New York, U.S.A.

A. Bhatti, R. Ciesielski, L. Demortier, K. Goulianos, G. Lungu, S. Malik, C. Mesropian

Rutgers, The State University of New Jersey, Piscataway, U.S.A.

S. Arora, A. Barker, J.P. Chou, C. Contreras-Campana, E. Contreras-Campana, D. Duggan, D. Ferencek, Y. Gershtein, R. Gray, E. Halkiadakis, D. Hidas, A. Lath, S. Panwalkar, M. Park, R. Patel, V. Rekovic, J. Robles, K. Rose, S. Salur, S. Schnetzer, C. Seitz, S. Somalwar, R. Stone, S. Thomas, M. Walker

University of Tennessee, Knoxville, U.S.A.

G. Cerizza, M. Hollingsworth, S. Spanier, Z.C. Yang, A. York

Texas A&M University, College Station, U.S.A.

R. Eusebi, W. Flanagan, J. Gilmore, T. Kamon[60], V. Khotilovich, R. Montalvo, I. Osipenkov, Y. Pakhotin, A. Perloff, J. Roe, A. Safonov, T. Sakuma, S. Sengupta, I. Suarez, A. Tatarinov, D. Toback

Texas Tech University, Lubbock, U.S.A.

N. Akchurin, J. Damgov, C. Dragoiu, P.R. Dudero, C. Jeong, K. Kovitanggoon, S.W. Lee, T. Libeiro, I. Volobouev

Vanderbilt University, Nashville, U.S.A.

E. Appelt, A.G. Delannoy, C. Florez, S. Greene, A. Gurrola, W. Johns, P. Kurt, C. Maguire, A. Melo, M. Sharma, P. Sheldon, B. Snook, S. Tuo, J. Velkovska

University of Virginia, Charlottesville, U.S.A.

M.W. Arenton, M. Balazs, S. Boutle, B. Cox, B. Francis, J. Goodell, R. Hirosky, A. Ledovskoy, C. Lin, C. Neu, J. Wood

Wayne State University, Detroit, U.S.A.

S. Gollapinni, R. Harr, P.E. Karchin, C. Kottachchi Kankanamge Don, P. Lamichhane, A. Sakharov

University of Wisconsin, Madison, U.S.A.

M. Anderson, D.A. Belknap, L. Borrello, D. Carlsmith, M. Cepeda, S. Dasu, E. Friis, L. Gray, K.S. Grogg, M. Grothe, R. Hall-Wilton, M. Herndon, A. Hervé, P. Klabbers, J. Klukas, A. Lanaro,

C. Lazaridis, R. Loveless, S. Lusin, A. Mohapatra, I. Ojalvo, F. Palmonari, G.A. Pierro, I. Ross, A. Savin, W.H. Smith, J. Swanson, D. Wenman

†: Deceased

1: Also at Vienna University of Technology, Vienna, Austria

2: Also at CERN, European Organization for Nuclear Research, Geneva, Switzerland

3: Also at National Institute of Chemical Physics and Biophysics, Tallinn, Estonia

4: Also at California Institute of Technology, Pasadena, U.S.A.

5: Also at Laboratoire Leprince-Ringuet, Ecole Polytechnique, IN2P3-CNRS, Palaiseau, France

6: Also at Zewail City of Science and Technology, Zewail, Egypt

7: Also at Suez Canal University, Suez, Egypt

8: Also at Cairo University, Cairo, Egypt

9: Also at Fayoum University, El-Fayoum, Egypt

10: Also at British University in Egypt, Cairo, Egypt

11: Now at Ain Shams University, Cairo, Egypt

12: Also at National Centre for Nuclear Research, Swierk, Poland

13: Also at Université de Haute Alsace, Mulhouse, France

14: Also at Joint Institute for Nuclear Research, Dubna, Russia

15: Also at Skobeltsyn Institute of Nuclear Physics, Lomonosov Moscow State University, Moscow, Russia

16: Also at Brandenburg University of Technology, Cottbus, Germany

17: Also at The University of Kansas, Lawrence, U.S.A.

18: Also at Institute of Nuclear Research ATOMKI, Debrecen, Hungary

19: Also at Eötvös Loránd University, Budapest, Hungary

20: Also at Tata Institute of Fundamental Research - HECR, Mumbai, India

21: Now at King Abdulaziz University, Jeddah, Saudi Arabia

22: Also at University of Visva-Bharati, Santiniketan, India

23: Also at Sharif University of Technology, Tehran, Iran

24: Also at Isfahan University of Technology, Isfahan, Iran

25: Also at Shiraz University, Shiraz, Iran

26: Also at Plasma Physics Research Center, Science and Research Branch, Islamic Azad University, Tehran, Iran

27: Also at Facoltà Ingegneria, Università di Roma, Roma, Italy

28: Also at Università degli Studi di Siena, Siena, Italy

29: Also at University of Bucharest, Faculty of Physics, Bucuresti-Magurele, Romania

30: Also at INFN Sezione di Padova; Università di Padova; Università di Trento (Trento), Padova, Italy

31: Also at Faculty of Physics, University of Belgrade, Belgrade, Serbia

32: Also at University of California, Los Angeles, U.S.A.

33: Also at Scuola Normale e Sezione dell'INFN, Pisa, Italy

34: Also at INFN Sezione di Roma, Roma, Italy

35: Also at University of Athens, Athens, Greece

36: Also at Rutherford Appleton Laboratory, Didcot, United Kingdom

37: Also at Paul Scherrer Institut, Villigen, Switzerland

38: Also at Institute for Theoretical and Experimental Physics, Moscow, Russia

39: Also at Albert Einstein Center for Fundamental Physics, Bern, Switzerland

40: Also at Gaziosmanpasa University, Tokat, Turkey

41: Also at Adiyaman University, Adiyaman, Turkey

42: Also at Izmir Institute of Technology, Izmir, Turkey

43: Also at The University of Iowa, Iowa City, U.S.A.

44: Also at Mersin University, Mersin, Turkey

45: Also at Ozyegin University, Istanbul, Turkey

46: Also at Kafkas University, Kars, Turkey

47: Also at Suleyman Demirel University, Isparta, Turkey

48: Also at Ege University, Izmir, Turkey

49: Also at School of Physics and Astronomy, University of Southampton, Southampton, United Kingdom

50: Also at INFN Sezione di Perugia; Università di Perugia, Perugia, Italy

51: Also at Utah Valley University, Orem, U.S.A.

52: Now at University of Edinburgh, Scotland, Edinburgh, United Kingdom

53: Also at Institute for Nuclear Research, Moscow, Russia

54: Also at University of Belgrade, Faculty of Physics and Vinca Institute of Nuclear Sciences, Belgrade, Serbia

55: Also at Argonne National Laboratory, Argonne, U.S.A.

56: Also at Erzincan University, Erzincan, Turkey

57: Also at Mimar Sinan University, Istanbul, Istanbul, Turkey

58: Also at Yildiz Technical University, Istanbul, Turkey

59: Also at KFKI Research Institute for Particle and Nuclear Physics, Budapest, Hungary

60: Also at Kyungpook National University, Daegu, Korea